Current distribution inside Rutherford–type superconducting cables and impact on performance of LHC dipoles

Thomas Schreiner
CERN LHC-MTA

26. Februar 2002

Deutsche Kurzfassung der Dissertation

Die Spulen von supraleitenden Beschleunigermagneten mit hoher Feldstärke werden üblicherweise aus Rutherford Kabel gewickelt. Die magnetische Feldverteilung entlang der Achse solcher Magnete weist eine periodische Überlagerung des Feldes auf, die dem Wicklungsabstand der Drähte (Strands) auf dem verwendetem Kabel entspricht. Diese periodischen Magnetfeldschwankungen (periodic field pattern, PFP) wurden an etlichen supraleitenden Beschleunigermagneten beobachtet. Zusätzliche unsymmetrische Ströme treten in den einzelnen Strands des Kabels auf und verursachen diesen Effekt. Die vorliegende Arbeit beschreibt die Untersuchung der PFPs, die mit einer Anordnung aus Hallproben innerhalb der Öffnung der supraleitenden LHC Dipole durchgeführt wurde. Die Messungen wurden sowohl an kurzen Modelmagneten mit einer Länge von einem Meter, als auch an Prototypen und Vorserienmagneten mit einer Länge von fünfzehn Meter ausgeführt. Die Amplitude und das zeitliche Verhalten dieser periodischen Feldoszillationen wurden in Abhängigkeit der verwendeten Stromzyklen der Magnete untersucht.

Einer der Hauptparameter, der die Eigenschaften des PFP beeinflußt, ist der Kontaktwiderstand zwischen den Strands des Kabels. Eine Abschätzung dieser Werte wird durch die sogenannten Field–Advance (FA) Messungen erzielt, die auch mittels der bereits verwendeten Hallproben durchgeführt wurden. Auf Grund von Wirbelströmen werden unterschiedliche Magnetfeldstärken für den aufsteigenden und den fallenden Teil eines Stromzyklus generiert. Diese Differenz ist eine lineare Funktion der zeitlichen Stromänderung. Die so erhaltene Steigung ist wiederum indirekt proportional dem entsprechendem Kontaktwiderstand.

Es werden gleichmäßig und ungleichmäßig gekoppelte Ströme durch ein sich änderndes Magnetfeld induziert, die nicht nur innerhalb der einzelnen Strands sondern auch zwischen den Strands des Kabels fließen. Dadurch kann in Teilen der Strands ein Gesamtstrom auftreten der größer ist als der Transportstrom. Dieses Phänomen reduziert örtlich die Differenz zwischen dem Gesamtstrom in den Strands und dem kritischen Strom des Supraleiters. Als Folge kann ein vorzeitiger Quench der supraleitenden Magnete auftreten, i.e. ein Übergang in den normalleitenden Zustand.

An Hand theoretischer Modelle sowie experimenteller Ergebnisse werden die Auswirkungen der Stromverteilung auf das Quenchverhalten der LHC Dipole behandelt. Schließlich wird auch eine Abschätzung über den Einfluß dieser Ströme auf die Stabilität der Magnete in Bezug auf Quench unter Betriebsbedingungen gegeben.

Abstract

The windings of high–field superconducting accelerator magnets are usually made of Rutherford–type cables. The magnetic field distribution along the axis of such magnets exhibits a periodic modulation with a wavelength equal to the twist pitch length of the cable used in the winding. Such a Periodic Field Pattern (PFP) has already been observed in number of superconducting accelerator magnets. Additional unbalanced currents in individual strands of the cable appear to be causing this effect. The present thesis describes the investigation of the PFPs performed with a Hall probes array inserted inside the aperture of the LHC superconducting dipoles, both in the small–scale model magnets with a length of one meter and in full–scale prototypes and pre–series magnets with fifteen meters of length. The amplitude and the time dependence of this periodic field oscillation have been studied as a function of the magnet current history.

One of the main parameters influencing the properties of the PFP is the cross–contact resistance between the strands of the cable. An estimation for these values is achieved by the so–called Field Advance (FA) measurements performed again with a Hall probes set–up. Due to eddy currents a difference in the field values for the ramp–up and the ramp–down of a current cycle is generated, which is a linear function of the applied ramp rate. The resulting slope is furthermore indirectly proportional to the corresponding cross–contact resistance.

Two types of so–called interstrand coupling currents, uniform and non–uniform, are induced by a changing magnetic field and flow not only within the individual strands but also between the strands of the cable. Therefore some parts of the strands can carry a total current which is larger than the transport current. This phenomenon locally reduces the difference between the total strand current and the critical current of the superconductor and can provoke a premature quench of the superconducting magnet, i.e. a transition to the normal state.

Considering theoretical models and experimental results the impact of the current distribution on the quench performance of the LHC dipoles is discussed. Finally an estimation for the influence of these currents on the magnet stability with respect to quench during operation conditions is given.

Acknowledgments

This work was carried out within the scope of the Austrian Doctoral Student Program in the LHC-MTA group at CERN, Geneva, Switzerland.

I should like to thank my university supervisor Prof. Dr. Hans Kirchmayr, head of the Institute of Experimental Physics at the University of Technology in Vienna, and my CERN supervisor, Dr. Andrzej Siemko of the LHC-MTA group for their help and encouragement during this project.

I would also like to mention the valuable assistance of all the members of the MTA group at CERN. Especially I am grateful to P. Pugnat for fruitful discussions and P. Schnizer for his help and support during the development of the Python code.

Last but not least, I would like to thank my family for their moral support accorded me during all these years of study and all my friends for their continuous encouragement.

Contents

Chapter 1

Introduction

1.1 CERN before LHC project

The creation of an European Laboratory was recommended at an UNESCO meeting in Florence in 1950. Only three years later the first European joint venture (12 countries were present) was founded by signing a Convention of the Conseil Européen pour la Recherche Nucleaire. CERN, the European Organization for Nuclear Research and Particle Physics was born. The motivation for this project was the search for answers of the fundamental questions of the natural scientists, the beginning of the universe and to understand the fundamental forces [1].

Colliding particles at high energies is one of the most effective ways to get information about their behavior and their properties. Therefore accelerators were built for all kinds of different particles e.g. PS the Intersecting Storage Rings (IRS) proton–proton collider, the proton–antiproton collider at the Super Proton Synchrotron (SPS), which produced the massive W and Z particles (1983), confirming the unified theory of electromagnetic and weak force. Figure 1.1 gives an overview of the accelerator complex considering the LEP machine. There are two types of accelerator at CERN, linear and circular. Although all particle beams begin their lifetime in linear accelerators, the big machines today are circulator accelerators because of requiring an enormous length for linear ones at high energy. However the next project after the LHC will be perhaps a linear accelerator using new technology at CERN.

On the second November of 2000 the Large Electron Positron collider (LEP) ended its operation lifetime. It was the largest accelerator of CERN and in the world for eleven years. The circumference of the tunnel, 100 meters below the ground, was equal to $27\,km$. No less than 3368 magnets were necessary for focussing and bending the beams on a curved track. For the detection of the huge number of different particles which were created during the collisions of the electron–positron beams the ALEPH, the DELPHI, the L 3 and the OPAL detectors were placed at four points around the accelerator circumference.

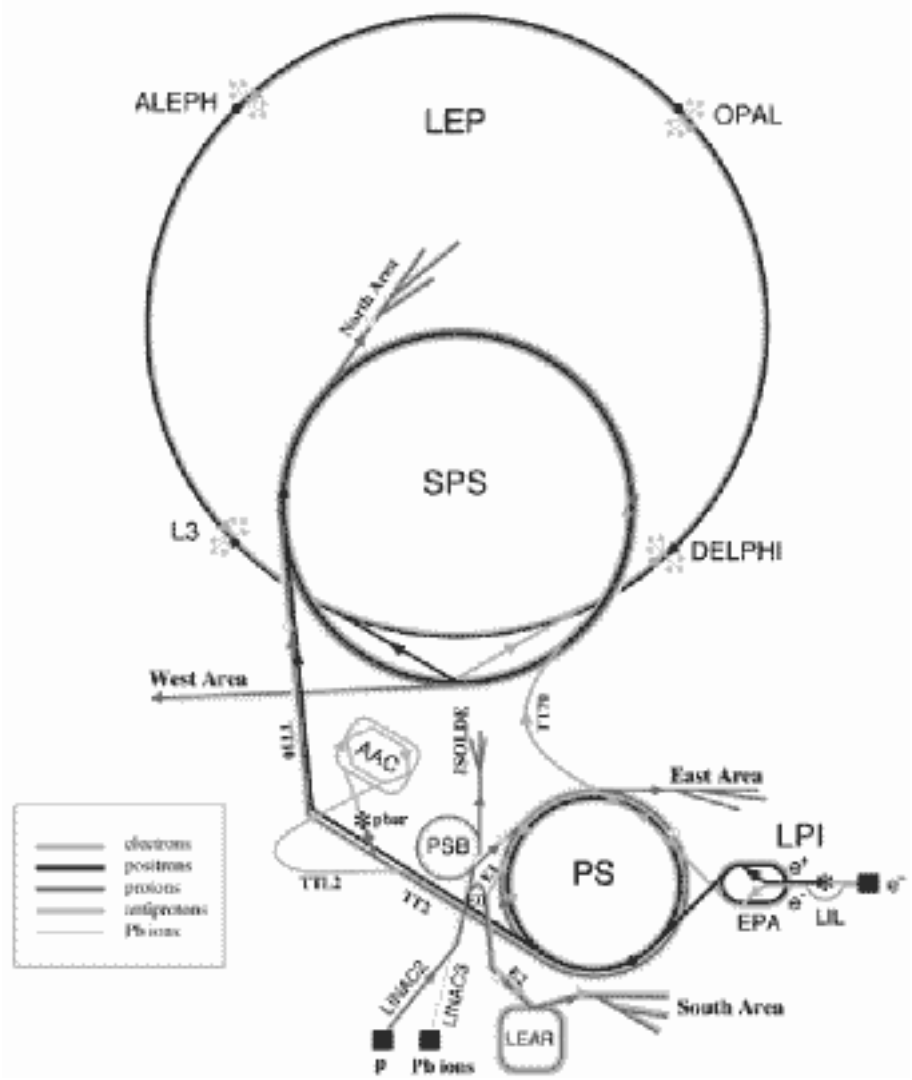

Figure 1.1: Map of all accelerators at CERN before the LHC. LEP: Large Electron Positron collider, SPS: Super Proton Synchrotron, AAC: Antiproton Accumulator Complex, ISOLDE: Isotope Separator OnLine DEvice, PSB: Proton Synchrotron Booster, PS : Proton Synchrotron, LPI: Lep Pre-Injector, EPA: Electron Positron Accumulator, LIL: Lep Injector Linac, LINAC2: LINear ACcelerator 2, LINAC3: LINear ACcelerator 3, LEAR/LEIR: Low Energy Ion Ring [2]

Already in the early days of LEP it was possible to count how many types of neutrinos exist in the universe by detailed studies of the unstable Z particle, based on nearly $2 \cdot 10^7$ examples of its decays measured. The answer turns out to be three, the electron–neutrino, the myon–neutrino and the tau–neutrino. Within the Standard Model (SM), this means that there can be no more siblings of the electron, beyond the known myon and tau, and hence no more than 6 quark constituents of nuclear matter. In 1998 a beam energy sligthly larger than $200\,GeV$ was reached in the so–called LEP II, where the W particles are produced and studied. Therefore the measurements of the mass of the W boson ($80.35 \pm 0.09\,GeV$) have reached a high level of accuracy.

In the final operation period LEP has achieved a collision energy of over $104\,GeV$ per beam and the last experiments have been reporting tantalizing hints of new physics. But unfortunately the mass collision energy of the LEP was limited because of the synchrotron radiation. If charged particle are accelerated on a circular path, they will emit a power P_s which is given by Equation 1.1.

$$P_s = \frac{e^2}{6\pi\varepsilon_0}\frac{\left(\ddot{z}\gamma^2\right)^2}{c^3} = \frac{e^2 c}{6\pi\varepsilon_0}\frac{\gamma^4}{\rho^2} \propto \frac{1}{\left(m_0c^2\right)^4}\frac{E^4}{\rho^2} \tag{1.1}$$

e	...	elementary charge of an electron
$\ddot{z} = v^2/\rho \approx c^2/\rho$	...	motion in a circle
ρ	...	radius of curvature of the particle trajectory
$E = \gamma E_0 = \gamma m_0 c^2$	...	particle energy
$E_0 = m_0 c^2$	...	rest energy of the particle

Considering a LEP operation at $100\,GeV$ we can compute a power of $16\,MW$ [3]. This amount must be provided by the accelerating cavities, which have intrinsic limitations.

The required power can be dramatically reduced when accelerating heavier protons instead of electrons in an accelerator with equal energy and radius. This results in the fact that Equation 1.1 for the emission of the synchrotron radiation is in principle the same for both, electrons and protons. Thus P_s would be significantly decreased by using protons because the power radiated is inversely proportional to the fourth power of the rest mass. Comparing the rest energy of the electron with $0.511\,MeV$ and that one of the proton with $938.19\,MeV$ shows, that for the same energy and magnetic field electrons radiate $1.13 \cdot 10^{13}$ more power than protons [4]. This leads to the conclusion that in the case of protons the collision energy is only limited by the field produced by the bending magnets.

1.2 The LHC Project

1.2.1 Motivations for the LHC

All evidence of the LEP experiments indicates that new physics lie at energies around $1\,TeV$. As previously mentioned it is impossible for the LEP to reach such high energy and luminosity values, so a new research instrument, the Large Hadron Collider (LHC), was originated and is presently under construction for the required energy and luminosity values. This superconducting, high–energy proton collider is unprecedented in terms of energy, luminosity, costs, size/complexity of experiments and human resources [5]. The LHC will be, upon its completion in 2005 and for the next twenty years, the most advanced research instrument of the world's high–energy physics community. The motivations for planing and performing such a huge project are:

- Origin of particle masses

  The experiments at LEP verified the standard model of electroweak interactions with a precision of 10^{-3} to 10^{-4}. However the origin of the particle masses and their distribution, which spans more than twelve orders of magnitude, are neither predicted nor explained. A possible process to endow particles with masses is their coupling with a particular field permeating space, the Higgs field, which would be mediated by the Higgs boson. Theoretical considerations and experimental searches for the Higgs boson indicate that its mass range would fall between $115\,GeV$ and about $1\,TeV$, well within reach of the LHC.

- Is the standard model the "ultimate theory"?

  Probably the SM is the low–energy approximation of a more general theory. Therefore it is necessary to have a high–energy machine to look for the manifestations for this theory. In addition the concept of the Grand Unified Theory, which predict the unification of the strengths of electromagnetic, weak and strong interactions at very high energy, would require amending the SM to include other particles, "supersymmetric" to the known ones (SUSY). Although this unification would only occur at energies far above those of the LHC collisions, its consequences could appear as new physics down to the TeV range accessible to the machine.

- Precise measurements

  There are two ways to find new physics: the discovery of new particles and phenomena, or to measure the properties of known particles as precisely as possible and find the deviations from the SM. Because of the high energy and the high luminosity of the LHC enormous rates of known particles discovered with other accelerators (W, Z, b- and top-quark, etc.) will be

produced. Therefore large statistics can be reached and it is possible to get precision measurements that will confirm the SM or require its modification.

- Many other open questions
  - Are quarks and leptons really elementary?
  - Are there additional families of (heavy) quarks and leptons?
  - Are there additional gauge bosons?
  - What is the origin of matter–antimatter asymmetry in the universe?
  - What is the nature of QCD–confinement?
  - Unexpected physics?
  - etc.

1.2.2 Machine performance and layout

The LHC is designed to use the $27\,km$ LEP tunnel and be fed by existing particle sources and pre–accelerators (Linac/Booster/PS/SPS), as it can be seen in Figure 1.1. The reuse of these accelerators as pre–injectors imposes an injection energy of $450\,GeV$, thus requiring a large dynamic range in energy. Some of the main performance parameters of the LHC as a proton collider are listed in Table 1.1.

The basic layout of the machine (Figure 1.2) consists of eight straight sections each approximately $528\,m$ long, available for detectors and insertion chains or utilities. The collisions will be produced and their products analyzed in four large experiments located in underground caverns around the machine.

The two proton–proton interaction experiments using high luminosity (ATLAS and CMS) are located at diametrically opposite straight sections. There are two more particles detection possibilities, i.e. ALICE which is a heavy–ion detector and LHC-B which is designed for precise measurements of CP violation and rare decays. These latter sections (Point 1, 5, 2 and 8) also contain the injection systems. The beams cross from one ring to the other only at these four locations.

The remaining four straight sections include the beam collimation systems (Point 3 and 7), the radio frequency systems (Point 4) and the beam dump insertion (Point 6) respectively [6].

The testing phase of the pre–series magnets has already started. After their thorough test, measurement and evaluation, the green light for mass production could be given by mid 2001. About four years will be needed for production test, installation and commissioning of the magnets. In 2006 the first beam tests are expected and first collisions half a year later.

Injection energy	450	GeV
Collision energy	7	TeV
Dipole field at $7\,TeV$	8.33	T
Operating temperature	1.9	K
Luminosity	10^{34}	$cm^{-2}\,s^{-1}$
Circulating current per beam	0.56	A
Stored energy per beam	350	MJ
Beam lifetime	22	h
Luminosity lifetime	10	h
Energy loss per turn	6.7	keV
Total radiated power per beam	3.8	kW

Table 1.1: LHC performance parameters

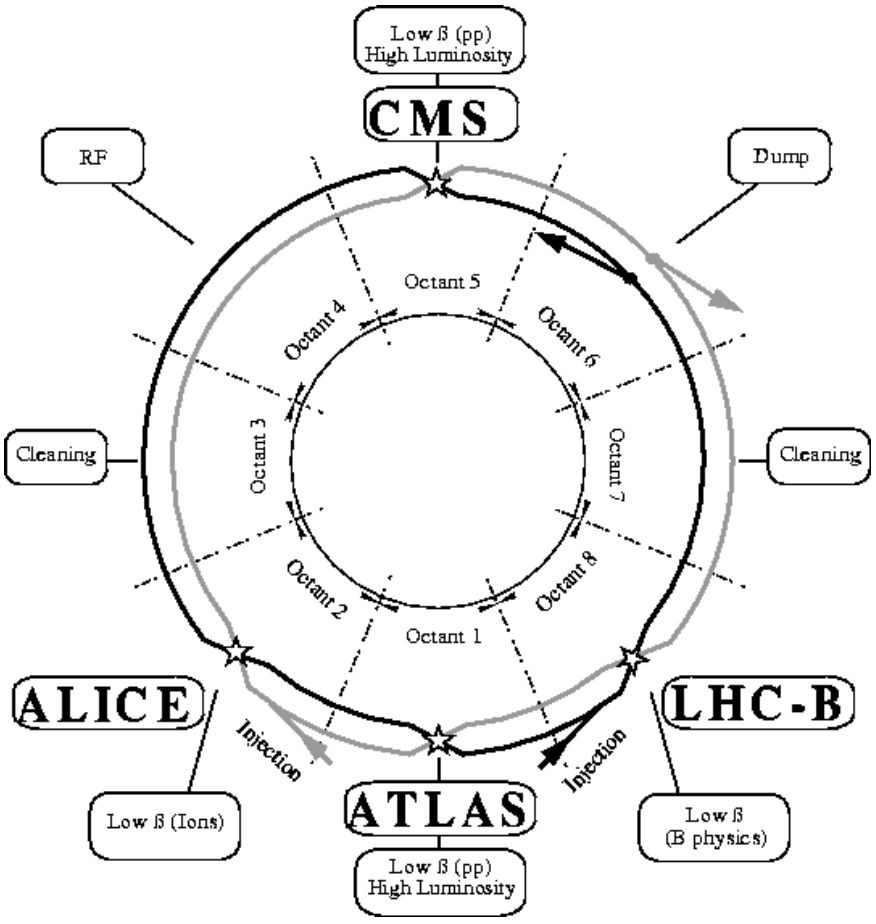

Figure 1.2: Schematic layout of the LHC

1.2.3 The magnet system

The Tevatron (Fermilab[1]) and HERA (Desy[2]) were pioneers in using superconducting magnets for accelerators. Both make use of classical NbTi superconductors cooled with normal liquid helium at a temperature slightly above $4.2\,K$, and their operational fields are below $5\,T$ ($\sim 4\,T$ for the Tevatron and $4.7\,T$ for HERA).

In the case of the LHC the circumference is given by the existing LEP tunnel, therefore a bending field of about $8.33\,T$ is required to reach a beam energy of $7\,TeV$. At present this high field can be reached reliably and economically by using the well known NbTi superconducting technology and cooling the magnets to a low temperature of $T \simeq 1.9\,K$ to increase the current carrying capacity versus field of the conductor.

For the LHC accelerator system several types of magnets will be used. The main dipole magnets are needed to bend the beam on a circular orbit. A positive charged particle on the designed orbit in the horizontal plane follows a bending trajectory in the presence of a vertical dipole field because of the Lorentz force. The quadrupole magnets provide focusing forces through their normalized field gradient. A field gradient of $223\,T/m$ will be used to focus the beam. In addition to these main magnets sextupole and decapole corrector magnets will be needed.

Since proton–proton colliders require two separate beam channels with fields equal in strength but opposite in directions, the compact "two–in–one" design was adopted, whereby the two beam channels and their corresponding sets of coils are inserted in an unique structure and in a single iron yoke and cryostat. By combining two sets of windings in a common mechanical and magnetic structure, the LHC magnets can be made more compact and efficient, as the stray flux of one aperture contributes to increasing the field in the neighboring one. The resulting cross talk between the twin apertures is not a drawback, as the magnets will be operated with the same field level in both apertures [7]. The main dipoles and quadrupoles are all of this twin–apertures design, while the corrector magnets are independent for each beam. This configuration not only saves space, which is imposed by the cross–section of the LEP tunnel, but gives a 25 percent cost saving over separate rings as well.

The main technological challenge of the LHC is the development and industrial production of 1232 superconducting main dipoles, 400 superconducting main quadrupoles and several thousand other superconducting magnets for correcting multipole errors, steering and colliding the beams, and increasing the luminosity in collision. All these magnets (see Table 1.2), which must produce a controlled field with a precision of 10^{-4}, are presently being series–produced by industry in Europe, India, Japan and USA. The LHC magnets are thus one of the most massive applications of superconductivity using $1200\,t$ of conductor including

[1]Fermi National Accelerator Laboratory near Chicago
[2]Deutsches Elektronen–Synchrotron in Hamburg

Type	Quantity	Purpose
MB	1232	Main dipole
MQ	400	Main quadrupole
MSCB	376	Combined chromaticity and closed–orbit corrector
MCS	2464	Sextupole for correcting dipole persistent currents
MCDO	1232	Octupole/Decapole for correcting dipole persistent currents
MO	336	Landau octupole for instability control
MQT	256	Trim quadrupole for lattice correction
MCB	266	Orbit correction dipole
MQM	100	Dispersion suppressor quadrupole
MQX	32	Low-β insertion quadrupole
MQY	20	Enlarged–aperture quadrupole

Table 1.2: Superconducting magnets in the LHC [8]

about $400\,t$ of NbTi alloy. The mass to be kept cool at $1.9\,K$ temperature will be about $30000\,t$, including only the dipoles, distributed over the $27\,km$ circumference [9]. Powering all superconducting magnet circuits in the LHC require feeding $3.4\,MA$ into the cryogenic helium environment. The conventional solution of vapor–cooled resistive current leads would require installation of significant extra refrigeration capacity. With the advent of practicalHigh–Temperature Superconductor (HTS) materials, and using the favorable cooling conditions available in the LHC cryogenic system, which is described bellow, HTS–based current leads have the potential of reducing the entropic load by a factor 3 with respect to their resistivecounterparts. Prototypes of such leads, manufactured by industry, are being tested and show promising results [10].

The use of superfluid helium ($T < 2.163\,K$ at $1\,bar$) as magnet coolant brings other advantages than lower operating temperature alone [11]. Its high specific heat, which is 2000 times that of the conductor per thinspace volume, and extremely low viscosity make it a prime component for stabilizing the windings against thermal disturbances. The large thermal conductivity permits to operate in a quasi–isothermal environment, thus minimizing the temperature differences associated with the extraction and transport of heat over long distances [12]. These properties allow to design a particularly simple and efficient cooling scheme by which the magnet active parts operate at $1.9\,K$ in a bath of static superfluid helium at atmospheric pressure [13].

Figure 1.3 shows the transverse cross–section of the main dipole. The design is based on an operational field of $8.33\,T$ corresponding to an operating current of $11800\,A$, the magnetic length has an amount of $14.3\,m$ and the coil inner diameter is $56\,mm$. The coils are held firmly in place and pre–compressed by stainless steel alloy collars common to both apertures, to guarantee parallelism of the field in the two beam channels. The yoke, vertically split in two halves, tightly fits

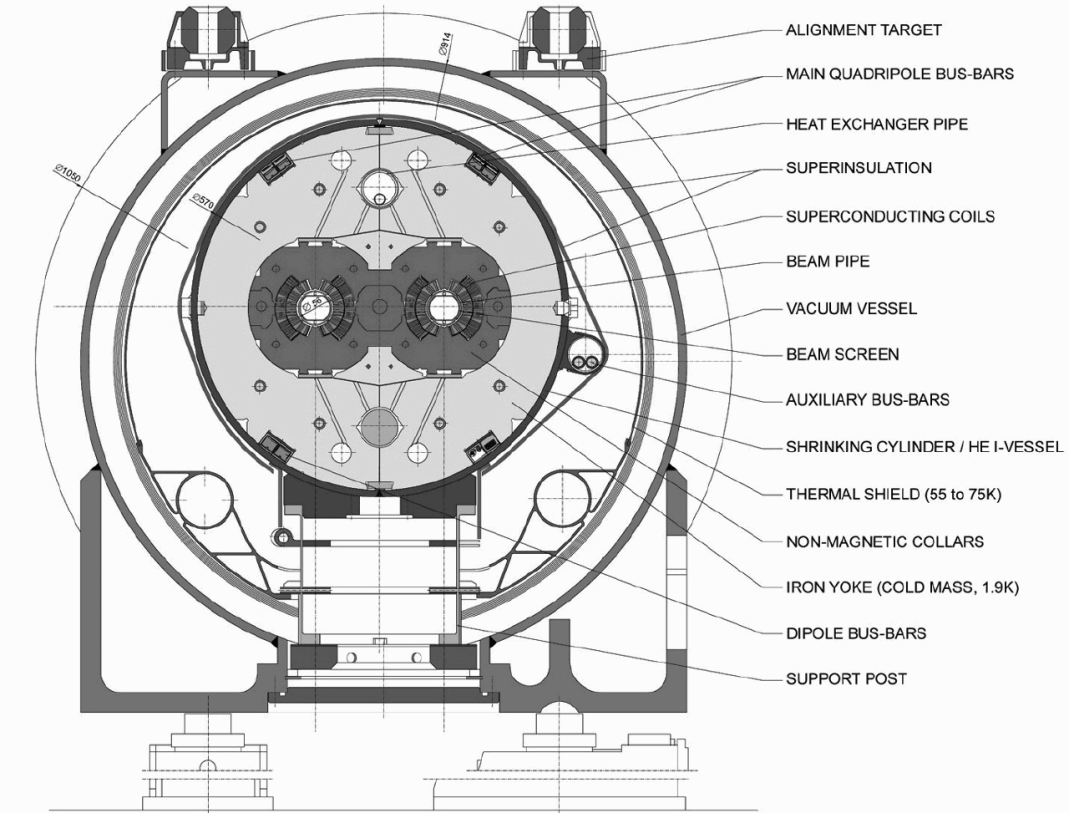

Figure 1.3: Transverse cross–section of the LHC twin aperture dipole in its cryostat.

and clamps the collars and is held together by an outer, welded stainless steel shrinking cylinder. The structure is designed to prevent any tensile stress in any part of the coils at all operating conditions. The shrinking cylinder is at the same time the outer shell of the helium tank, while the inner wall forms the beam vacuum chamber. The assembly between these two cylindrical walls, the so–called "cold mass", is kept at $1.9\,K$. In order to reduce the heat load on the cryogenic system at this very low temperature, the heat generated by the synchrotron radiation and the effect of beam induced currents in the resistive wall is intercepted by a beam screen. This is inserted within the vacuum chamber and is cooled by helium circulating at 5 to $20\,K$. Attached to the ends of dipole magnets are one small sextupole and one small decapole corrector to compensate the corresponding multipole errors of the main dipole resulting from persistent currents in conductors. Main and auxiliary bus–bars to feed the magnets of the arcs and the dispersion suppressors are located in grooves in the iron yokes and in auxiliary bus–bar attached to the cold mass [6] [9].

	Inner Layer	Outer Layer
Strand		
Diameter $[mm]$	1.065	0.825
Copper to superconductor ratio	1.6	1.9
Filament size $[\mu m]$	7	6
Number of filaments	8900	6500
Twist pitch $[mm]$	25	25
Critical current $[A]$		
at $10T$, $1.9K$	≥ 515	–
at $9T$, $1.9K$	–	≥ 380
Cable		
Number of strands	28	36
Cable dimension $[mm]$		
width	15.1	15.1
thin	1.736	1.362
thick	2.064	1.598
Transposition pitch $[mm]$	110	100
Critical current $[A]$		
at $10T$, $1.9K$	≥ 13750	–
at $9T$, $1.9K$	–	≥ 12950
dI_c/dB $[A/T]$	> 4800	> 3650

Table 1.3: Strand and cable characteristics of the main dipole magnets

1.3 Rutherford–type cables

The superconducting coils of the modern accelerator magnets are formed of two winding layers made with keystoned cables (Rutherford–type cables) of trapezoidal cross–section. This kind of cables are manufactured by flattening hollow tubular multistrand cables, which are compacted by rolling to packing factors up to 90%. The large compaction not only increases the overall current density but also reduces the average contact resistance between the strands. The strands are fully transposed with a transposition length (or cable pitch) which is usually about 6 to 8 times the cable width. In the inner layer of the dipole magnet a cable with 28 strands, each of $1.065\,mm$ in diameter is used. The cable of the outer layer has 36 strands, each of $0.825\,mm$ in diameter. The basic parameters of the cables and strands used for the LHC are given in Table 1.3.

Figure 1.4 contains an example of a Rutherford–type cable with the transposition pitch and the single strands on the left hand side. The second picture shows the corresponding cross–section of the multifilamentary NbTi strand with the central core, the filament zone and the outer shell. And the third one is an enlargement of a part of the strand showing the hexagonal bundles of filaments.

The basic cable insulation is composed of two polyimide layers wrapped

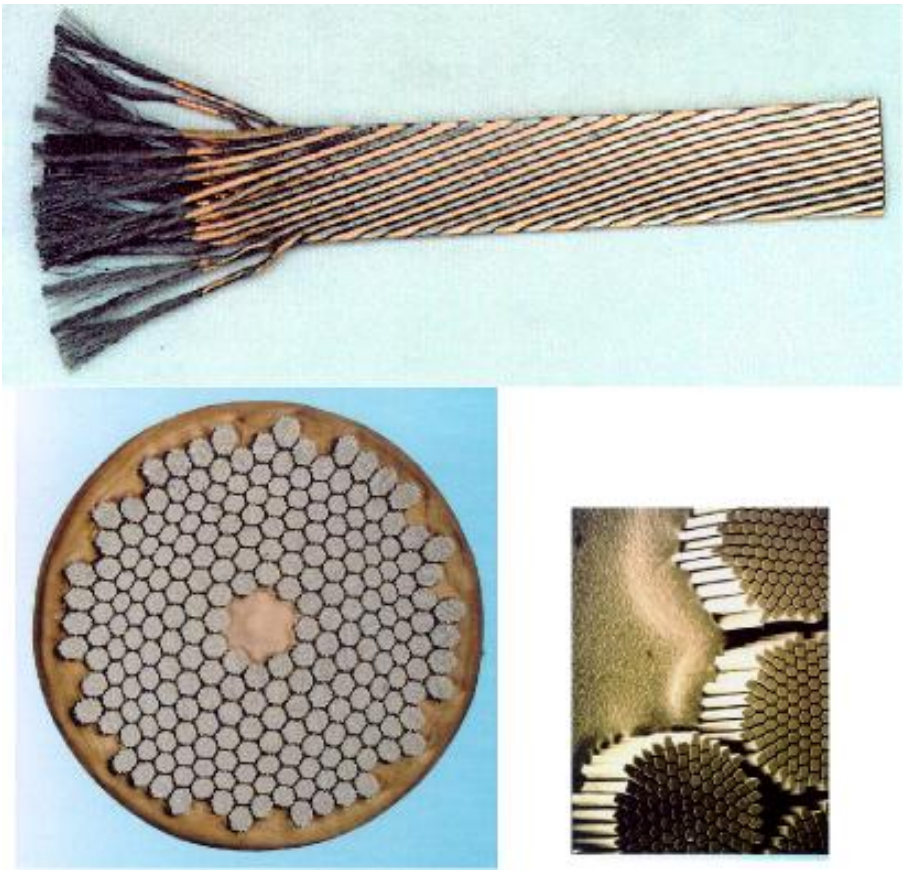

Figure 1.4: A Rutherford–type cable with the corresponding strands and the cross–section of such a multifilamentary strand with an enlargement of the filaments matrix.

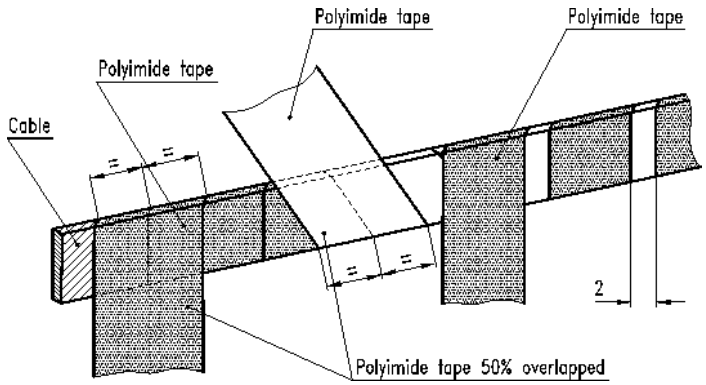

Figure 1.5: Conductor insulation with wraps of overlapping polyimide tape.

around the cable, with 50 overlapping, and another polyimide tape wrapped onto the cable and spaced by $2\,mm$ (see Figure 1.5). The resulting gap makes the coil porous by setting up channels for superfluid helium, without effecting the mechanical support between the turns.

The strands themselves consist of thousands of superconducting filaments (NbTi) twisted together and embedded in a matrix of high purity copper. The main reason for the subdivision into small filaments is the reduction of the filament magnetization which is the main cause of field distortions at weak excitation. Another advantage is the reduction of energy loss during (de-)excitation. Also cryostability can be reached from the high number of separate filaments, i.e. avoid flux jumping. If a filament should temporally be heated beyond the critical temperature the current is taken over by the copper for a short moment, allowing the NbTi to cool down and recover superconductivity. In order to fulfill these tasks the copper matrix must be as good electrical and thermal contact with the superconductor as possible. The electrical resistivity of the matrix should therefore be small, especially in the longitudinal direction. The RRR–value (Residual Resistivity Ratio) gives the ratio between the resistivity at $300\,K$ and $4\,K$ for zero field and is generally about 50 to 200 for practical NbTi superconductors. A common lay–out of the cross-section of such a multifilamentary strand (Figure 1.4) consists of a central core of normal–conducting material, a ring filled with many thin filaments embedded in a matrix and an outer shell of normal–conducting material, which is required to facilitate the wire production.

1.4 Current distribution inside the cables

In the accelerator the Rutherford–type cables are exposed to a changing magnetic field inducing various currents. These currents flow not only within the individual strands of the cable but also in and between the various strands of the cable. Due to the energy dissipation, the cable warms up locally so that the difference between the transport current and the critical current decreases. Additionally, the induced currents can also reduce directly the current margin at nominal ramp rate which can provoke a premature quench, i.e. a transition to the normal state. These additional currents can explain the reduction of the quench performance when the ramp rate increases. Therefore the study of these currents and the time behavior is of crucial importance for the field quality requirements for the LHC [14] as well as for magnet stability with respect to quench performance especially in real operating conditions of the machine.

In general four types of induced currents can be distinguished which differ with respect to the part of the conductor through which they flow, the characteristic loop length and the characteristic time [15]:

- Persistent currents (PCs) in the filaments (partially) shield the interior of the filaments against the external applied field. The magnitude of these

currents depends on the field and the history but, in first approximation, not on the field–sweep rate.

- Interfilament coupling currents (IFCCs) are induced by an external field variation and flow between and in the filaments of a strand. The magnitude of the IFCCs increases with increasing twist length of the filaments and decreasing resistivity of the matrix material. The IFCCs have a characteristic loop length equal to the twist pitch of the filaments, exhibit time constants of typically 0.01 to 0.1 s and cause the interfilament coupling loss.

- Interstrand coupling currents (ISCCs) are also induced by an external field variation and flow between and in the strands of the cable. The magnitude of the ISCCs increases with increasing twist length of the strands and decreasing electrical contact resistance between the strands. The ISCCs have a characteristic loop length equal to the twist pitch of the strands, exhibit time constants of typically 0.01 to 10 s and cause the interstrand coupling loss.

- Boundary–induced coupling currents (BICCs) are mainly induced by variations of the field–sweep rate and the contact resistances along the length of the cable. BICCs can flow in and between the strands of a cable and also in and between the filaments of the strands. The loop length and the characteristic time of the BICCs can be several orders of magnitude larger than those of the ISCCs. The additional power loss caused by the BICCs is dissipated in the contact resistances between the strands.

In the following mainly the interstrand coupling currents and the boundary–induced coupling currents will be discussed which are responsible for the uniform and the non–uniform current distribution inside the cable affecting the measured phenomena of the so–called Field Advance (FA) and the Periodic Field Pattern (PFP). As already described above an external field variation which is independent of the spacial coordinates produces an uniform current distribution which can explain the larger field values at the ramp down of a performed current cycle of a magnet. From these measurements an average value of the contact resistances along a part of the magnet length can be deduced.

The non–uniform current distribution has its origin in the BICCs, which are also called "supercurrents" in the literature. There are two parameters responsible for these currents. First the statistical spatial variation of the cross–contact resistance induces these currents. And the second one is a spatial variation of the field–sweep rate. This non–uniform current distribution is linked to another phenomenon which occurs in superconducting magnets.

Exact field measurements of accelerator prototype magnets revealed an axial periodic modulation of the magnetic field with a wave length equal to the cable transposition pitch length. In several measurements, discussed in Chapter 2, it

was found that the amplitude of this Periodic Field Pattern has a complex time and space dependence.

From measurements an estimation of the amplitude of the additional induced currents can be made. Also the influence of the current cycle parameters on the PFP are investigated and the time decay of the corresponding induced currents is studied. In addition the PFP was measured on different kind of magnets, short models with single and twin apertures and also full–scale prototypes and pre–series magnets.

1.5 Scope of the thesis

This thesis covers the effects of uniform and non–uniform current distribution inside Rutherford–type cables. Beside historical aspects and theoretical modeling the main part describes the measurements performed on LHC short dipole models and on LHC prototypes and pre–series dipoles. Also the impact of these additional currents on the performance of the LHC is discussed.

In detail the thesis is structured in the following order:

- Chapter two covers a historical review of experimental results of the periodic field pattern from the first observation at HERA, studies at BNL and last but not least already performed investigations on this topic at CERN.
- Chapter three gives a short overview of the existing theories dealing with a network model and a continuum model, respectively.
- Chapter four introduces the experimental equipment and measurement technique, which was used in this thesis. Especially the used Hall probe set–ups are described and the characteristics of the measured magnets are given.
- Chapter five presents the experimental results of the PFP–measurements and the so–called Field Advance (FA) measurements. Here also the data analysis and interpretations considering existing theories are given.
- Chapter six deals with the impact of the investigated additional currents on the quench performance of the LHC.
- Conclusion

Chapter 2

Historical Review

The effect of the Periodic Field Pattern (PFP) is directly linked to superconducting magnets. Thus the first observations and measurements dealing with the PFP were performed in the large accelerator laboratories using superconducting technology for the bending of the accelerated particles on their circle. This chapter gives an overview of experiments performed at DESY, BNL and CERN in chronological order.

2.1 First observation of the PFP at DESY

The Hadron–Electron Ring accelerator facility (HERA) is part of the Deutsches Elektron–Synchrotron (DESY) laboratory in Hamburg, Germany. The construction was finished in 1990 and one year later the first electron–proton collision took place. The task of HERA is to collide protons with an energy of $820\,GeV$ and $30\,GeV$ electrons with a luminosity of $5 \cdot 10^{31}\,cm^{-2}\,s^{-1}$. The accelerator ring has a length of $6.3\,km$ and the tunnel contains the superconducting proton storage ring and the electron storage ring. The injection energy of the proton ring which requires a dipole current of $250\,A$ is $40\,GeV$. The nominal field for the main bending dipole magnets is $4.682\,T$ corresponding to a nominal operation current of $5027\,A$. The whole magnet system of HERA contains 650 superconducting dipole and quadrupole magnets and more than 1500 superconducting corrector thinspaces [16].

During an experimental study of the time dependence of persistent current multipoles with a HERA dipole magnet, it was found that the field exhibits a sinusoidal structure along the axis of the magnet. The first evidence for this unexpected periodic field pattern in a superconducting magnet is shown in Figure 2.1, curve (a). The magnet was subjected to a current cycle typical for accelerator operation ($0 \rightarrow 5500\,A \rightarrow 50\,A \rightarrow 250\,A$) and then kept at $250\,A$ for one hour. An almost sinusoidal structure was observed with a remarkably large amplitude. After going through another cycle $250\,A \rightarrow 2000\,A \rightarrow 250\,A$ curve (b)

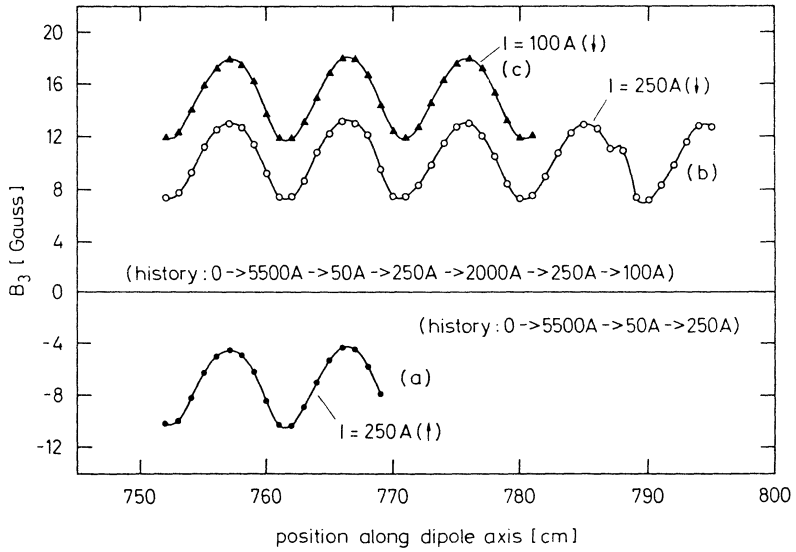

Figure 2.1: Sextupole field B_3 at $r_0 = 25\,mm$ as a function of the coordinate z along the axis of a HERA dipole [17].

was obtained and lowering the current to $100\,A$ finally curve (c).

For the investigation of this new effect three different measurement techniques were used to extract the PFP from the main dipole field, the sextupole harmonic component and the other multipoles in about 10 magnets. Because of the limited time and spatial resolution of rotating pick up coils, which have generally a very good sensitivity and precision, a sensor consisting of three Hall probes was developed to study the behavior of the sextupole field. The probes were temperature controlled and they were powered with an alternating current. For the dipole field a nuclear magnetic resonance detector was used. Finally, a $2\,cm$ long tangential pickup coil was developed to determine all other normal and skew harmonics.

Several different measurements were performed mainly on the sextupole field of the dipole magnets but also on the other harmonics. The wavelength of the PFP is comparable with the transposition pitch of the cable and the effect is related to the superconducting currents in the cable, because it can only be observed below the critical temperature T_c of the cable material (NbTi). After the magnet was exposed to a certain power history the periodic structure persists for more than twelve hours with zero transport current in the coil. Furthermore it was found that the amplitudes depend strongly on the highest excitation of the magnet before performing the measurements at low field, but the structure is independent on $\dot{B} = dB/dt$. The phase of the structure is not perfectly stable, slight shifts have been observed [17].

2.2 PFP studies at BNL

The Superconducting Super Collider (SSC) project was recommended by the High Energy Physics Advisory Panel (HEPAP) of the US department of energy in 1983. A proton–proton collider with an energy of $20\,TeV$ per beam and a luminosity of $5 \cdot 10^{33}\,cm^{-2}\,s^{-1}$ was launched. For the accelerator complex it was foreseen to build in total four rings, the Low Energy Booster consisting of a $600\,m$ circumference ring filled with resistive magnets, the Medium Energy Booster consisting of a ring of $4\,km$ in circumference again using resistive magnet technology, the High Energy Booster consisting of $10.8\,km$ circumference ring filled with superconducting magnets and finally the $87.1\,km$ collider ring in which the protons were housed one above the other. A standard dipole was designed with a maximum field of $6.6\,T$. The total number of superconducting dipoles was 7680. The whole project was terminated because of economic reasons by a Congress decision in 1993 [18].

In the Brookhaven National Laboratory (BNL) a series of measurements with superconducting dipole magnets for the SSC were performed referring to the PFP. Because of their small spatial extent and relatively high sensitivity Hall probes were used for measuring the magnetic field. In one experimental arrangement two Hall probes were mounted on the magnet axis separated by one half of the cable transposition width with a third probe situated at the maximum radius and aligned with one of the axis probes. It was possible to move this array in axial and rotational direction. Therefor the oscillations in the dipole field could be observed directly while the harmonic components were determined by rotating the assembly and analyzing the difference between the axial and radial probes. A second Hall probes set–up in which three elements were positioned at the same radius but separated by 120 degrees was also used to measure directly the sextupole component. In total fifteen dipoles have been examined including ten short and long SSC prototype magnets. Since the field variations are small (typically a few gauss) the PFP is most apparent at low fields. After a high field cycle in which the current has been maintained at the peak value for several minutes and the shut–off of the power supply all magnets showed an axial pattern.

The oscillation is particularly pronounced at high fields, as can be seen from Figure 2.2 where the sextupole in a SSC dipole is plotted for magnet currents of 650 and $7000\,A$. At high field the oscillation amplitude is much larger than the average value of the sextupole field. It should be noted that the detailed behavior is not representative for other magnets except for the general trend that the oscillation becomes more pronounced at higher excitation of the magnets.

Despite the fact that axial variations seem to be universal in all dipole cables, the differences in the way the patterns grow and decay is quite remarkable. Each of the magnets examined so far has shown some unique features and it has not been possible to predict anything beyond the fact that an oscillation with a wavelength matching to the cable pitch length will be observed. Nevertheless some

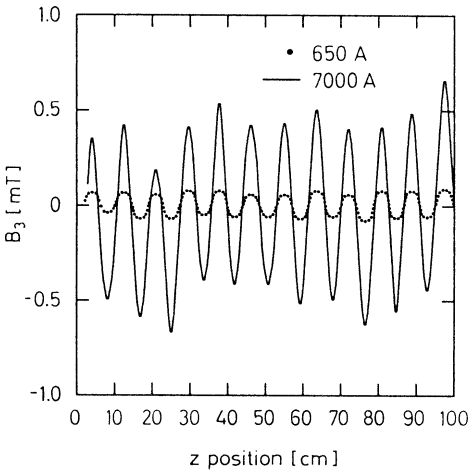

Figure 2.2: Longitudinal periodicity of the sextupole field in a SSC dipole at 650 A and 7000 A [19].

conclusions can be done. The magnitude of the oscillation increases with both the maximum field achieved during the energizing cycle and the time spent at high field. For a given field level the amplitude grows exponentially with time much like the voltage on a charging capacitor with a time constant of typically 500 s. After the pattern has been established it decays in a complex way and can only be completely erased by raising the conductor above its transition temperature [19].

Thus another experiments were made at the BNL to investigate the decay of the PFP parameters [20]. After a symmetrical energizing cycle with a ramp rate of 60 A/s, a flat–top current of 6400 A and a waiting time of 15 min at the flat–top the power supply of the SSC model magnet was turned off. Afterwards the remanent field oscillation amplitude and the average dipole field were measured as a function of time. The curve of the average decay can be represented by a combination of three exponentials having time constants of 60, 2200 and 400000 seconds, with respective amplitudes of 0.46, 0.042 and 0.59 mT. The oscillation amplitude shows no decrease during the first 100 s, but during the next 2000 s it changes appreciably before stabilizing to a very slow decay.

Other experiments showing the dependency of the PFP on the ramp rate and the inter–strand resistance can be found in [21]. Magnets with a very low inter–strand resistance (6 $\mu\Omega$) exhibit a large axial oscillation in the sextupole field between up and down ramps which is rate dependent. When the strand resistance is high (79 $\mu\Omega$) the amplitude of this oscillation is almost independent of the ramp rate. The used values for the inter–strand resistances were deduced from loss measurements taking into account the effects of inter–strand coupling.

2.3 Historical studies at CERN

2.3.1 Measurements on a Nb_3Sn dipole model

In a collaboration between the university of Twente in the Netherlands and CERN magnets constructed with Nb_3Sn cables were tested for the LHC project. Specially the performance of the single aperture $11\,T$ Nb_3Sn model dipole magnet MSUT has been studied experimentally in 1995 at the first and in 1997 at the second cool–down [22]. Both programs covered extensive magnetic measurements, AC loss measurements and a quench study program.

The results of these studies have shown a relatively fast decrease of the quench current with increasing ramp rate. A maximum ratio of

$$\frac{dI_Q}{d\dot{I}} \approx -150\,A/\,As^{-1}$$

was measured where I_Q indicates the quench current and $\dot{I}$ is the ramp rate. This ramp rate sensitivity depends on the amplitude and the distribution of the induced coupling currents which are also responsible for the PFP.

2.3.2 Measurements on long LHC dipole models

The first experiments referring to the PFP at CERN were performed on the ten meter dipole model MTP1 A1. The axial variations of the field were measured by a $30\,mm$ long coil placed at the end of a rotating shaft which could be displaced axially with high precision. The PFP amplitude is measured to be of about the same at the LHC injection field of $0.6\,T$ and at a field level of $8.5\,T$. Additional the amplitude and the phase of these oscillations vary with time in the first few minutes after stabilization at $0.38\,T$ following a ramp from high field. This time dependence gives a corresponding time constant of about 2 minutes [23].

Another measurements were performed on the field quality of two $10\,m$ long models of the main LHC bending dipoles MTP1 A3 and MTP1 N2. The field was measured with two rotating coil systems. One was a $30\,mm$ long single coil where the measurements taken at successive cycles and adjacent positions had to be synchronized to reconstruct the periodic pattern. The other system consisting of an array of 7 coils covered a length of $175\,mm$, longer than a twist pitch of the cable which is of the order of 110 to $120\,mm$. Therefore it was possible to derive directly the PFP parameters on all harmonics from a fit of points measured simultaneously. Measurements were performed throughout the powering cycles of different ramp rates, in the range of $10\,A/s$ to $50\,A/s$, and at different positions along the magnet bore.

The experiments showed that the amplitudes of the PFP in the sextupole component of the magnetic field differed between the two measured magnets in one order of magnitude, although the magnets were nominally identical and the

powering history was similar. As a second result the time decay of the amplitude can be mentioned which shows two phases. In the first one the time constant is in the range of 100 to 300 s. Afterwards the decay leads to slower drift with much longer time constants being larger than 1000 s. Finally it was observed that the PFP was stronger closer to the magnet ends than in the center of the magnet. Furthermore, also the decay of the amplitude is stronger approaching the end [24].

2.3.3 Measurements on a short LHC dipole model

The measurements were performed on the one meter long, twin aperture LHC dipole model MBSMT1. Three arrays of short radial coils consisting of five adjacent coil sections each were used to measure the field. The length of one coil group is approximately 125 mm which is larger than the nominal inner cable twist pitch of 105 mm. The three coil groups are located on different places in the magnet bore. One at the beginning of the straight section of the coil winding at the connection end. The second group is placed in the center of the magnet. And the last one covers the end of the straight part of the coil winding, in the non–winding end. The acquisition allowed simultaneous read–out of five coils, i.e. a complete group. Therefore the field can be measured at the same time as a function of the coil position along the magnet bore axis.

The sextupole component of the field was extracted and the PFP was found in every measurement that was performed. But it has different features in the three positions of the coil groups along the magnet. In the first part of the magnet a strong longitudinal field gradient is observed, so that it is not possible to recognize a precise and repeatable pattern. However the other two coil sections exhibit a strong oscillation with a period equal to the inner cable twist pitch.

Two types of measurement cycles were performed. In the first series of test the magnet was ramped–up in a single step from a small current to a flat–top current at constant ramp rate. For three different flat–top currents (2 kA, 5 kA and 8 kA) the amplitude of the PFP increases linearly. In contrary the amplitude is independent of the three ramp rates 50 A/s, 200 A/s and 450 A/s. On the flat–top the amplitude shows a time decay which can be interpreted as a superposition of exponentials with several time constants.

The second type of cycles reproduces the typical operating current cycle for LHC dipole magnet. The magnet was pre–cycled ramping at 50 A/s to maximum current, remaining at flat–top for a certain time, and finally ramping down at $-50\,A/s$ to a minimum current of 50 A. Afterwards the current was increased up to 810 A with a ramp–up of 1 A/s followed by a 1000 s constant current period, corresponding to the injection phase in the LHC, and finally the current was ramped up to about 1500 A. In this case the evolution of the pattern amplitude is more complex. Nevertheless is was observed that the PFP amplitude is proportional to the pre–cycle flat–top duration. Additional longer flat–top times

correspond to larger variations of the pattern during the constant current phase. During the slow ramps ($1\,A/s$) to and from injection the amplitude does not depend on the pre–cycle [25].

Chapter 3

Models for the Periodic Field Pattern

Two main kinds of models are described in the literature in order to calculate the current distribution in superconducting cables. The network model originated in the work of G. H. Morgan [26] and further developed by A. Akhmetov [29] and A. P. Verweij [15] considers the flat cable as a network of superconducting strands interconnected via discrete resistive contacts. It is possible to describe phenomena like, for instance, energy loss and field distortion in magnets of complicated geometry, in a very detailed way, but calculations require large computer resources. Additional the application of these models is limited to the stationary case or to short ideal cables with few strands.

The second section of this chapter gives a rough overview of several publications of L. Krempasky and C. Schmidt dealing with a diffusion solution of the problem. After a two–wire cable was introduced [31], it was applied for the ramp–rate limitation in large superconducting magnets [32] and for an experimental verification of this effect [34]. The influence of these supercurrents on the stability of superconducting magnets is discussed in [33]. A more general aspect on the time constants in superconductors can be found in [35] and [36], respectively.

3.1 Network Models

3.1.1 One dimensional model

The first developed model describing interstrand eddy currents for braided conductors by Morgan can be used to show the principal of a network of wires [26]. For the simplest way the Rutherford cable is replaced by a two–layer network of wires that is connected by small resistors at the cross–over points [27]. A schematic drawing of a cable with four strands is given in Figure 3.1. Afterwards

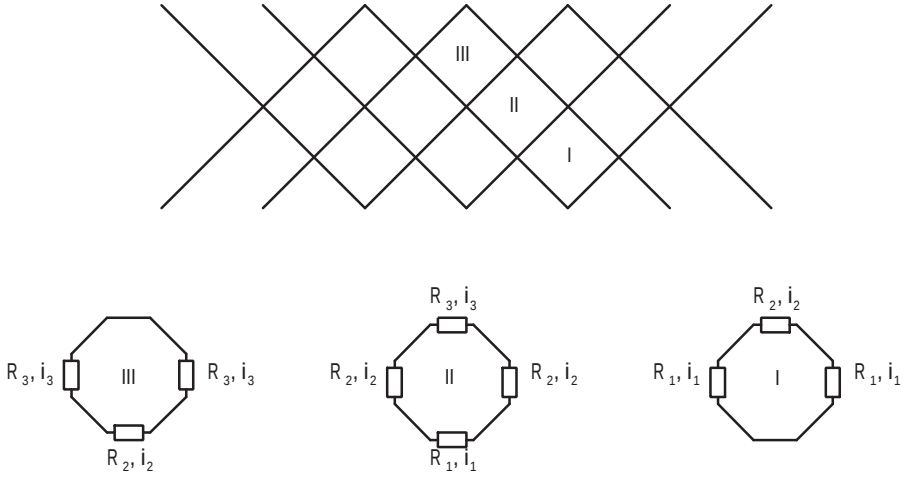

Figure 3.1: A simple network model of a Rutherford–type cable consisting of four strands. Below the three different loops are shown with the corresponding cross–over resistances and currents.

the results will be expanded to the general case of N strands for a more realistic cable [28].

Considering the four strand cable three different loops can be distinguished, as it can be seen in Figure 3.1. Using the contact resistances and the corresponding currents in the cross–over points the magnetic flux can be estimated by neglecting a dependence on the longitudinal coordinate.

$$\begin{aligned} \frac{d\Phi_1}{dt} &= 2R_1 i_1 - R_2 i_2 \\ \frac{d\Phi_2}{dt} &= 2R_2 i_2 - R_1 i_1 - R_3 i_3 \\ \frac{d\Phi_3}{dt} &= 2R_3 i_3 - R_2 i_2 \end{aligned} \tag{3.1}$$

These three equations can be solved analytically for the unknowns i_1, i_2 and i_3.

$$\begin{aligned} i_1 &= \frac{1}{4R_1}\left[3\frac{d\Phi_1}{dt} + 2\frac{d\Phi_2}{dt} + \frac{d\Phi_3}{dt}\right] \\ i_2 &= 2\frac{R_1}{R_2} i_1 - \frac{1}{R_2}\frac{d\Phi_1}{dt} = \frac{1}{2R_2}\left[\frac{d\Phi_1}{dt} + 2\frac{d\Phi_2}{dt} + \frac{d\Phi_3}{dt}\right] \\ i_3 &= 3\frac{R_1}{R_3} i_1 - \frac{1}{R_3}\left[2\frac{d\Phi_1}{dt} + \frac{d\Phi_2}{dt}\right] = \frac{1}{4R_3}\left[\frac{d\Phi_1}{dt} + 2\frac{d\Phi_2}{dt} + 3\frac{d\Phi_3}{dt}\right] \end{aligned} \tag{3.2}$$

For the general case of N strands the number for the different loops become $N-1$, and they are labelled by the letter n with $1 \leq n \leq N-1$. Thus the

Equations 3.1 change to

$$\frac{d\Phi_n}{dt} = 2R_n i_n - R_{n-1} i_{n-1} - R_{n+1} i_{n+1} \tag{3.3}$$

for the inner loops ($2 \leq n \leq N-2$), while at the edges of the cable we have

$$\begin{aligned} \frac{d\Phi_1}{dt} &= 2R_1 i_1 - R_2 i_2 \\ \frac{d\Phi_{N-1}}{dt} &= 2R_{N-1} i_{N-1} - R_{N-2} i_{N-2} \quad . \end{aligned} \tag{3.4}$$

The solutions for the cross–over currents i_n, corresponding to Equations 3.2 are than

$$\begin{aligned} i_1 &= \frac{1}{NR_1} \sum_{k=1}^{N-1} (N-k) \frac{d\Phi_k}{dt} \\ i_n &= n\frac{R_1}{R_n} i_1 - \frac{1}{R_n} \sum_{k=1}^{n-1} (n-k) \frac{d\Phi_k}{dt} \qquad 2 \leq n \leq N-1 \quad . \end{aligned} \tag{3.5}$$

Furthermore, assuming that the crossover resistances and the elementary fluxes are all equal, it is easy to express the solution in a closed form

$$i_n = \frac{n\,(N-n)}{2R_c} \frac{d\Phi}{dt} \qquad 1 \leq n \leq N-1 \tag{3.6}$$

with the sum $\sum_{k=1}^{N-1} (N-k) = \frac{N\,(N-1)}{2}$ of Equation 3.5.

The power W dissipated by the cross–over currents per cable thinspace length, where l_p is the transposition pitch of the cable, is

$$\begin{aligned} W &= \frac{N}{l_p} \sum_{n=1}^{N-1} R_c i_n^2 = \frac{N}{4 l_p R_c} \left(\frac{d\Phi}{dt}\right)^2 \sum_{n=1}^{N-1} \left[n^2\,(N-n)^2\right] = \\ &= \frac{N^2\,(N^4-1)}{120 l_p R_c} \left(\frac{d\Phi}{dt}\right)^2 \end{aligned} \tag{3.7}$$

using the sum $\sum_{n=1}^{N-1} \left[n^2\,(N-n)^2\right] = \frac{N\,(N^4-1)}{30}$.

At last we consider that there are $N\,(N-1)$ elementary loops per cable pitch length. Therefore an estimate of the flux is given by the following

$$\Phi \approx \frac{h l_p}{N\,(N-1)} B \tag{3.8}$$

where h is the cable width and B is the supposedly uniform component of the magnetic flux density perpendicular to the cable. This results in

$$W \approx \frac{(N^4-1)\,h^2 l_p}{120\,(N-1)^2\,R_c}\left(\frac{dB}{dt}\right)^2 \tag{3.9}$$

and for $N \gg 1$

$$W \approx \frac{N^2 h^2 l_p}{120 R_c}\left(\frac{dB}{dt}\right)^2 . \tag{3.10}$$

3.1.2 Two dimensional model

Considering now a dependency of the induced cross–over currents $i_{k,n}$ also from the longitudinal index k and from the transverse index n, the previously treated one dimensional model can be extended [29]. With the assumption of an uniform cross–over resistance both across and along the cable and an uniform magnetic flux along the cable, but allowing for a flux variation transverse to the cable, the cross–over currents $i_{k,n}$ exhibit a longitudinal periodicity, i.e. $i_{k+N,n} = i_n$. The periodicity interval is identical with the cable twist pitch length l_p. We can illustrate this again by using the four strand model of Figure 3.1. The Equation 3.1 for the magnetic flux have to be modified to incorporate the longitudinal dependence.

$$\begin{aligned}
\frac{1}{R_c}\frac{d\Phi_1}{dt} &= i_{k,1} + i_{k+1,1} - i_{k,2} \\
\frac{1}{R_c}\frac{d\Phi_2}{dt} &= i_{k,2} + i_{k+1,2} - i_{k+1,1} - i_{k+1,3} \\
\frac{1}{R_c}\frac{d\Phi_3}{dt} &= i_{k,3} + i_{k+1,3} - i_{k,2}
\end{aligned} \tag{3.11}$$

From these equations once can compute the currents at position $k+1$ from the values at position k. For this purpose it is convenient to use matrix notation. We define a 3×3 (generally $(N-1) \times (N-1)$) matrix $\mathbf{A}$ by

$$\mathbf{A} = \begin{pmatrix} -1 & 1 & 0 \\ -1 & 1 & -1 \\ 0 & 1 & -1 \end{pmatrix} \tag{3.12}$$

and the vectors

$$\mathbf{I}_k = \begin{pmatrix} i_{k,1} \\ i_{k,2} \\ i_{k,3} \end{pmatrix} \qquad \text{and} \qquad \Phi = \begin{pmatrix} \Phi_1 \\ \Phi_1 + \Phi_2 + \Phi_3 \\ \Phi_3 \end{pmatrix} . \tag{3.13}$$

The Equations 3.11 can then be rewritten as

$$\mathbf{I}_{k+1} = \mathbf{A} \cdot \mathbf{I}_k + \frac{1}{R_c}\frac{d\Phi}{dt} \ . \tag{3.14}$$

For the general case of a N strand cable the matrix $\mathbf{A}$ is defined that

$$\mathbf{A}^N = \mathbf{1} \qquad \text{and} \qquad \sum_{k=0}^{N-1} \mathbf{A}^k = 0 \tag{3.15}$$

is fulfilled, and Equation 3.14 becomes to

$$\mathbf{I}_{k+N} = \mathbf{A}^N \cdot \mathbf{I}_k + \sum_{k=0}^{N-1} \mathbf{A}^k \cdot \frac{1}{R_c}\frac{d\Phi}{dt} = \mathbf{I}_k \ . \tag{3.16}$$

This shows explicitly that the cross–over currents are periodic in the longitudinal index k with a period N, the number of strands in the cable. This means that the cross–over current between any two strands of the cable is the same after every pitch length l_p.

3.2 Continuum Models

The effect of the PFP can be explained by additional currents between the strands of superconducting cables. These currents flow over a large length and superimposed to the transport current. The so–called "supercurrents" are induced by a variable field rate $\dot{B} = dB/dt$ along the length of a superconducting cable. They depend sensitively on the exact geometry of the cable and on the field distribution, and can in principle not be avoided completely [32].

The coincidence of the wavelength of the magnetic field oscillations with the cable transposition pitch suggests that slowly decaying current loops exist in the cable. These loops consist of currents flowing along the cable through one set of strands and returning through another set of strands [30].

3.2.1 The two–strand model

In a first step we use for an explanation of the PFP effect the approach of a cable composed of only two wires, which allows a comprehensive treatment of the problem. As it can be seen in Figure 3.2 the two wires are twisted with a twist length l_p and lie in a plane. The total cable length is represented by l_0. Such an arrangement is usually called a Rutherford–type cable. The wires are connected at every half twist pitch by a cross–contact resistance, R_c. This cross–contact resistance is a constant in the ideal case, but scatters more or less in a real cable.

As the simplest case we consider that only one half twist pitch loop in the middle of the cable, $z = l_0/2$, is exposed to a constant magnetic field variation

$\dot{B} = dB/dt = const$, while $\dot{B}$ vanishes elsewhere. The driving voltage in the loop is

$$U = \iint \dot{B} df \tag{3.17}$$

the integral being taken over the loop area. As we have assumed a constant field sweep rate, the driving voltage also is constant and depends only on the length of b where $\dot{B} \neq 0$. In our example this is one half twist pitch loop, $b = l_p/2$, and thus Equation 3.17 becomes to

$$U = \frac{bw}{2}\dot{B} = \frac{l_p w}{4}\dot{B} \ . \tag{3.18}$$

The case of a single loop exposed to $\dot{B}$ is not completely hypothetical. It is relevant for accelerator dipoles, were $\dot{B}$ is constant along the length of one half turn of the winding, but is different over a small cable length around the ends of the magnet.

After a time $t \gg \tau$, where τ is the largest time constant appearing in the system, the so–called steady state supercurrent will flow in the cable. This current depend only on the geometry and the contact resistances of the cable. The equivalent circuit for this case reduces to that shown in Figure 3.3, with a driving voltage, U, and two resistances. R is here the value of contact resistances of half the cable length in parallel. The current flowing around the loop is then

$$I_{\max} = \frac{U}{2R} = \frac{U}{2R_c}\frac{l_0}{l_p} = \frac{UGl_0}{4} \tag{3.19}$$

with the transverse electric conductivity per thinspace length, G, which will be described later.

Since the current $I_{\max}$ flows through all the contacts in parallel at the left- and right hand sides of the loop, we get a stepwise decreasing longitudinal current $I(z)$ towards both ends of the cable, with the maximum at the center of the cable. Assuming that the whole length of the two–strand cable l_0 is much larger than the number of half twist pitch loops, i.e. $l_p/l_0 \to 0$, the longitudinal current $I(z)$ becomes a smooth solid triangle–like function. Figure 3.4 shows the shape of this current in one strand, a current of the same magnitude flows in opposite direction in the other strand.

A Fourier transformation of this steady state solution can be performed, which has the general form

$$I(z) = \sum_{n=1}^{\infty} b_n \cdot \sin\left(\frac{n\pi z}{l_0}\right) \ . \tag{3.20}$$

For the simple case of the triangle–like function in Figure 3.4 the coefficients b_n become

$$b_n = (-1)^{\frac{n-1}{2}} \cdot \frac{8I_{\max}}{\pi^2 n^2} \tag{3.21}$$

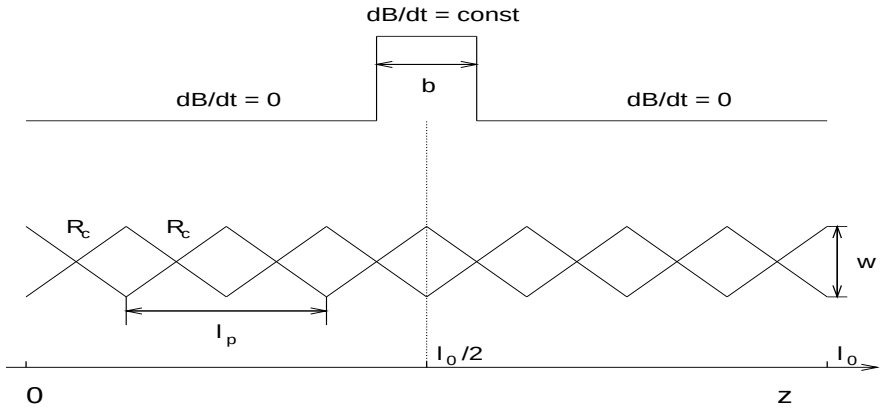

Figure 3.2: The two–strand cable with one half twist pitch loop exposed to a time–varying magnetic field, $\dot{B}$, in the centre of the cable at $z = l_0/2$.

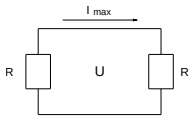

Figure 3.3: Equivalent circuit in the two–strand model, where R is the value of all the cross–contact resistances in parallel at one side of the $\dot{B}$-loop.

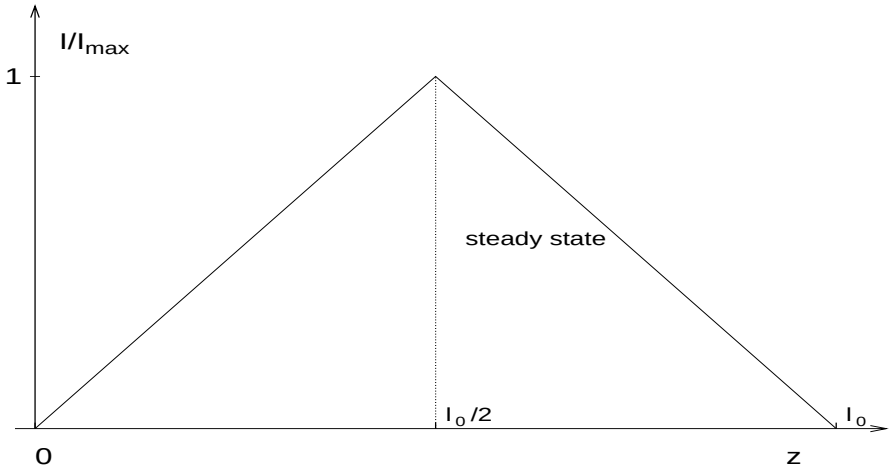

Figure 3.4: Corresponding "steady state" supercurrent for a time–varying magnetic field in the centre of the cable.

with $n = 1, 3, 5, ...\infty$. The even coefficients $b_2, b_4, ...$ are zero. This results in

$$I(z) = \frac{8I_{\max}}{\pi^2} \cdot \sum_{n=1,3,5,...}^{\infty} \frac{(-1)^{\frac{n-1}{2}}}{n^2} \cdot \sin\left(\frac{n\pi z}{l_0}\right) . \tag{3.22}$$

For the above mentioned case of $l_p \ll l_0$ and for equal cross–contact resistances we may treat the two–wire system as a continuous transmission line and we can introduce a transverse conductivity per thinspace length between both wires

$$G = \frac{2}{R_c l_p} . \tag{3.23}$$

Furthermore the inductance of the cable per thinspace length can be written as

$$L = \frac{\mu_0}{\pi}\left[\ln\left(\frac{w}{d}\right) + \frac{1}{4}\right] \tag{3.24}$$

where μ_0 is the magnetic permeability of the vacuum, w is the width of the cable and d is the strand diameter.

Steady state supercurrents are established, however, only after time $t \gg \tau$ of continuously changing magnetic field. In the usual case the duration of the field sweep $\dot{B}$ will be much smaller than the time constant τ and the current $\pm I(z,t)$ in the wires must fulfill the differential equation of a symmetrical two–wire transmission line

$$\frac{\partial^2 I(z,t)}{\partial z^2} = LC\frac{\partial^2 I(z,t)}{\partial t^2} + (R'C + LG)\frac{\partial I(z,t)}{\partial t} + R'GI(z,t) \tag{3.25}$$

which reduces for zero longitudinal resistance and zero transverse capacitance ($R' = 0$, $C = 0$) to the diffusion equation

$$\frac{\partial^2 I(z,t)}{\partial z^2} = LG\frac{\partial I(z,t)}{\partial t} . \tag{3.26}$$

The condition at a constant diffusity $D = (LG)^{-1}$ must be fulfilled and the boundary condition is $I(0,t) \equiv I(l_0,t) \equiv 0$.

For the charging period of the magnet, when $\dot{B}$ is switched on at time $t = 0$, we get the solution by multiplying each term under the sum in Equation 3.22 by $\left(1 - e^{-\frac{t}{\tau_n}}\right)$, i.e.

$$I(z,t) = \frac{8I_{\max}}{\pi^2} \cdot \sum_{n=1,3,5,...}^{\infty} \frac{(-1)^{\frac{n-1}{2}}}{n^2} \cdot \sin\left(\frac{n\pi z}{l_0}\right) \cdot \left(1 - e^{-\frac{t}{\tau_n}}\right) \tag{3.27}$$

with

$$\tau_n = \frac{\tau}{n^2} . \tag{3.28}$$

The time constant τ in Equation 3.28 is determined by the length of the cable and by the inductance and transverse conductance per thinspace length. It is given by

$$\tau = \frac{LGl_0^2}{\pi} \ . \tag{3.29}$$

If charging of a magnet is stopped, i.e. $\dot{B}$ becomes zero at time t_1, the terms under the sum in Equation 3.27 at $t = t_1$ decay with their corresponding time constants and we obtain for $t > t_1$

$$I\left(z, t > t_1\right) = \frac{8I_{\max}}{\pi^2} \cdot \sum_{n=1,3,5,\ldots}^{\infty} \frac{(-1)^{\frac{n-1}{2}}}{n^2} \cdot \sin\left(\frac{n\pi z}{l_0}\right) \cdot \left(1 - e^{-\frac{t_1}{\tau_n}}\right) \cdot e^{-\frac{t-t_1}{\tau_n}} \tag{3.30}$$

It is important to note, that the magnitude of the currents depends strongly on the exact geometry and number of half twist pitch loops exposed to $\dot{B}$ [34]. If for example the $\dot{B}$ region b extends over two loops, the resulting current will be close to zero [31]. In this case coupling currents of opposite direction (due to the twist) are induced in these loops and cancel each other completely.

Both Equations 3.27 and 3.30 give the complete time–dependent solution for the case where a field sweep rate $\dot{B}$ is applied to the two–wire cable during a time t_1. If some time later, another field sweep rate $\dot{B}'$ is applied, e.g. discharging the magnet, supercurrents induced by this second field sweep are calculated and simply added to the decaying currents of the first field sweep. For discharging with the same field rate the equations are the same but with the coefficients b_n of Equation 3.21 multiplied by (-1). This procedure allows, in principle, to calculate the supercurrents for an arbitrary function of $\dot{B}\left(z, t\right)$ [32].

3.2.2 Many–wire cable

An extension of the two–strand model can be done by considering a Rutherford–type cable of N strands. The strands are connected at all crossing points by uniform cross–contact resistances, but with no line contact between the neighboring strands. Such a cable represents an arrangement where the resistances between any pair of wires are the same. It can be shown that this resistance is a factor $N/2$ smaller than the resistance between the strands in a two–strand model, due to the additional connections via other strands. Since the resistance between the strands in a two–strand cable of length l_0 and twist pitch l_p is

$$\frac{R_c}{n} = \frac{R_c l_p}{2l_0}$$

with $n = 2l_0/l_p$ the number of loops along the cable length, the resistance between a pair of strands in a many–wire cable is

$$\frac{R_c l_p}{N l_0} \ .$$

Let again one half–twist pitch be exposed to a non–zero field sweep rate $\dot{B}$. The steady state supercurrents, at $t \gg \tau$, in individual strands are calculated in a very similar way as in the two–strand model. For reasons of symmetry, currents in opposite strands, i.e. in strand i and $i + N/2$, are equal but of opposite sign. The maximum current $I_{\max}$ appears in the strand pair, which is symmetrically placed in the $\dot{B}$ region. The driving voltage is calculated according to Equation 3.17 and the induced supercurrents by Equation 3.19, but with R being a factor $N/2$ smaller than in the two–strand cable. This gives a maximum supercurrent $I_{\max}$ which is a factor $N/2$ above the value in the two–strand model. This increase becomes plausible with following argument: The current in the opposite strands finds, outside of the $\dot{B}$-region, a smaller effective resistance than in the two–strand model, because of the contacts with all the other strands.

For the strand pair $N/2$ and N, i.e. the first and the last strand inside the half–twist pitch which is exposed to $\dot{B} \neq 0$, the driving voltage is zero because the integral in Equation 3.17 vanishes. Therefore the supercurrent in this strand pair is zero. For other strand pairs, driving voltages are, according to geometry of enclosed areas, between zero and $I_{\max}$.

The time dependence of supercurrents in a many–wire cable is expected to be qualitatively similar to the two–strand model. The steady–state distribution of currents will be reached only after a time $t \gg \tau$. The involved time constants are expected to be larger than in the two–strand model, but a quantitative estimation would require the solution of many coupled diffusion equations [31] and [32].

3.2.3 Accelerator magnets

In an accelerator dipole magnet the field derivative $\dot{B}(z)$ during a charging or a discharging period is constant along the straight section of the magnet. But on a short cable section around the end region of the magnet a sharply varying $\dot{B}(z)$ occurs. The field component perpendicular to the cable is here nearly zero because of the winding of the magnet (see Figure 3.5). Due to the superposition principle this case is identical to $\dot{B}(z) = 0$ on the straight section of the magnet, and $\dot{B}(z) \neq 0$ on a short length of the order of a twist pitch around the end. This will induce the supercurrents inside the Rutherford–type cables from which the magnet is built up.

The currents of opposite direction in opposite strands create, due to the twist pitch of the cable, a magnetic field which alternates at every half–twist pitch. The amplitude of this PFP will show the same space and time dependence as $I(z,t)$. In a magnet the superposition of the contribution of all turns leads to a sinussodial–like field modulation with the period of a twist pitch. The amplitude of field modulation measured at a certain position in a magnet depends on the exact number of twist pitches along a turn, because fields from different turns may add up or cancel each other. This makes it understandable that measured amplitudes can differ greatly from magnet to magnet, even if they are identically

Figure 3.5: The picture shows the coil end of the inner layer of a LHC dipole magnet. The magnetic field in the end section perpendicular to the cable is much lower than in the straight part and can even be zero.

built.

An exact calculation of $I(x,t)$ would require to know not only the time and space dependence of each strand, but also the exact geometry of the twist in the cable. Additionally there also exist currents created in a longer length than in half a winding, for example, currents due to different $\dot{B}$ values in different sections of the winding cross–section. For these reasons it seems that an exact calculation is very complicated, if not unsolvable for a real magnet.

Although the supercurrents can not be completely avoided, the introduced two–wire strand model and its extensions with the corresponding experiments can give some information to a magnet designer [33]:

1. Avoid a sharp variation of $\dot{B}$ within the length of a twist pitch. For accelerator magnets this condition is however difficult to fulfill at the magnet ends.

2. Choose the smallest possible dimension of the cable, because the flux change enclosed in a half twist pitch loop is, in general, proportional to the cable width (if the twist pitch is proportional to the width).

3. Make cross–contact resistances as high as possible, in order to reduce the amplitude and the time constants of the currents.

4. Avoid a large scattering of cross–contact resistances between the strands.

One low–resistance contact may be sufficient to degrade strongly the magnet performance.

Chapter 4

Measurement Environment

As it can be seen from the history of studies on the PFP two different measurement systems have been used. The system of rotating pick up coils having the advantage that the measured magnetic field can be divided directly into the different harmonics. Generally spoken this technique has a very good sensitivity and precision but they are limited in the time and spatial resolution.

The second way to measure the magnetic PFP variations is the use of Hall probes. Because of their small spatial extent it is possible to perform point like measurements, as well as measurements close to the magnet coil. Additionally the Hall probes exhibit a relatively high sensitivity.

For this study two different arrangements of Hall probes were used referring to the two different measurement stations where the magnetic measurements at LHC MTA were performed. The measurement station, referred here to as Block 4, was designed to analyze the field quality of one–meter long LHC dipole model magnets. The second test station deals with full–scale prototypes and pre–series LHC dipole magnets and is referred to here as the Superconducting Magnets Test Plant (SMTP). The Hall probes used for the measurement of the short and long dipole magnets have different properties and also the data acquisition differs from each other.

4.1 The Hall effect

In 1856 W. Thomson discovered the increased resistance of an electric conductor in a magnetic field. It was E. H. Hall, who explained this effect several years later in 1879, measuring at the same time a voltage across a current–carrying conductor [37].

The latter phenomenon, known today as the Hall effect, is due to the Lorentz force of a magnetic field on moving charged particles, acting perpendicular to the directions both of the field and of the moving particles [38]. This can be

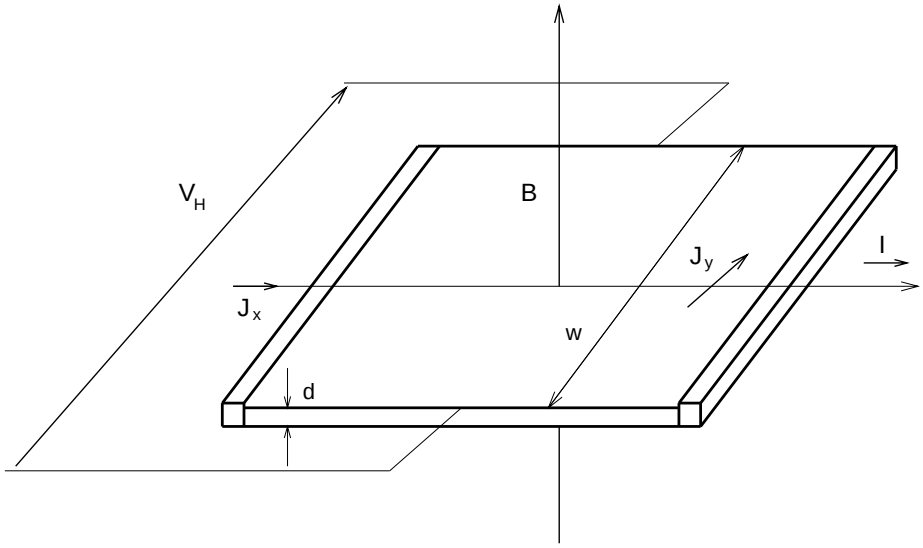

Figure 4.1: Principle of a Hall probe, where the Hall voltage V_H is created by the current density J_y in the probe, perpendicular to the current density J_x of the longitudinal control current I.

described in terms of the semiclassical equation

$$m^* \frac{d\vec{v}}{dt} + m^* \frac{\vec{v}}{\tau} = e\vec{E} + \vec{v} \times \vec{B} \tag{4.1}$$

where the first term represents the rate of change of momentum (m^* is the "effective" mass of the particle), the second term is a damping force proportional to velocity of the charge carriers and the relaxation time, and τ is the mean time between collisions with the lattice or with imperfections which disturb the lattice periodicity. Therefore the motion of the particles in metals and semiconductors will not be a cycloidal one like in vacuum. At each collision with the atoms of the crystal lattice the particles lose some of their velocity, afterwards being accelerated again in the electric field. So they will move between two collisions only along a short part of a cycloidal curve [39].

In Equation 4.1 it is presumed that all the charge carriers are in an isothermal environment and they have the same kinetic energy imparted by the electric field and by the Lorentz force.

If we consider the case shown in Figure 4.1 where the magnet induction has only the single component $B = B_z$, then we can write for the Cartesian components of Equation 4.1

$$\begin{aligned} m^* \frac{dv_x}{dt} + m^* \frac{v_x}{\tau} &= e\left(E_x + v_y B\right) \\ m^* \frac{dv_y}{dt} + m^* \frac{v_y}{\tau} &= e\left(E_y - v_x B\right) \\ m^* \frac{dv_z}{dt} &= eE_z = 0 \ . \end{aligned} \tag{4.2}$$

Using the definition of the angular cyclotron frequency, $\omega_c = \frac{eB}{m^*}$, and the relation for the conductivity, $\sigma = \frac{ne^2}{m^*}\tau$, Equation 4.2 can be rewritten to

$$\begin{aligned} \tau \frac{dJ_x}{dt} + J_x &= \sigma E_x + \omega_c \tau J_y \\ \tau \frac{dJ_y}{dt} + J_y &= \sigma E_y + \omega_c \tau J_x \end{aligned} \tag{4.3}$$

where $\vec{J} = ne\vec{v}$ is the current density vector.

If the applied electric field and the current density are time varying quantities with the angular frequency ω, such that $\vec{J} = \vec{J}_0 e^{i\omega t}$, then provided that $\nabla \vec{E} = 0$ and $\nabla \times \vec{E} = 0$, Equation 4.3 becomes to

$$\begin{aligned} J_x \left(1 + i\omega\tau\right) - \omega_c \tau J_y &= \sigma E_x \\ J_y \left(1 + i\omega\tau\right) + \omega_c \tau J_x &= \sigma E_y \ . \end{aligned} \tag{4.4}$$

Rearranging by solving explicitly for J_x and J_y leads to

$$\begin{aligned} J_x &= \frac{\sigma}{\left(1 + i\omega\tau\right)^2 + \left(\omega_c\tau\right)^2} \left[\left(1 + i\omega\tau\right) E_x + \omega_c \tau E_y\right] \\ J_y &= \frac{\sigma}{\left(1 + i\omega\tau\right)^2 + \left(\omega_c\tau\right)^2} \left[-\omega_c \tau E_x + \left(1 + i\omega\tau\right) E_y\right] \end{aligned} \tag{4.5}$$

or

$$\begin{aligned} \vec{J} &= \hat{\sigma} \cdot \vec{E} \qquad \text{with} \qquad \hat{\sigma} = \begin{pmatrix} \sigma_{xx} & \sigma_{xy} \\ \sigma_{xy} & \sigma_{xx} \end{pmatrix} = \\ &= \frac{\sigma}{\left(1 + i\omega\tau\right)^2 + \left(\omega_c\tau\right)^2} \begin{pmatrix} 1 + \omega\tau & \omega_c\tau \\ \omega_c\tau & 1 + \omega\tau \end{pmatrix} \ . \end{aligned} \tag{4.6}$$

Only for the case $\omega\tau \ll 1$ (low frequencies[1]) the tensor components become

[1]For semiconducting compounds τ is of the order 10^{-12} to 10^{-13}s. Therefore σ is essentially the same for d.c. and for frequencies less than ~ 10 Ghz.

to

$$\begin{aligned} \sigma_{xx} &= \frac{\sigma}{1+(\omega_c\tau)^2} \\ \sigma_{xy} &= \frac{\sigma\omega_c\tau}{1+(\omega_c\tau)^2} \end{aligned}$$

and Equation 4.5 can be written in simply way as

$$\begin{aligned} J_x &= \frac{\sigma}{1+(\omega_c\tau)^2}\left(E_x+\omega_c\tau E_y\right) \\ J_y &= \frac{\sigma}{1+(\omega_c\tau)^2}\left(-\omega_c\tau E_x+E_y\right) \ . \end{aligned} \tag{4.7}$$

Introducing the Hall mobility $\mu_H = \frac{e\tau}{m^*}$ and therefore $\omega_c\tau = \mu_H B$, the current density vector can be represented in dependence of the electric and the magnetic field.

$$\begin{aligned} J_x &= \frac{\sigma\cdot(E_x+\mu_H B E_y)}{1+\mu_H^2 B^2} \\ J_y &= \frac{\sigma\cdot(E_y-\mu_H B E_x)}{1+\mu_H^2 B^2} \end{aligned} \tag{4.8}$$

For a homogeneous, isotropic, rectangular Hall probe (Figure 4.1) with the Hall output terminals not connected to a load and no current density in y-dircetion, $J_y = 0$, the x-component of the current density can be calculated

$$J_y = 0 \quad \Rightarrow \quad E_x = \frac{E_y}{\mu_H B} \tag{4.9}$$

$$J_x = \frac{\sigma}{1+\mu_H^2 B^2}\left(\frac{E_y}{\mu_H B}+\mu_H B E_y\right) = \frac{\sigma}{\mu_H}\frac{E_y}{B} \tag{4.10}$$

and solved for E_y leading to

$$E_y = \frac{\mu_H}{\sigma} J_x B = R_H J_x B \ . \tag{4.11}$$

The Hall coefficient $R_H = \frac{\mu_H}{\sigma}$ is negative for electrons and it is positive for holes. It may be considered to be a constant of proportionality between the product $J_x B$ and resultant Hall field E_y. If the input control current I flowing through the Hall plate is expressed as $I = wdJ_x$ and E_y is integrated over the width of the plate, then the Hall voltage V_H is

$$V_H = -\int_0^w E_y dy = -\frac{R_H}{d} B I \ . \tag{4.12}$$

For a strong Hall effect the probe must be thin and must exhibit high charge mobility at low electric conductivity σ, such as in the semiconducting compounds GaAs, InAs or InSb.

In addition to temperature dependent and the non–linear calibration curves limiting the accuracy of Hall probe measurements, the so–called planar Hall effect and the de Hass–Šubnikov effect, appearing at cryogenic temperatures, are important. The planar effect limits the measuring accuracy of low perpendicular fields $\vec{B}$ in the presence of a strong planar field, parallel to the plane of the Hall probe. For low temperature measurements at high fields increased field–dependent oscillations appear. This is the de Hass–Šubnikov effect. Because of this effect the oscillations must be investigated and considered for cryogenic measurements with superconducting magnets. Another way to solve this problem is to place a room temperature anticryostat in the cold bore and perform Hall probe measurements at ambient temperature [40].

4.2 Test facility for short magnet models

4.2.1 General layout

The cryogenic test facility called Block 4 is located at the Prevessin site of the CERN area in France. It was designed to study LHC short magnet models and protection diodes. Two vertical setups can be used to suspend and immerse magnets in superfluid helium, as shown in Figure 4.2.

A so–called λ-plate separates the pool boiling helium bath from the superfluid bath, both at atmospheric pressure (Claudet bath). The subcooled superfluid state in the lower portion of the cryostat is achieved by means of heat exchanger, where saturated superfluid helium conditions are obtained via Joule–Thomson expansion of liquid helium from $1\,bar$ down to approximately $15\,mbar$. The λ-plate has a number of leak–tight feedthroughs for superconducting busbars, instrumentation wires and a sliding bearing for the rotating shaft used for measurements of the field quality [41]. A special shaft was equipped with stainless steel boxes containing Hall plates as described in 4.2.3. This test environment provides a temperature stability to a level of $\pm 0.03\,K$.

The short dipole model test program for the LHC allows convenient studies of different design and assembly options on one–meter long LHC dipole magnets. The test program covers single (labeled MBSMS[2]) and twin (labeled MBSMT[2]) aperture magnets. All model magnets were designed, fabricated and tested in–house. Often already tested magnets were re–worked and re–assembled with modified parameters, which created a number of different versions for some magnets. Each model magnet was tested in respect to training behavior quench

[2]MBSM stands for Main Bending Short Model, and the last letter S or T represents a single and a twin aperture magnet respectively.

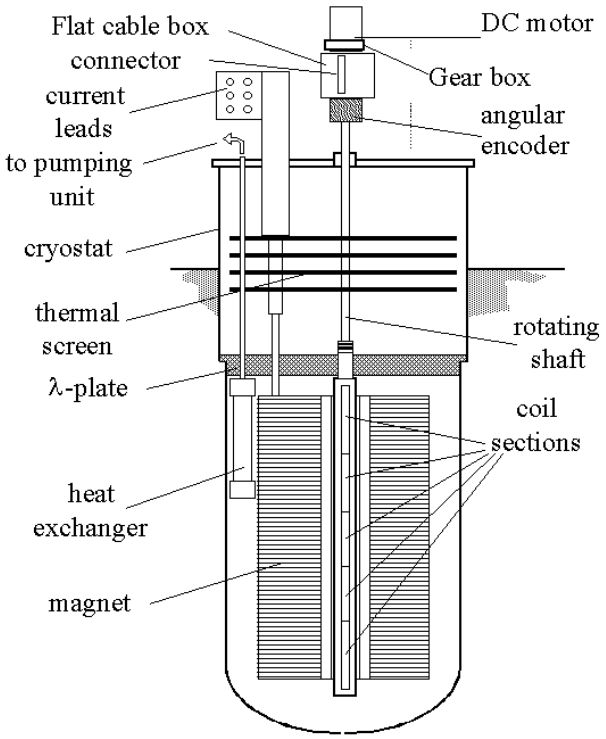

Figure 4.2: Schematic view of the vertical set–up for the dipole model magnets, shown for a single aperture model [42].

localization, loss measurements and series of magnetic measurements [43].

Since the program of the 2nd generation dipoles was started in 1995 with the single aperture magnets a total amount of 39 single aperture models were tested at cold at a rate of about one per month. The results allowed to select the series–design features among several variants for the coil cross section, the material of the collars and of the coil spacers, the coil pre–stress and the cable insulation. Since August 1999 the model program is focussed on the fabrication of twin aperture models to study the training performance. In addition the recent twin aperture magnets are dedicated to the fine–tuning of the baseline design and the manufacture of the coil ends. Finally, the short dipole model program will come to an end in the year 2001 with the fabrication of three identical magnets for studying the reproducibility of training performance and of magnetic field quality [44].

4.2.2 Hall probe properties and calibration

The cryogenic Hall probes of three different types provided by the AREPOC company were used. Their main characteristics are given in Table 4.1. According

to the AREPOC designation Hall sensors are classified in two categories. The first letter H of the names listed in the Table 4.1 means high sensitivity whereas the letter L denotes low sensitivity.

The behavior of each Hall probe type at $1.9\,K$ was investigated [46]. In particular the so–called de Hass–Van–Alphen oscillations were characterized. Under the influence of strong magnetic field, the electron motion is quantized and the accompanying change in the electronic energy levels produces oscillation in the magneto–electrical transport properties of metals as well as of semiconductors [47]. The oscillation of the magnetoresistance is known as the de Hass–Šubnikov effect and this name has been commonly extended to the case of the Hall voltage oscillation. Such type of oscillations have a well defined period which varies at the inverse of the magnetic field. When a precision better than $\pm 0.5\%$ is needed, such oscillations should be taken into account in the calibration procedure to correct the linear field variation of the Hall voltages.

The calibration of the sensitivity of the Hall probes provided by AREPOC was performed at $T = 300\,K$ and at nominal control current I_n for the different probes used. A new calibration at cold environment ($T = 1.8\,K$) was performed with the help of the single aperture dipole model magnet MBSMS17.V3 in the test faciltiy at Block 4. The probes were inserted in the central part of the aperture with the magnetic field perpendicular to sensing areas. For the calibration a control current of $I_n = \pm 5\,mA$ was used provided by a KNICK DC–Strom–Calibrator J152 which delivers stable current with an error below $\pm 40\,ppm$. The transformation of the transport current into the applied magnetic field of the magnet was achieved by the so–called transfer function deduced form rotating coil measurements with a precision of the order of $\pm 10^{-4}$ for current values higher than few kA [48]. The stability of the magnet power supply is included in the range of $\pm 10\,ppm$.

The magnet was ramped in steps of $500\,A$ from 0 to $12500\,A$. At each current step the transport current of the magnet and the field seen by the Hall probes were recorded, for both signs of the control current, $\pm 5\,mA$. This results in a Hall sensor output voltage of V_{H+} and V_{H-} if the $+$ and $-$ sign in the subscript refer to the polarity of the Hall control current. Such a sequence makes it possible to substract in great part the thermal emf's contribution to the Hall voltages measured by taking the half difference $\langle V_H \rangle = \frac{1}{2}(V_{H+} - V_{H-})$.

Hall probes	Nominal control current, I_n $[mA]$	Sensitivity $[V/TA]$	Sensitive area $[mm^2]$	Number of units
HHP–NP	50	2.308	1.25×0.5	1
LHP–MP	20	0.275 - 0.44	0.1×0.1	3
HHP–MU	20	4.66 - 5.11	0.1×0.1	9

Table 4.1: Main parameters at $T = 300\,K$ of the Hall probes used [45]

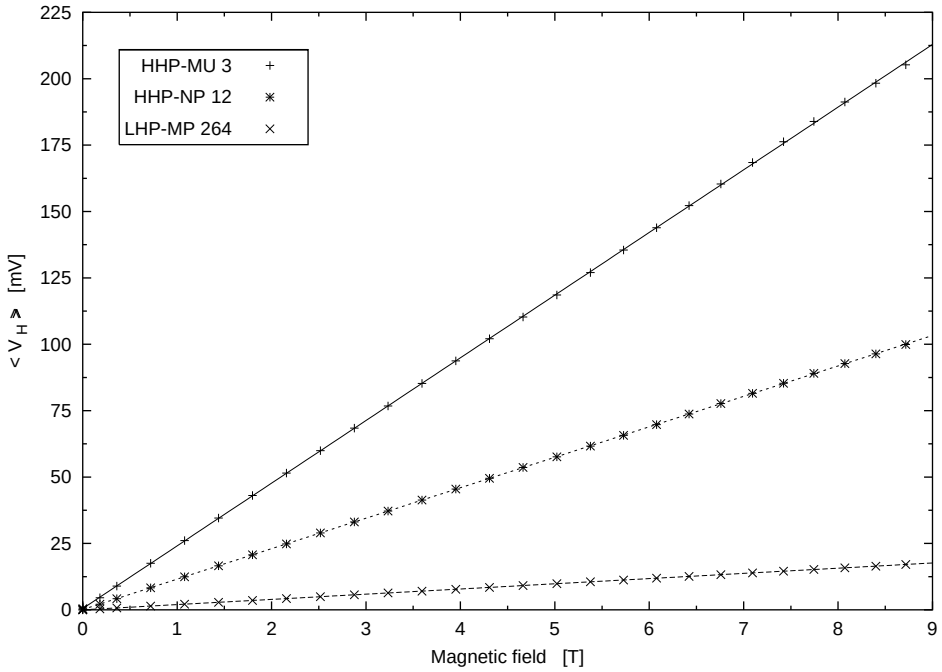

Figure 4.3: Example for the calibration applied on all used Hall probes of the three different types HHP–NP, LHP–MP and HHP–MP.

At the end data doublets for every Hall probe, which can be fitted with a linear function were obtained. The slope of the linear function correspond to the calibration factor at $5\,mA$ which transfers the measured Hall output voltage into magnetic field. An example for this calibration is given in Figure 4.3 where the Hall voltages $\langle V_H \rangle = \frac{1}{2}(V_{H+} - V_{H-})$ versus the applied magnetic field, and the linear fit functions are shown. Three probes, HHP–NP 12, LHP–MP 264 and HHP–MP 3, have been chosen in reference to the three different types of Hall probes discussed in Table 4.1. It can be clearly seen that the sensitivity of the most used HHP–MU type is the highest one, while the sensitivity of the three LHP–MP probes is of about twelve times lower.

Finally the calibration factors for all thirteen Hall probes deduced from the above mentioned procedure are listed in Table 4.2. Slightly lower sensitivities have been obtained around $1.9\,K$ compared to those measured at room temperature.

4.2.3 Hall probe location and measurement system

For the measurements of the PFP inside several short superconducting dipole models the Hall probes were mounted inside two stainless steel cases to protect the probes against the pressure which can be present in the magnet (up to $200\,MPa$). A schematic drawing (Figure 4.4) shows the position of the different probes used

Hall probes	Calibration factor in $[mV/T]$ @ $5\,mA$
HHP–NP 12	11.47
LHP–MP 264	1.96
LHP–MP 274	1.31
LHP–MP 340	2.07
HHP–MU 1	23.61
HHP–MU 2	23.37
HHP–MU 3	23.60
HHP–MU 4	25.00
HHP–MU 5	24.07
HHP–MU 6	24.56
HHP–MU 7	22.67
HHP–MU 9	23.34
HHP–MU 11	23.30

Table 4.2: Calibration factors for the used Hall probes in Block 4 at a control current of $5\,mA$ and a temperature of $1.9\,K$

and their relative distances inside the cases. The distance between the first eight probes amount $2\,cm$ and for the remaining ones it was reduced to $1.5\,cm$.

The probes are glued inside the cases and the corresponding wires come out at the end sides. Finally the probes are covered with a cap fitting to the surface of the cases. A photo (Figure 4.5) of this arrangement shows clearly the stainless steel case with the cap and the Hall probes with their real dimensions.

The two cases were fixed on a special rotating shaft dedicated to such measurements. The probes were located at a radius of $17\,mm$ which correspond to the reference radius of the LHC. The axial position was chosen to cover the central part of the magnet. In total a length of $7 \times 2 + 5 \times 1.5 = 21.5\,cm$ was investigated along the axis. This arrangement allow measurement of the radial component of the total magnetic field as a function of azimuthal angle for the different positions of the z-axis.

Besides the Hall probes the measurement system consists of a power supply, a KNICK DC–Strom–Calibrator J152, to provide the control current I_n for the probes which were connected in series. In the normal operation mode the current was fixed to $I_n = 5\,mA$. Two KEITHLEY 2001 digital multimeters were used with scanner cards (Model 2000-Scan) to measure the voltage of 20 channels. The assignment of channels can be summarized as follows. Thirteen channels were used for Hall voltages, two for the magnet temperature and two for the magnet current. The latter was measured with a Direct Current Current Transformer (DCCT) mounted on a $20\,kA$ power supply. In addition, the drift of the KNICK DC–Strom–Calibrator as well as the offset of both KEITHLEY digital multimeters were measured precisely with the three remaining channels. Dedicated

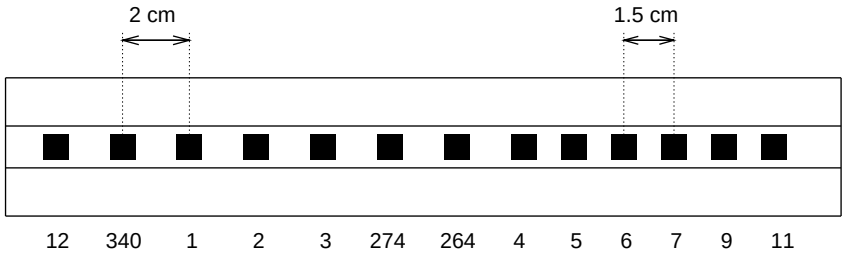

Figure 4.4: The position of the thirteen Hall probes inside the stainlees steel case.

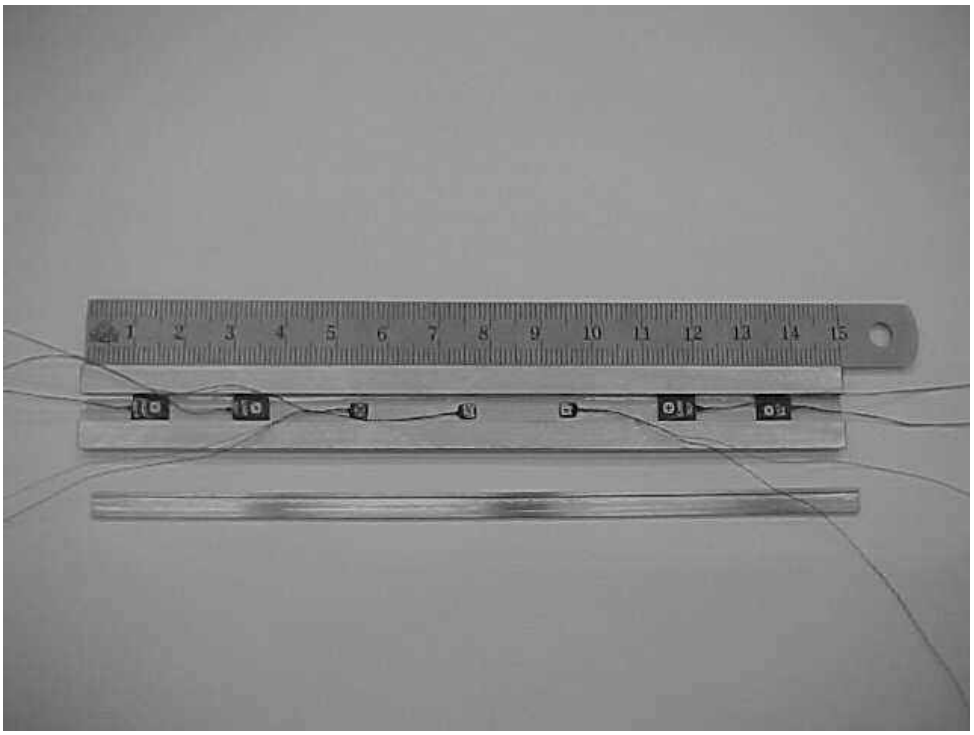

Figure 4.5: Photo of the stainless steel case within the glued Hall probes. The wires are led out to the two ends of the case.

LabVIEW software running on a SUN workstation, was used to interface with the digital multimeters via a GPIB bus for control, data acquisition and storage.

4.2.4 Short magnets measured

Within the short dipole model test program it was possible to perform special tests on several magnets dedicated to the subject of this thesis. The main parameters of these short dipole models, single and twin aperture, are given in Table 4.3. Additional there are some parameters like the cable insulation, coil cross–section, coil end spacers, coil assembly, coil pre–stress, quench heaters and mechanical structure which differ between the different magnet generations and magnet versions respectively. The standard test program, which was applied in parallel to the PFP studies, covered the quench training behavior, the magnetic field and its quality with respect to the LHC accelerator requirements, quench protection and dynamic behavior.

Coil inner diameter	56	mm
Cable width	15.1	mm
Nominal quenching field at $1.9\,K$	9.65	T
Current at $8.4\,T$	11500	A
Ratio of peak field to central field	1.05	
Overall coil length	1080	mm
Length of magnetic steel in the yoke	560	mm
Magnetic length	862	mm
Total inductance	3.2	mH
Total axis forces $8.4\,T$	19	$tons$
Cu/SC ratio of inner / outer strands	1.6/1.9	
I_c of inner cable at $1.9\,K$ and $10\,T$	13750	A
$\frac{dI_c}{dB}$ of inner cable at $1.9\,K$ and $10\,T$	4.8	kA/T
I_c of outer cable at $1.9\,K$ and $9\,T$	12950	A
$\frac{dI_c}{dB}$ of outer cable at $1.9\,K$ and $9\,T$	3.65	kA/T

Table 4.3: Main parameters of the short dipole models

In total three single and three twin aperture short dipole models were available for the Hall probe measurements to study the induced current distribution inside the cables. The first magnet measured was the third version of the single aperture dipole MBSMS17. The two remaining single aperture ones were two later versions of magnet MBSMS23, namely version 3 and version 4.

For the three twin aperture magnets the selection was similar, two versions of MBSMT4 (version 2 and 5) and the third version of magnet MBSMT5. From the chronological point of view the MBSMT5.V3 was finished and measured before the MBSMT4.V5. Table 4.4 summarizes some construction differences between the six used magnets.

Magnet	Prestress after the collaring $[MPa]$		Prestress after the yoking $[MPa]$		Prestress at $1.9\,K$ $[MPa]$		Field resulting prestress loss $[T]$	
	Inner	Outer	Inner	Outer	Inner	Outer	Inner	Outer
S17.V3	49	78	54	83	17	31	7.1	9.5
S23.V3	51	83	60	89	14	32	6.7	9.8
S23.V4	70	85	75	91	28	36	8.3	10.2
T4.V2	50	76	55	82	18	31	7.1	9.5
T5.V3	50	62	52	64	16	24	7.0	8.8
T4.V5	50	74	55	80	17	28	7.0	9.3

Table 4.4: Differences between the measuared short dipole models

4.3 Test facility for full–scale LHC lattice magnets

4.3.1 General layout

The second measurement station is also located on the French CERN site. Besides previously described one–meter model test station Block 4, the Superconducting Magnet Test Plant (SMTP) was designed and constructed to measure the 10 meter long LHC dipole model magnets and the 15 meter long LHC prototype magnets. This test facility will also host the measurement stations for the future pre–series and series measurements.

At the SMTP, cryo–dipoles are connected to the Cold Feed Boxes (CFB) which provide liquid superfluid helium and contains current leads to power the coils. On the test bench, the cryo–dipoles are filled with around $300\,l$ of liquid helium. This constitutes in normal operation the static bath of pressurized superfluid helium through which heat is transported by conduction to a linear cold source made of a heat exchanger tube threaded through the whole cold mass. In this heat exchanger, the heat is absorbed quasi–isothermally by gradual vaporisation of flowing saturated superfluid helium. On the test bench, both apertures of the cryo–dipole are equipped with anticryostats. They allow to insert different types of equipment operating at room temperature like rotating shafts for standard magnetic field measurements or Hall probe set-ups for more local investigations.

The experimental program on the LHC 10 meter long, two–in–one, main dipoles started on the turn of 1998-1999. Since then seven magnets of the 1^{st} generation and five of the 2^{nd} generation have been build in industry and tested at CERN. The design and main test results of these magnets were described in [49] and [50].

In summer 1998, CERN launched in industry the fabrication of six full–scale dipole prototype collared coils of the 3^{rd} generation i.e. final design. These collared coils were subsequently assembled into cryo–dipoles at the CERN Magnet

Assembly Facility (MAF).

In November 1999, CERN placed, with three European firms, a first order for three times thirty pre–series dipole cold masses.

The magnets are tested with respect to quench training, conductor performance, magnet protection, sensitivity to ramp rate and field quality in terms of the design parameters and the aims of the full–scale LHC dipole program [51].

4.3.2 Hall probe properties and calibration

Six Hall probes were used which have been again developed by AREPOC for operation at room as well as at cryogenic temperatures. They are all of the same type labeled HHP–NU which means that they are prepared in the special doped semiconductor featuring high sensitivity, at least $70\,mV$ per Tesla at the standard active area size. The dimensions of the active area are $1.25\,mm \times 0.5\,mm$ and the nominal control current I_n is $50\,mA$ at a temperature of $300\,K$. The linearity error up to $1\,T$ is less than 0.2 percent.

The slight different values for the sensitivity, the error of the linearity from 0 up to $1\,T$ and the offset values provided by AREPOC are given in Table 4.5 for the six used Hall probes.

In contrary to the measurements in Block 4 which were performed at cryogenic temperatures the Hall probes used at the SMTP are placed at room temperature inside an anticyrostat in one aperture of the magnet. Nevertheless the sensitivity and the linearity of the probes was checked in a range of 0 to $1\,T$ before they have been used for the magnetic measurements. For this purpose each probe was placed perpendicular to the main dipole field of a conventional reference magnet with the help of an inclinometer. The magnet was ramped in steps of $50\,mT$ and around the injection field from 0.5 to $0.6\,T$ the increment was reduced to $0.1\,mT$. The magnetic field was measured with two NMR–sensors, one for the low field range less than $0.2\,T$ and the other one for the rest of the applied field range.

Hall probes	Sensitivity $[mV/T]$	Error [%]	Offset $[\mu V]$
HHP–NU 1	222	< 0.2	24
HHP–NU 3	223.4	< 0.2	56
HHP–NU 10	222.3	< 0.2	120
HHP–NU 2	227.9	< 0.2	104
HHP–NU 9	228.1	< 0.2	-26
HHP–NU 8	225	< 0.2	135

Table 4.5: Specification of the six used Hall probes at room temperature ($T = 300\,K$) and at the nominal current $I_n = 50\,mA$ for this temperature. Data provided by AREPOC

Hall probes	Sensitivity $[mV/T]$	Error 0 - 0.3 T [%]	Error $> 0.3\,T$ [%]	Offset $[\mu V]$
HHP–NU 1	221.133	< 1.020	< 0.066	652.433
HHP–NU 3	223.752	< 1.465	< 0.111	578.188
HHP–NU 10	223.875	< 1.228	< 0.114	709.662
HHP–NU 2	228.433	< 1.571	< 0.159	760.863
HHP–NU 9	228.037	< 1.842	< 0.197	827.137
HHP–NU 8	225.915	< 0.830	< 0.144	201.797

Table 4.6: Measured values of the main parameters of the six used Hall probes at room temperature ($T = 300\,K$) and at the nominal current of $50\,mA$

The precision of these NMR–sondes is in the μT range. The control current of the Hall probes was fixed and equal to the nominal control current of $50\,mA$. A KNICK DC–Strom–Calibrator J152 was used as previously for the measurements in Block 4. The Hall voltage output was measured again with a KEITHLEY 2001 digital multimeter.

Finally the recorded Hall voltage in function of the applied magnetic field was fitted with a linear function. The values for the slope, i.e. the sensitivity of the probe at a fixed control current, and the offset values are summarized in Table 4.6, as well as the linearity error. Because this error increases for lower field values ($< 0.3\,T$) it is given for the two field ranges from 0 to $0.3\,T$ and from 0.3 up to $1\,T$ separately.

As an example Figure 4.6 shows the measured Hall voltage versus the magnetic field with the applied linear function for the Hall probe labeled HHP–NU 9 which pointed out the largest linearity error of all probes. This error in function of the magnetic field is shown in Figure 4.7 for the same probe. It can be clearly seen that the deviation from the linear fit is much larger at small field values.

The results of the Hall probe tests described above are in quite good agreement with the values given by the AREPOC data sheets for the six probes. Therefor the calibration values provided directly from AREPOC were used for the further data treatment without correction of the small non–linearity.

4.3.3 Hall probe location and measurement system

For the measurements inside long LHC cryo–dipoles a device consisting of six Hall probes was used (see Figure 4.8). It was designed to measure not only the total magnetic field of the dipole magnet but also to extract directly the sextupole component. For this purpose three Hall probes are mounted onto the surface of a ring with an angular spacing of 120 degree. Each probe measures the projection of the field onto a vector perpendicular to its surface. In an ideal case this arrangement compensates the main dipole field and produces a signal

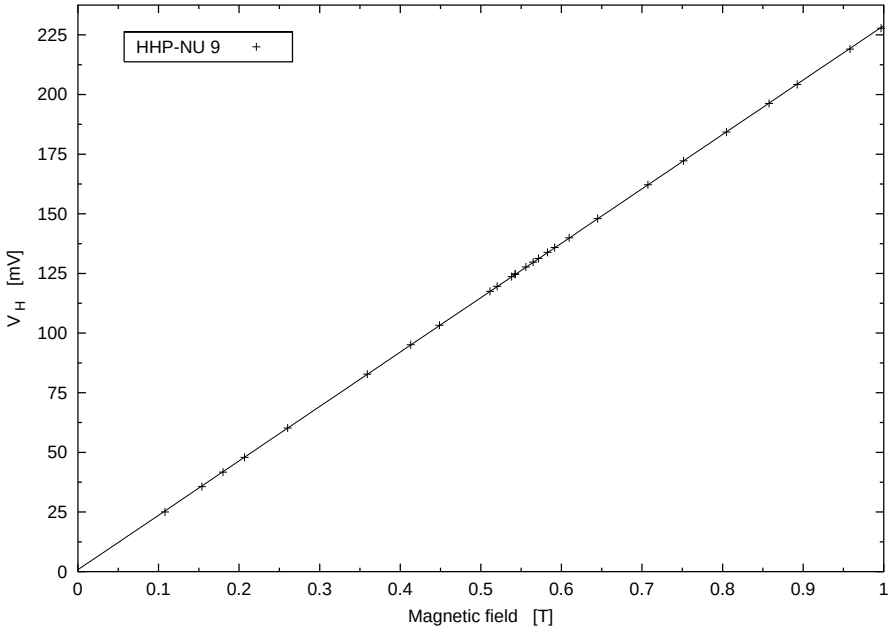

Figure 4.6: The linearity and the sensitivity of the used Hall probes. Example of HHP–NU 9.

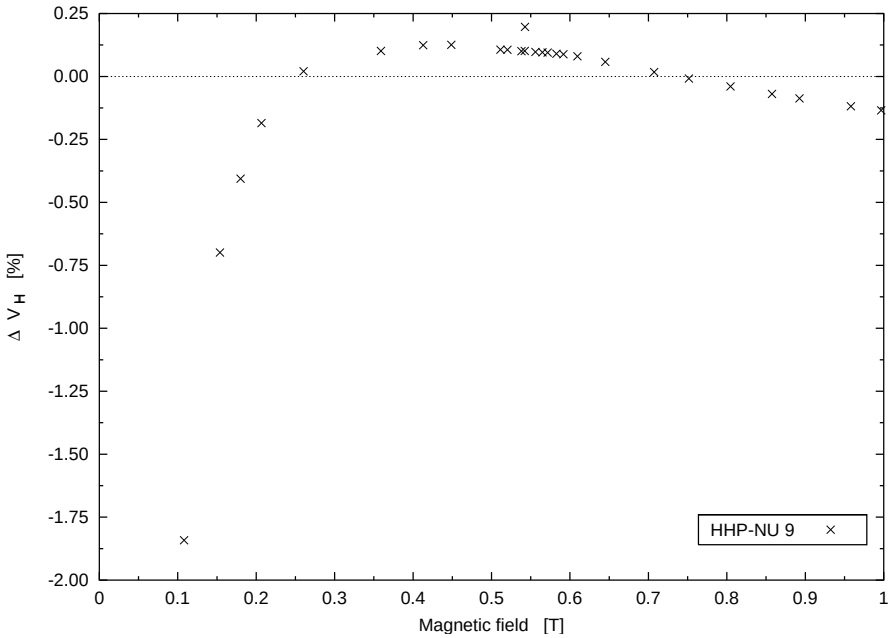

Figure 4.7: Deviation from the linear fit function for HHP–NU 9. For field values larger than $0.3\,T$ the linearity error is smaller than 0.2%.

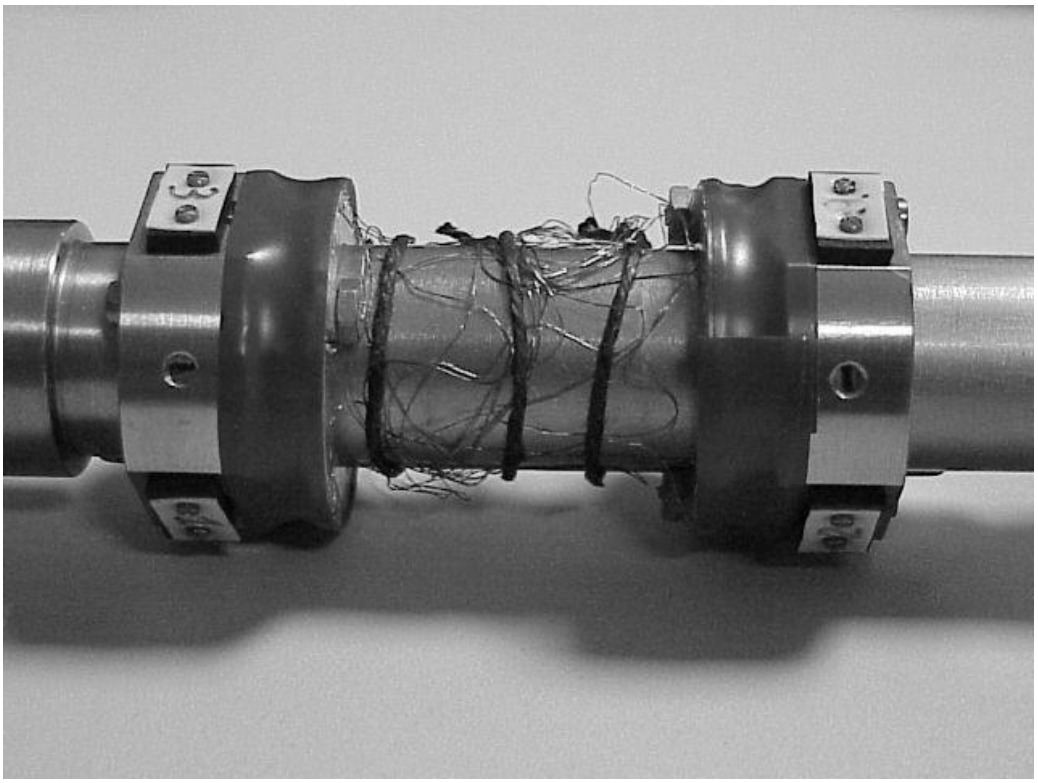

Figure 4.8: Photo of the Hall pobes set–up used in the SMTP.

proportional to the sextupole one. Two of such sextupole rings are assembled on a Ti-alloy support shaft at a distance of $5.5\,cm$. The shaft is equipped with rollers and ball bearings in order to move and rotate the device inside the warm bore of the magnet i.e. inside an anticryostat [52].

The Hall probes in the detector are connected in series with the current source. This ensures that the used control current of $I_n = 50\,mA$ is the same for all probes. A fifteen meter long cable connects the sensor in the magnet to the data acquisition system. The voltage signal of each Hall probe is measured with a KEITHLEY 2001 digital multimeter. A LabVIEW based software running on a SUN workstation provides the control of the multimeters and the data storage.

Figure 4.9 shows the cross–section of a LHC dipole magnet coil within the above described Hall probe detector. The device is orientated inside the anticryostat that the sensitive area of one of the probes of each ring lies perpendicular to the dipole field. The detector allows to measure simultaneously the field on two different positions along the magnet axis. For covering a longer part of the axis it is necessary to move the detector in longitudinal direction without rotation of the shaft.

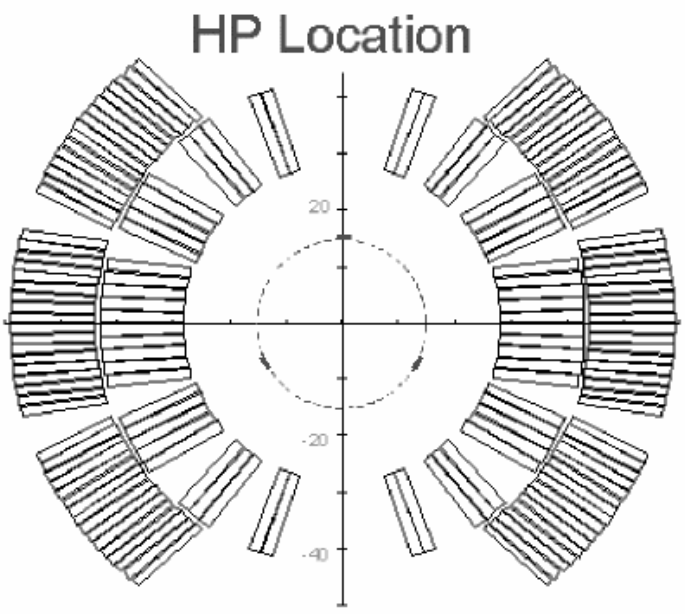

Figure 4.9: The cross–section of a coil of the LHC dipoles. The coil consits of two layers (inner and outer) and six blocks in each quarter. The Hall probes are glued on a ring with an angular spacing of 120 degree. One of the three probes lies perpendicular to the main field.

4.3.4 Long magnets measured

The design of the 3rd and final generation of the LHC full–scale superconducting dipole prototypes has been described in details in [53] and [54]. The construction of these magnets is the result of close collaboration between CERN and European industry. Only the main design features and fabrication variants will be recalled here in view of the measured magnets concerning this study.

The 3rd generation LHC–dipole coils were wound with two different, 15.1 mm wide, graded NbTi Rutherford cables. The cable for the inner layer consists of 28 strands of 1.065 mm diameter, while that for the outer layer consists of 36 strands of 0.825 mm diameter. As compared to the 5-block coil of the 2nd generation, in the 3rd generation dipole coil the conductors of each quadrant are distributed in six blocks. The cable insulation is all polyimide and composed typically of two layers of 25 μm thick tapes each overlapped by 50%, and a third 70 μm thick adhesive coated layer, spaced by 2 mm to provide channels for helium penetration into the coils.

All two–in–one LHC dipole magnets have a single race track type collar, embracing the coils of the two dipole channels. Before the collaring process the thickness of the correcting shims is calculated on the basis of the required pre–stress and the actual size of the coils. The target value for the residual pre–stress

when cold is $25\,MPa$ to $35\,MPa$, on both the inner and the outer layer. The main manufacturing variants of the measured magnets, specific for each company or introduced for evaluation in view of the series production are listed in Table 4.7. The magnet names are referred to the Main Bending Prototypes (MBP) and the Main Bending Pre–Series (MBPS) respectively.

The detailed results of the performed tests and measurements of magnets are collected in several CERN Internal Notes [55]-[58].

Magnet name	Coil pre–stress at $293\,K$	Collar material	Collaring procedures	Colar packs
MBP 2O1	62/62[a]	aus. steel	No Mandrel	1 pair
MBP 2A2	56/60[a]	aus. steel	Rigid Mandrel	32 pairs
MBP 2O2	54/63[a]	aus. steel	No Mandrel	1 pair
MBPS O01	90/90[a,b]	aus. steel	Both collared on	1 pair
MBPS A01	80/80[a,b]	aus. steel	the cold bores	32 pairs

[a] values in MPa for Inner/Outer layer. The pre–stress at 1.9 K can be evaluated in MPa from the pre–stress (σ_{293}) at 293 K as 0.5(σ_{293}-15)

[b] estimated average values

Table 4.7: Main design and assembly variants of full–scale LHC dipoles

Chapter 5

Experimental Results

5.1 General magnetic field inside a dipole

A perfect dipole field is produced by a current density that varies as a function of the azimuthal angle ϕ. This current distribution can be described as

$$I(\phi) = I_0 \cos(\phi) \tag{5.1}$$

and is shown in Figure 5.1 as a geometry of two intersecting circles or ellipses with their centres spaced apart and with opposite current direction.

In practical high–field accelerator magnets a current distribution of Equation 5.1 is difficult to fabricate with a superconducting cable of constant cross–section. Thus the so–called shell–type configuration is applied to approximate the ideal current distribution. Figure 5.2 shows the cross–section of one quadrant of one aperture of a typical 6-blocks geometry LHC dipole magnet. The blocks are separated by copper wedges.

Due to this approximation of the ideal dipole current distribution other multipole components are present which are referred to as distortions or field errors. These field imperfections, which in order to characterize a certain field quality, must be minimized and corrected for by using higher–order coils.

The main multipole is often referred to as the main component or fundamental, while the other multipoles are called harmonics. The harmonics can be normalized to the main component. For a dipole magnet the field at position $z = x + iy$ is usually expressed by a two–dimensional Fourier series

$$\vec{B}(x,y) = B_y + iB_x = B_1 \sum_{n=1}^{\infty} (b_n + ia_n) \left(\frac{x+iy}{R_{ref}} \right)^{n-1} \tag{5.2}$$

where b_n and a_n are the normal and skew multipole coefficients, normalized to the main component B_1. R_{ref} represents the reference radius which is set to $17\,mm$. The relative multipole components b_n and a_n are typically about 10^{-4} therefore they are often expressed in so–called units of 10^{-4}.

Figure 5.1: Generation of a pure dipole field by a $\cos(\phi)$ current distribution and positive ($\otimes$) and negative ($\odot$) current densities respectively. The right side shows a conventional dipole magnet with iron pole shoes [59].

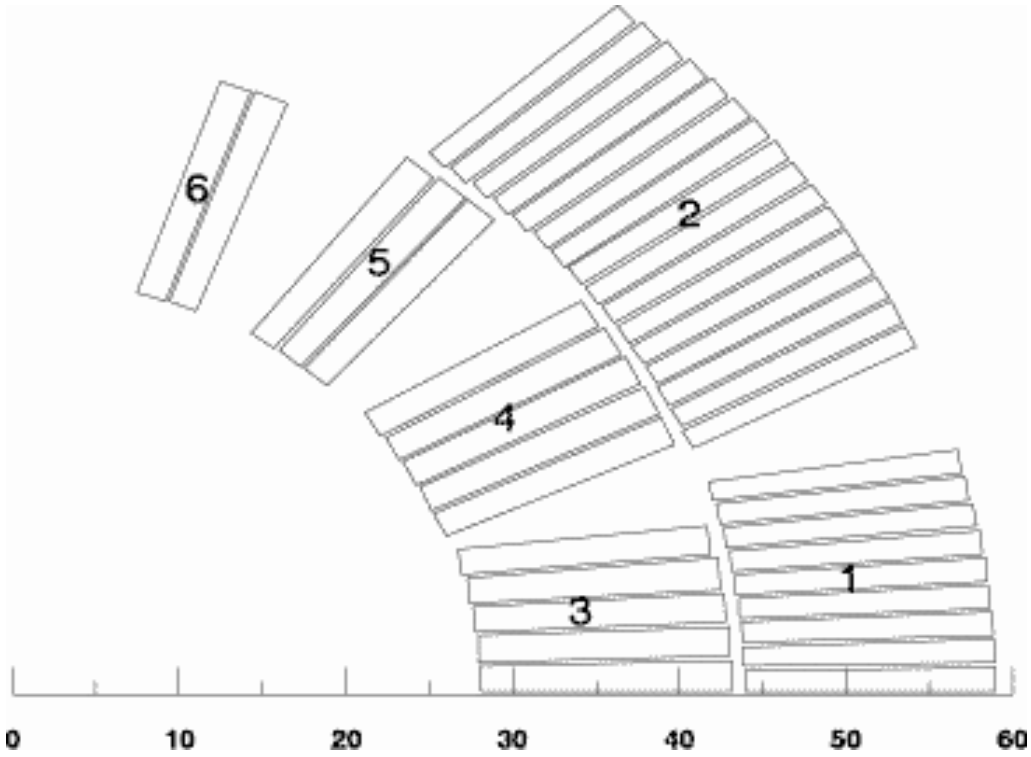

Figure 5.2: View of the cross–section of the two–shell arrangement for a LHC dipole coil. The two blocks in the outer coil and the remaining four blocks in the inner coil are separated by copper wedges.

In practical dipole magnets all normal odd harmonics are present since the current distribution is slightly different from the ideal $\cos(\phi)$ shape. Due to fabrication tolerances normal–even and skew harmonics are also present. These field errors can be defined of geometric origin as already known from normal conducting magnets. In twin–aperture magnets with a common mechanical structure additional field errors are introduced due to (non–symmetrical) saturation effects of the iron yoke. The geometric and the saturation field contributions are reproducible, can be predicted and may be largely inferred from warm measurements.

It has been observed that besides the normal transport current additional eddy currents occur inside the superconducting cables. These eddy currents can be divided into a non–uniform and a uniform current distribution. The non–uniform part of the eddy currents has its origin mainly in the statistical distribution of the cross–contact resistance and in the local variation of the field sweep rate $\dot{B}$ (mainly in the ends of the magnet). An assumed constant field increase along the cable length is responsible for the uniform current distribution. Both effects have been experimentally investigated and results will be presented and analyzed in the following.

5.2 Measurements and analysis of the PFP

5.2.1 Measurements protocol

In general every magnet was quenched before starting a new measurement in order to erase the "memory" of all previous induced currents. Afterwards the system was cooled down again to a temperature of about $1.9\,K$ below the λ-point of helium ($T_\lambda = 2.163\,K$) remaining stable for the whole measurement.

The superconducting magnets were submitted to current cycles of the type shown in Figure 5.3 which can be described with four parameters. If the origin of time is set to be equal to the start of the current increase, the charging period of the magnet up to the maximum current $I_{\max}$ will be defined by t_1. In the case of a constant current on the flat–top the difference

$$\Delta t_{ft} = t_2 - t_1 \tag{5.3}$$

represents the plateau duration during the cycle. The third point of time t_3 indicates the end of the discharging period i.e. $t_3 - t_2$, as well as the end of the whole current cycle.

An equivalent description of a cycle shown in Figure 5.3 is given by using also the maximum current $I_{\max}$ and the flat–top duration Δt_{ft} but takes the two ramp rates for up and down into account which are linked to the previously mentioned

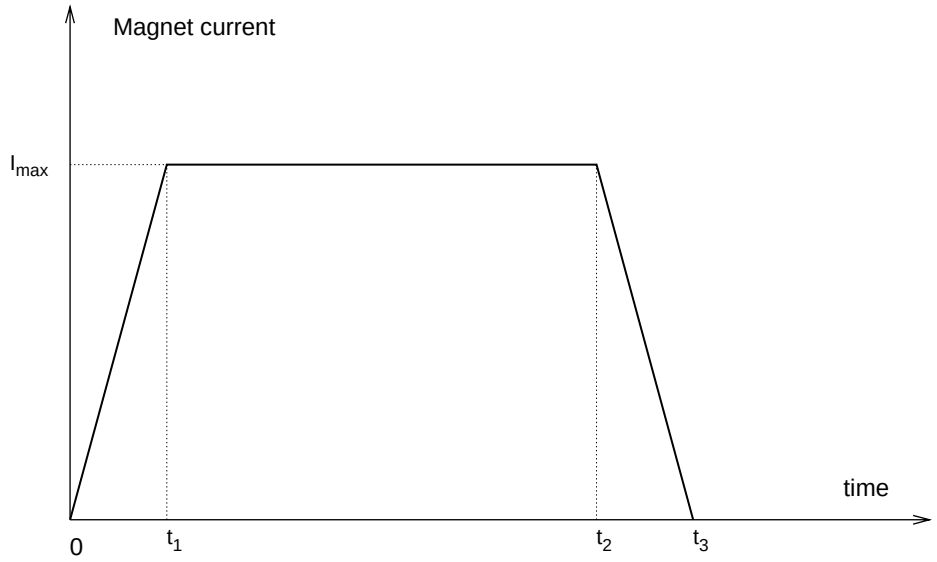

Figure 5.3: Schematic view of a current cycle applied during the PFP measurements.

formulation by

$$\begin{aligned} \dot{I}_{up} &= \frac{I_{\max}}{t_1} \\ \dot{I}_{dn} &= \frac{I_{\max}}{t_3 - t_2} \ . \end{aligned} \tag{5.4}$$

The data obtained from the measurement systems described in Chapter 4 are usually recorded in an ASCII file on a SUN workstation. The files are transferred on a network disk where all R & D data of each magnet are stored. The further data treatment has been performed locally on PC, mainly using Gnuplot [60] and MS-Excel. The two different Hall probe systems used in Block 4 and in the SMTP provide different raw data files and a slightly modified data analysis for the long prototype and pre–series magnets was developed.

Short magnets

In the case of the short dipole models the raw data for every current cycle of the PFP measurements are stored in one single file and the data can be divided into three parts: the current cycle, the decay period after the cycle without any transport current inside the magnet and finally a rotation of the shaft with the Hall probes. Especially a rotation of 180 degrees has been performed which is

used to calculate the offset of the Hall probes. This offset (i.e. the mean value from the non–rotated Hall voltages and the rotated ones) is subtracted from the original data. Afterwards the Hall voltages are transformed into field values using the calibration factors from Table 4.2.

In this way the magnetic field inside the magnet aperture was measured with the Hall probes as a function of time during the flat–top Δt_{ft}, and at the end of the current cycle for $t > t_3$.

Long magnets

By using the Hall probes with the sextupole set–up dedicated for the snap–back study in the LHC dipoles [52] it is only possible to measure the magnetic field simultaneously on two positions along the magnet axis.

The previous measurements with the short dipole models have shown (see also section 5.2.2) that after a strong decay of typically ten minutes the PFP decays much slower with time constants of several hours. Thus the position of the Hall probes stayed unchanged after t_3 for fifteen minutes in order to reach the phase of the PFP with a much longer time constant. After this fast decay period the field inside the aperture was scanned by moving the Hall probes set–up at fixed orientation in steps of $2\,cm$. For every position a mean value of the recorded voltage values ($2\,mn \triangleq 200$ data points for each step) was calculated which contributes to the shape of the PFP in dependence on the axial position.

Due to this measurement arrangement only the static point of view was investigated for the long prototype and pre–series magnets.

5.2.2 Influence of the precycle on the PFP

The PFP was clearly observed at the end of the current cycles for all magnets which were investigated when the flat–top duration Δt_{ft} was larger than $3000\,s$. It was in general difficult to identify it on the current flat–top mainly because of the contribution of other sources of field inhomogeneity like the ferromagnetic yoke laminations.

The study dealing with the influence of the current cycle parameters on the PFP was mainly performed on the short dipole models because of the time constraint of the test duration for the full–scale prototypes and pre–series LHC dipoles.

Two examples of PFPs measured on the short model MBSMS17.V3 at times t_1 and t_3 are given in Figure 5.4. They correspond to a current cycle with a ramp–up to $9\,kA$ at $40\,A/s$ followed by a ramp–down at $-40\,A/s$ after a flat–top time of $\Delta t_{ft} = 3000\,s$. Typical PFPs can be well approximated by the relation

$$B\left(z,t\right) = B_0\left(t\right) + B_1\left(t\right) \cdot \sin\left(\frac{2\pi z}{\lambda} + \varphi\right) \tag{5.5}$$

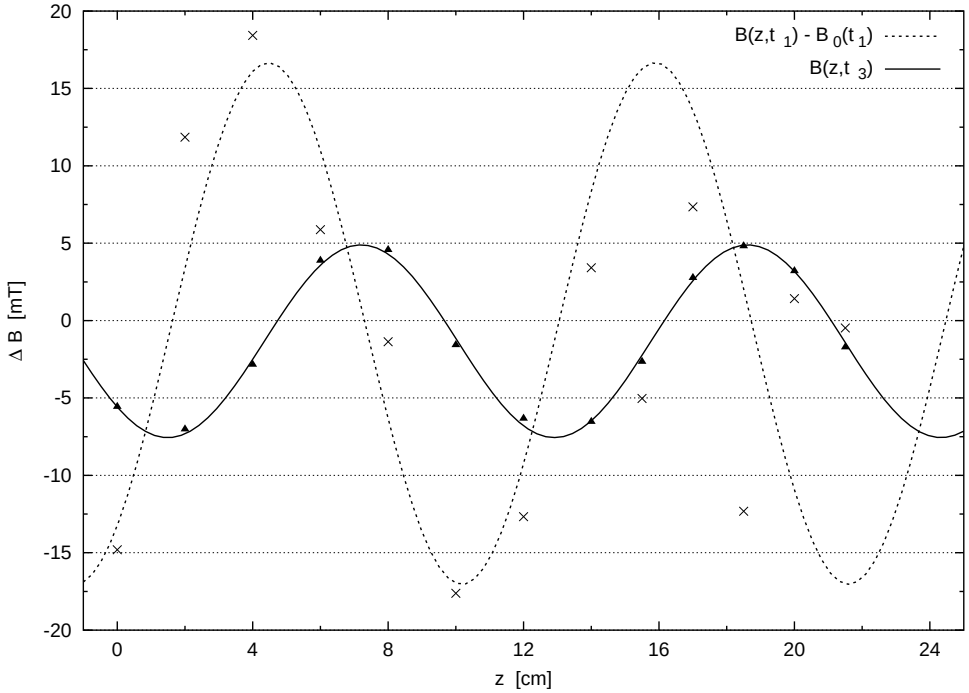

Figure 5.4: Example of two PFPs measured in the short model MBSMS17.V3 at times t_1 and t_3 of the current cycle shown in Figure 5.3.

Parameters	PFP at t_1	PFP at t_3
B_0 $[mT]$	6444	-1.33
B_1 $[mT]$	16.8	6.23
λ $[mm]$	114	114
φ $[rad]$	-0.885	-2.39

Table 5.1: Fitting parameters extracted from Equation 5.5 for both PFPs shown in Figure 5.4

where λ is found to be close to the twist pitch length l_p of the cable used for the inner layer of the coil. Note that here, B_0 and B_1 have a different meaning than the Fourier coefficients of the multipole development of Equation 5.2 and that $B(z,t)$ represents the superposition of all harmonics!

This result showing the coincidence of the wavelength of the magnetic field oscillations with the cable transposition pitch, suggests that slowly decaying current loops exist in the cable even at zero transport current [30]. These loops consist of currents flowing along the cable through one set of strands and returning through another set of strands. The two dimensional network model already described in Chapter 3, shows that the crossover currents between the strands which are responsible for the field variation exhibit a longitudinal periodicity with an interval which is identical with the cable twist pitch length l_p (see Equation 3.16).

The induction effect caused by the variation of the $\dot{B}$ along the cable of a coil can qualitatively account for the longitudinal periodicity seen in all magnets. The observed multipole field pattern results from a complex superposition of the bipolar currents induced in any pair of strands in all turns of the coil. Since the cross–over resistances and the number of pitch lengths between the coil heads will vary from turn to turn and from magnet to magnet, rather different oscillation patterns of the various multipoles must be expected for different magnets. For this reason a quantitative analysis appears not obvious and predictions for a new magnet will be difficult [28].

All the fitting parameters deduced from Equation 5.5 for both PFPs of Figure 5.4 are given in Table 5.1. Concerning the homogeneous term of Equation 5.5 obtained from the fit of the PFP measured at t_1 i.e. $B_0(t_1)$, it is in good agreement with the value of $6430\,mT$ deduced from the transfer function measured by means of the rotating coil technique. The corresponding term measured at t_3, after the suppression of the magnet current, $B_0(t_3)$ is negative because it comes mainly from the remanent magnetization of the superconducting filaments.

The angle φ of Equation 5.5 express the phase between the PFP and an arbitrary origin. The PFPs pictured in Figure 5.4 show a different phase at t_1 and at t_3. This relative phase shift indicates a change of the sign for the two amplitudes $B_1(t_1)$ and $B_1(t_3)$.

The amplitudes $B_1(t_1)$ and $B_1(t_3)$ of the sinusoidal field variation are found to depend strongly on the current cycle performed and will be discussed in the following.

The above introduced examples of the PFP given in Figure 5.4 lead already to a qualitative description of this effect. From Table 5.1 it can be seen that the amplitude $B_1(t_1)$ is clearly larger than $B_1(t_3)$ for one specified cycle. During the ramp–up of the current cycle (i.e. up to t_1) the Rutherford–type superconducting cable charges itself with a non–uniformly distributed current wave. On the plateau of the cycle this wave diffuses slowly, in other words the current leads to be shared more uniformly between the strands. During the ramp–down the

superconducting cable charges itself with a non–uniformly distributed current wave of an opposite sign as compared to the current ramp–up (antiwave). As a consequence, the PFP measured at t_3 is the composition of two waves which can partially cancel out [61].

Some important features can be understood in a more quantitative way with the continuum model presented in Chapter 3 by describing the above introduced picture of the induced wave and antiwave during the current cycle. Considering Equation 3.27 and 3.30 for describing the charging period of the current cycle $\left(1 - e^{-\frac{t}{\tau}}\right)$ and the decay period $\left(e^{-\frac{t}{\tau}}\right)$ on the flat–top, it is possible to link the measurement results to the existing theory based on the two–strand model. For simplification and as a first approach we introduce an effective time constant for the series of Equation 3.30 and we combine all time independent factors of Equation 3.30 to one effective constant referred here to as D. This results in

$$B_1\left(t > t_1\right) = D \cdot \left(1 - e^{-\frac{t_1}{\tau}}\right) \cdot e^{-\frac{t-t_1}{\tau}} \tag{5.6}$$

if we consider that the induced currents can be expressed within the PFP amplitude. As Equation 5.6 describes only the solution after the charging period has stopped at time t_1 and the corresponding decay afterwards, another term has to be added to take into account the discharging period of a complete current cycle. The most general case consists of two different ramp rates for up and down, and thus Equation 5.6 becomes to

$$B_1\left(t > t_3\right) = \left[D \cdot \left(1 - e^{-\frac{t_1}{\tau}}\right) \cdot e^{-\frac{t_2-t_1}{\tau}} - E \cdot \left(1 - e^{-\frac{t_3-t_2}{\tau}}\right)\right] \cdot e^{-\frac{t-t_3}{\tau}} \tag{5.7}$$

if we use the same notation as for the current cycle introduced in Figure 5.3.

The two coefficients D and E of Equation 5.7 are directly linked to the used ramp rates of the current cycle. The influence of the field sweep rate is already given in 3.18 and 3.19. Since the induced steady state current is proportional to the ramp rate, $I_{\max} \propto U \propto \dot{B}$, the ratio of the coefficients D and E is equal to that one of the two ramp rates $\dot{I}_{up}$ and $\dot{I}_{dn}$

$$\frac{D}{E} = \frac{\dot{I}_{up}}{\dot{I}_{dn}} \ . \tag{5.8}$$

State of the PFP at time t_3

Here only the initial state of the PFP after the cycle at t_3 is discussed. Thus Equation 5.7 is reduced to the time $t = t_3$ and this leads to

$$B_1\left(t_3\right) = D \cdot \left(1 - e^{-\frac{t_1}{\tau}}\right) \cdot e^{-\frac{t_2-t_1}{\tau}} - E \cdot \left(1 - e^{-\frac{t_3-t_2}{\tau}}\right) \tag{5.9}$$

where the last exponential describing the decay for $t > t_3$ is disappeared.

For the study of the PFP, especially the amplitude of Equation 5.5 as a function of the current cycle, different precycles were performed with a variation of

- the flat–top time Δt_{ft} by constant top current,
- the flat–top current $I_{\max}$ by constant ramp rate,
- the ramp rates (symmetrical and asymmetrical cycles), i.e. change of t_1 and $t_3 - t_2$ by constant $I_{\max}$.

Flat–top time dependence To begin with the influence of the flat–top duration on the PFP, a measurement series consisting of four different single measurements on the short model magnet MBSMS17.V3 has been performed. The applied current cycles differ in the parameter Δt_{ft} which have been chosen to $500\,s$, $1000\,s$, $2000\,s$ and $3000\,s$. Naturally this causes an increase of the total cycle time t_3 with the same time steps. The other parameters of the current cycle remained unchanged i.e. $40\,A/s$ and $-40\,A/s$ for the ramp–up and the ramp–down respectively and $I_{\max} = 9\,kA$. All four measurements exhibit clear PFPs by means of Equation 5.5 at their respective time t_3 which are shown in Figure 5.5. The deduced fitting parameters are listed in Table 5.2 and will now be discussed.

The homogeneous term of the PFP $B_0\,(t_3)$ seems to decrease with longer cycle time originated from an increase of the flat–top duration.

No variation of the phase was observed. The standard deviation resulting from all four values of φ in Table 5.2 is less than one percent.

Figure 5.6 shows a clear increase of the PFP amplitude in dependence on t_3.The error margins are deduced from the "asymptotic standard error" provided from the fitting process using Gnuplot [60]. This behavior can be explained by using the general Equation 5.9 for $B_1\,(t_3)$. In the case of the applied symmetrical current cycles the duration for the ramp–up is equal to that one for the ramp–down, i.e. $t_1 = t_3 - t_2$. Additional by Equation 5.8 becomes one which results in equal coefficients for the charging and the discharging period, i.e. $D = E$. Thus Equation 5.9 can be rewritten to

$$\begin{aligned} B_1\,(t_3) &= D \cdot \left(1 - e^{-\frac{t_1}{\tau}}\right) \cdot e^{-\frac{t_2 - t_1}{\tau}} - D \cdot \left(1 - e^{-\frac{t_1}{\tau}}\right) \\ &= -D \cdot \left(1 - e^{-\frac{t_1}{\tau}}\right) \cdot \left(1 - e^{-\frac{t_2 - t_1}{\tau}}\right) \\ &= -D \cdot \left(1 - e^{-\frac{t_1}{\tau}}\right) \cdot \left(1 - e^{-\frac{t_3 - 2t_1}{\tau}}\right) \end{aligned} \tag{5.10}$$

where the flat–top duration is expressed by the total cycle time, i.e. $\Delta t_{ft} = t_2 - t_1 = t_3 - 2t_1$ with $t_1 = 225\,s$. The negative sign in Equation 5.10 indicates that a phase shift takes place between the PFP on the flat–top and the PFP after

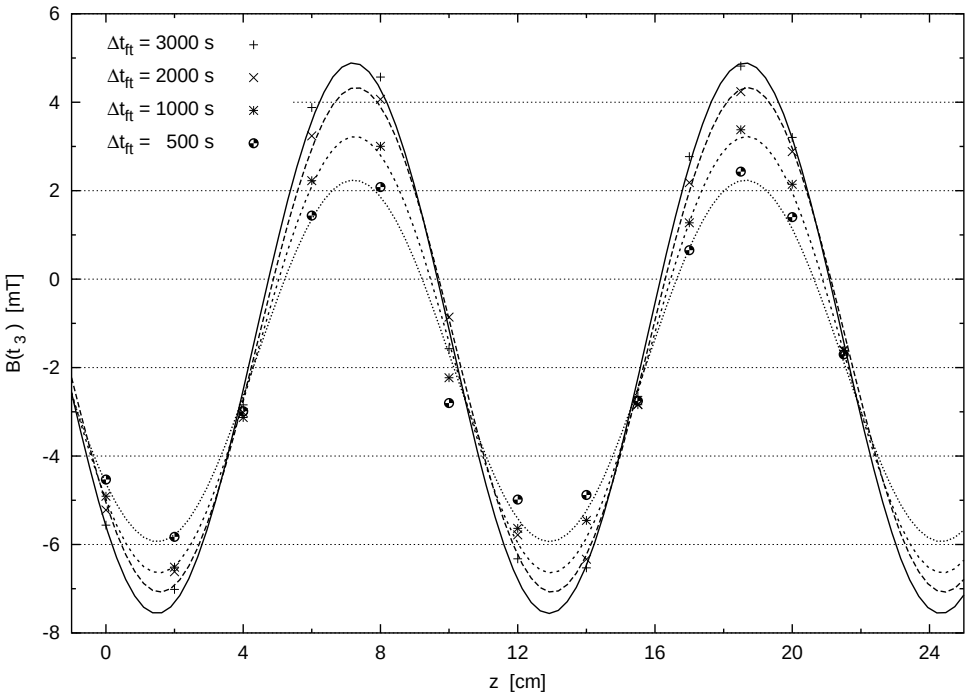

Figure 5.5: Example of the influence of the flat–top duration Δt_{ft} on the PFP measured in the short model MBSMS17.V3 at time t_3. The ramp rates were fixed to $\pm 40\,A/s$, as well as the flat–top current to $9\,kA$. The amplitudes increase for current cycles with longer flat–top durations.

Parameters	$\Delta t_{ft} = 500\,s$	$\Delta t_{ft} = 1000\,s$	$\Delta t_{ft} = 2000\,s$	$\Delta t_{ft} = 3000\,s$
B_0 $[mT]$	-1.85	-1.71	-1.37	-1.33
B_1 $[mT]$	4.09	4.93	5.7	6.23
λ $[mm]$	114	114	114	114
φ $[rad]$	-2.4	-2.42	-2.44	-2.39

Table 5.2: Fitting parameters of the measured data shown in Figure 5.5 for current cycles with different flat–top duration

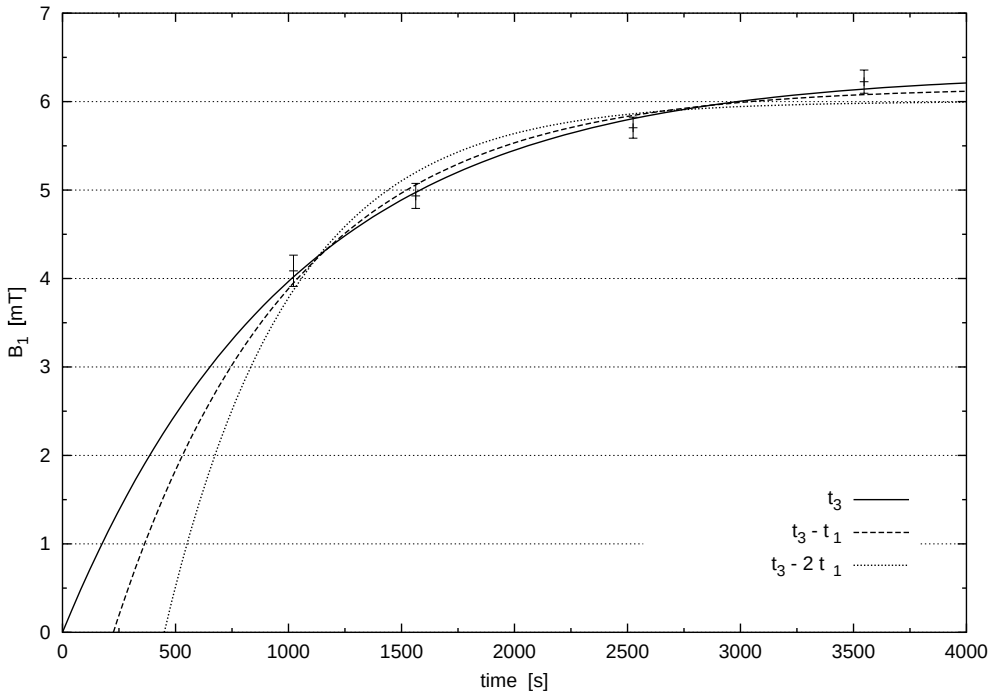

Figure 5.6: The increase of the PFP amplitude for longer flat–top duration can be approximated with three fit functions considering different arguments in the exponential.

the current cycle. This can be included inside the parameter φ of Equation 5.5 and thus we use in the following always positive values for the amplitude.

For describing the PFP amplitude as a function of the flat–top duration, the theory propose to use a fit function like in Equation 5.10. Such a function is shown as a dotted line in Figure 5.6 and the corresponding fit parameters result in $D_{(t_3-2t_1)} = 18\,mT$ and a time constant of $553\,s$. If in this case the flat–top duration is reduced to zero, i.e. $t_3 = 2t_1 = 2t_2$, the two waves for charging and discharging cancel each other completely and no PFP amplitude at all is expected from Equation 5.10. This, however, is in disagreement with measurement results performed on triangle–like forms for the current cycles. Also here a PFP with a defined value for $B_1\,(t_3)$ was observed. Considering this matter a modification of the fit function was applied to satisfy the measured results.

Thus a second fit function was used where the argument in the exponential of Equation 5.10 was reduced from $(t_3 - 2t_1)$ to $(t_3 - t_1)$. The function is drawn with a dashed line in Figure 5.6 and provides fit parameters of $D_{(t_3-t_1)} = 24.6\,mT$ and a time constant of $779\,s$. The function crosses the time axis at time $t_1 = 225\,s$. This implies that the decay of the non–uniformly distributed current wave, induced during the charging period, does not stop at t_2, i.e. at the end of the flat–top, but continues during the discharging period up to t_3. An equivalent interpretation of

this function is given by considering a decay during the charging period which is stopped at time t_2. As it can be seen from Figure 5.10 the amplitude does not vanish for a cycle without any flat–top duration which is for our example at time $t_3 = 2t_1 = 450\,s$.

Finally the best fit is achieved by using a function which is presented as a continuous line in Figure 5.6 and does not consider any time shift in the exponential. Equation 5.10 is then reduced to

$$B_1(t_3) = -D \cdot \left(1 - e^{-\frac{t_1}{\tau}}\right) \cdot \left(1 - e^{-\frac{t_3}{\tau}}\right) \tag{5.11}$$

where again positive values for the amplitudes are considered. Here the parameters are $D_{(t_3)} = 31.9\,mT$ and for the time constant $1016\,s$. This behavior supposes that the decay of the non–uniformly distributed current wave already starts at the beginning of the current cycle, quasi in parallel to the charging process and also continues during the discharging of the magnet. For the charging of the antiwave no decay is considered in equation 5.11, because this process describes already a lowering of the total energy inside the system.

Flat–top current dependence It has also been observed on the short model magnet MBSMS17.V3 that both amplitudes, on the flat–top $B_1(t_1)$ and right after the cycle $B_1(t_3)$, increase with the maximum current of the cycle. We compare the results from the measurements with the current cycles described above with a flat–top current of $9\,kA$ and that one from additional measurements with current cycles at a higher flat–top current, namely at $13\,kA$. Such a high current is close to the nominal critical current and therefore the ramp rate was decreased from $40\,A/s$ to $10\,A/s$ for the current interval from 10 to $13\,kA$. The flat–top duration was set to be the same for both cycles $\Delta t_{ft} = 500\,s$.

Table 5.3 shows the results for the PFP amplitudes for both current cycles on the flat–top at time t_1 and at time t_3 after the cycle is finished. Especially after the charging period a significant increase of the PFP amplitude for the higher flat–top current is observed. But also the value after the current cycle is larger for increasing flat–top current.

PFP amplitude	Flat–top current of $9\,kA$	Flat–top current of $13\,kA$
$B_1(t_1)$ $[mT]$	16.8	32
$B_1(t_3)$ $[mT]$	4.09	6.16

Table 5.3: Values for the PFP amplitude for two current cycles with different flat–top currents measured on MBSMS17.V3

In principle Equation 5.10 can be reused to interpret the results of Table 5.3, because also here the current cycles are symmetrical. But in contrary to the situation of a changing plateau time, here the charging term $\left(1 - e^{-\frac{t_1}{\tau}}\right)$ is

responsible for the increase of the amplitude. Figure 5.3 and also Equation 5.4 show clearly that a higher flat–top current requires a longer ramp duration t_1 at constant ramp–up rate. Especially for the example given above where the PFP amplitudes are compared at t_3 for two current cycles with the same flat–top time of $500\,s$ but different flat–top currents a significant change of t_1 produce the difference in $B_1\,(t_3)$. For the current cycle with a flat–top current of $9\,kA$ and a ramp rate of $40\,A/s$ the ramp–up duration is $225\,s$. According to Equation 5.10 the value for the amplitude at time t_3 is expressed by

$$B_1\,(t_3)^{9\,kA} = -D \cdot \left(1 - e^{-\frac{225}{\tau}}\right) \cdot \left(1 - e^{-\frac{\Delta t_{ft}}{\tau}}\right) \quad . \tag{5.12}$$

The second cycle reached the flat–top after $550\,s$ because the current was ramped from zero up to $10\,kA$ within $250\,s$, i.e. a ramp rate of $40\,A/s$, followed by a further ramp–up to $13\,kA$ at $10\,A/s$. Taking into account the change of the ramp–rate, a second term for the charging period is considered. Equation 5.8 provides the coefficient for this second term which is a quarter less in the case of $10\,A/s$ ramp rate. For this current cycle Equation 5.10 must be modified to

$$B_1\,(t_3)^{13\,kA} = -D \cdot \left[\left(1 - e^{-\frac{250}{\tau}}\right) + \frac{1}{4} \cdot \left(1 - e^{-\frac{300}{\tau}}\right)\right] \cdot \left(1 - e^{-\frac{\Delta t_{ft}}{\tau}}\right) \quad . \tag{5.13}$$

Calculating the ratio of Equation 5.13 and Equation 5.12 gives

$$\frac{B_1\,(t_3)^{13\,kA}}{B_1\,(t_3)^{9\,kA}} = \frac{1}{4} \cdot \frac{5 - 4 \cdot e^{-\frac{250}{\tau}} - e^{-\frac{300}{\tau}}}{1 - e^{-\frac{225}{\tau}}} \approx 1.4 \tag{5.14}$$

for time constants extracted from the previous section. The result of Equation 5.14 is in quite good agreement with the values given in Table 5.3 where the ratio of the two amplitudes at time t_3 is $6.16/4.09 = 1.5$.

Ramp rate dependence Up to now only symmetrical current cycles with the same ramp rate for up and down have been discussed. Figure 5.7 shows an example for two PFPs measured on the short twin aperture model MBSMT4.V2 at time $t_3 = 1365\,s$. The first part of the applied current cycle was in both cases the same, namely a ramp–up to $12.5\,kA$ at $20\,A/s$. For the symmetrical cycle (that one with the smaller PFP in Figure 5.7) the ramp–down was performed with $-20\,A/s$ after a flat–top duration of $50\,s$. Because of the ramp–down of $-400\,A/s$ for the asymmetrical cycle the plateau time was increased to $644\,s$ to achieve the same total cycle time for both measurements. The fitting parameters for both PFPs are given in Table 5.4.

Here the main parameter influencing the PFP amplitude comes from Equation 5.8. The increase of the value for the ramp–down from $-20\,A/s$ to $-400\,A/s$ generates a ratio of

$$\frac{D}{E} = \frac{20}{400} \quad \Leftrightarrow \quad 20D = E$$

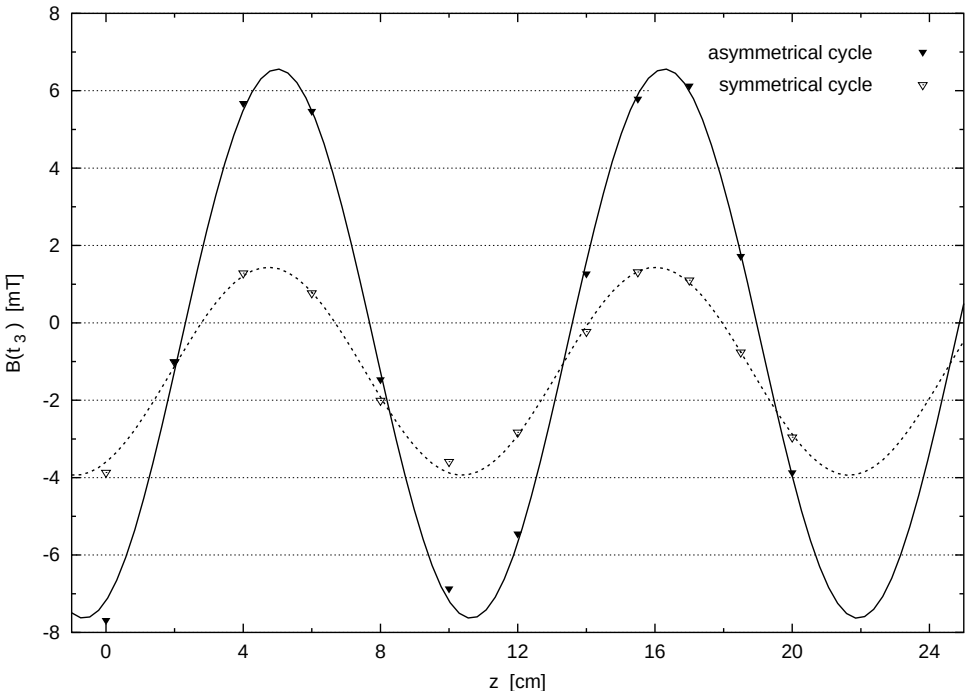

Figure 5.7: Example of the influence of the ramp rates on the PFP measured in the short model MBSMT4.V2. The smaller PFP was observed after a current cycle with $\pm 20\,A/s$ for up and down, and for the larger one the ramp–down was changed to $-400\,A/s$.

Parameters	Symmetrical cycle	Asymmetrical cycle
B_0 $[mT]$	-1.25	-0.54
B_1 $[mT]$	2.69	7.10
λ $[mm]$	113	113
φ $[rad]$	-1.07	-1.21

Table 5.4: Fitting parameters extracted from Equation 5.5 for both PFPs shown in Figure 5.7

for the two coefficients of Equation 5.9. Thus the discharging term for the asymmetrical cycle is much larger compared to that one from the symmetrical current cycle. The effect of the longer flat–top duration on the asymmetrical cycle is here smaller. From the study with different plateau times we have seen that the term describing the decay on the flat–top starts already at the beginning of the charging period. However this part is the same for both current cycles and thus the influence of $\dot{B}$ prevails.

The two–strand model predicts for the ramp rate dependence the right behavior in a qualitative way. A discussion of the values given in Table 5.4 for the amplitudes in a more quantitative way seems, especially for this case, not possible.

Dynamic behavior

Due to the difference in the measurement protocol for the short models and the full–scale magnets, it was only possible to investigate the dynamic behavior of the PFP for the short model dipoles. It should be mentioned that the decay of the PFP amplitude on the flat–top was too low to be measured. Thus in the following only the time manner of the PFP built after the current cycle, i.e. $t \geq t_3$, will be discussed.

In some cases the PFP and its parameters were measured during several hours and even days. The longest measurement was performed during 81 hours after the end of the current cycle and a clear PFP can still be observed after this long decay duration.

As an example Figure 5.8 shows three PFPs measured on the short magnet model MBSMT4.V5 at different times $t > t_3$. They correspond to the same current cycle with a ramp–up to $12.5\,kA$ at $5\,A/s$ followed by a ramp–down at $-400\,A/s$ after a flat–top time of $120\,s$, i.e. an asymmetrical cycle. It can be clearly seen that the shape of the PFP remains stable also for times of 9 and 81 hours, respectively, after the current cycle. All these PFPs have been approximated by Equation 5.5 with the fitting parameters given in Table 5.5. Already from this example, by comparing the three values of the amplitude at different times after the current cycle, it can be seen that the decay is much faster during the first time period than that one during the second time period from $t = 9.2$ hours to $t = 81.3$ hours.

By extracting the fit parameters for the PFP for all recorded data points in the decay period (every 1 to 2 minutes) the PFP dependence on time can be studied in a more quantitative way. Considering the amplitude of the PFPs as a function of time, an exponential behavior for the decay is assumed which is in agreement for the solution of the diffusion like Equation 3.26.

For illustration of the PFP amplitudes as a function of time larger than t_3 we reuse the examples, consisting of four PFPs after current cycles with different flat–top durations, shown already in Figure 5.5. The time constants extracted

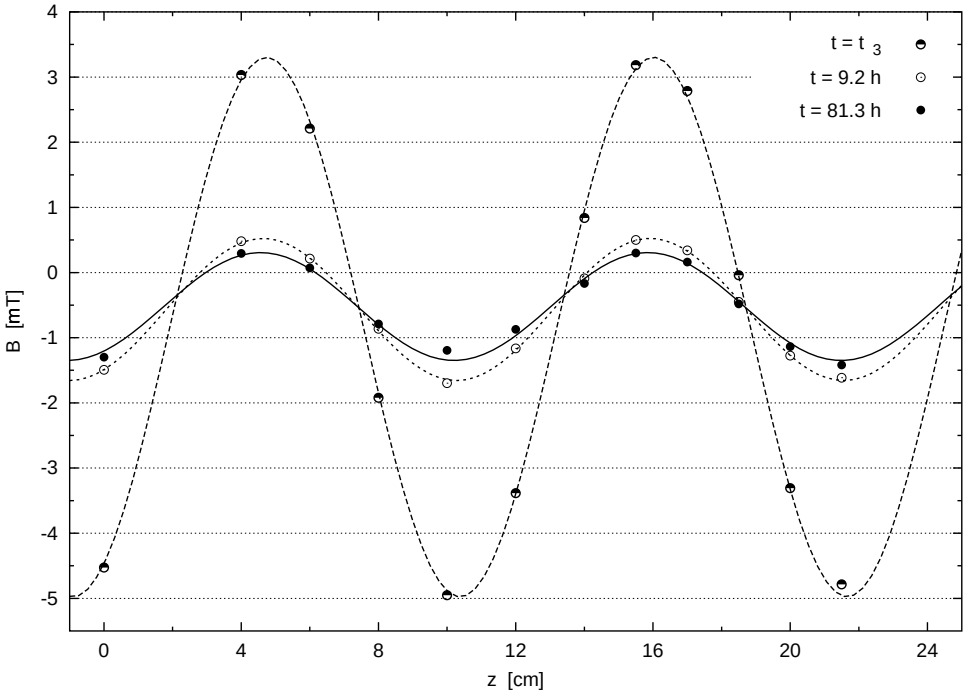

Figure 5.8: Example for the time behavior of the PFP measured in the short model MBSMT4.V5 after an asymmetrical current cycle with a ramp–up to $12.5\,kA$ at $5\,A/s$, a flat–top duration of $120\,s$ and a ramp–down at $-400\,A/s$. The largest PFP was measured at time t_3 whereas the amplitude is much smaller after 9 hours of decay. Even 81 hours after the current cycle, the measured data can be well approximated by Equation 5.5.

Parameters	PFP at $t = t_3$	PFP at $t = 9.2\,h$	PFP at $t = 81.3\,h$
B_0 $[mT]$	-0.84	-0.57	-0.52
B_1 $[mT]$	4.14	1.09	0.83
λ $[mm]$	113	113	113
φ $[rad]$	-1.07	-1.01	-0.97

Table 5.5: Fitting parameters of the measured data shown in Figure 5.8 at three different times of decay

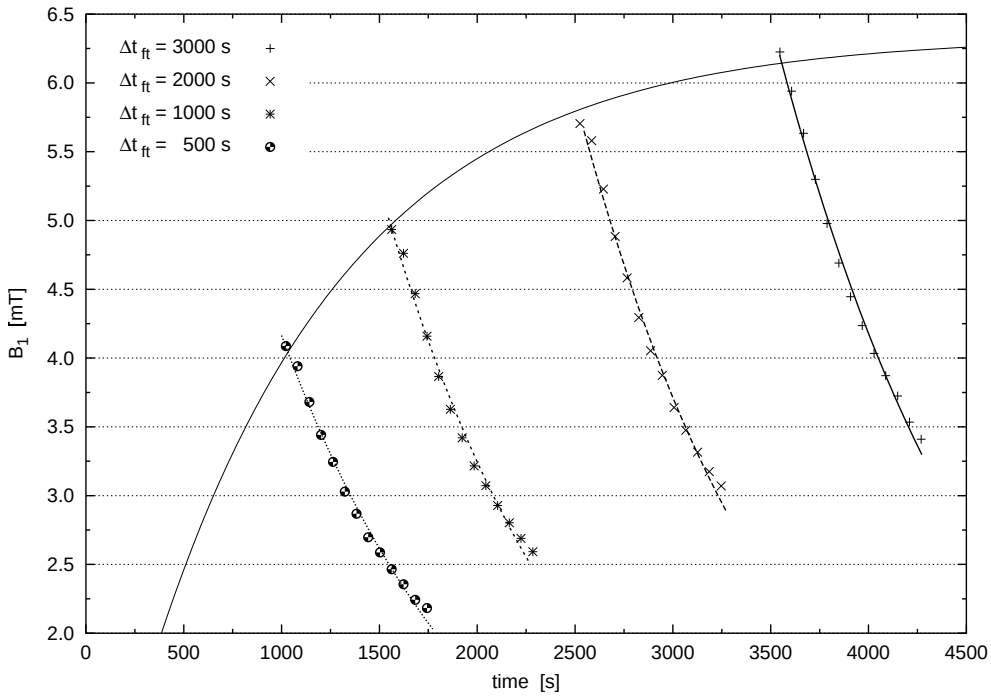

Figure 5.9: The decay of the PFP amplitudes in a time interval of $10\,mn$ after t_3 for current cycles with different flat–top durations. The measurement parameters were already introduced in Figure 5.5.

Parameters		$500\,s$	$1000\,s$	$2000\,s$	$3000\,s$	Mean
D	$[mT]$	62.1	45.9	39	41	47 ± 10
τ_1	$[s]$	1074	1041	1081	1150	1086 ± 46
$D_1\,(t_3)$	$[mT]$	10.6	22.2	59.6	135	

Table 5.6: Fitting parameters of the decay of the PFP amplitudes shown in Figure 5.9 for current cycles with different flat–top durations

from the used fit functions of Figure 5.6 are in the range of about 10 minutes. Thus we consider, as a first step, a time interval for the decay of the amplitudes which is limited between t_3 and $t_3 + 10\,mn$. This situation is shown in Figure 5.9 where only the first few values for the amplitudes after the end of the current cycles are presented. In this case Equation 5.7 becomes to

$$\begin{aligned} B_1\left(t_3 < t < t_3 + 10\,mn\right) &= D \cdot \left(1 - e^{-\frac{t_1}{\tau}}\right) \cdot \left(1 - e^{-\frac{\Delta t_{ft}}{\tau}}\right) \cdot e^{-\frac{t-t_3}{\tau}} \\ &= D_1\left(t_3\right) \cdot e^{-\frac{t}{\tau}} \ . \end{aligned} \tag{5.15}$$

which is similar to Equation 5.10 but considering an exponential decay with one time constant after the end of the current cycle, i.e. the superposition of the two waves for charging and discharging. It was found that the time constants are independent on the different flat–top durations of the used current cycles. The calculation of the mean value for the four time constants results in $1086\,s$ with a standard deviation of $46\,s$. Whereas the coefficients $D_1\left(t_3\right)$ are directly linked to the different values of Δt_{ft} in the current cycles. As the two fit parameters of Equation 5.15 strongly depend on the data points considered, i.e. the time duration after t_3, this solution should be seen as an interim result.

Considering the same measurements discussed above but with increasing of the decay time up to about 8 hours the fitting Equation 5.15 has to be extended to at least two exponentials describing the fast decay in the beginning and the very slow one afterwards. With the help of a third time constant the transient between the fast and the slow decay can be described even better, whereas the use of an additional forth exponential term does not improve the accuracy of the fit. Thus, finally, we apply a function with a series of three exponentials

$$B_1\left(t_3 < t < 8\,h\right) = D_1 \cdot e^{-\frac{t}{\tau_1}} + D_2 \cdot e^{-\frac{t}{\tau_2}} + D_3 \cdot e^{-\frac{t}{\tau_3}} \tag{5.16}$$

to describe the time dependence of the PFP amplitude over a time of about 8 hours after the current cycle.

Figure 5.10 shows the total decay of the amplitudes with the approximation of Equation 5.16. The time axis in seconds is plotted in logarithmic scale to illustrate better the quality of the fit function consisting of three exponentials. All fitting parameters are summarized in Table 5.7 as well as the calculated mean values for the three time constants and their corresponding standard deviations.

The comparison of the extracted three time constants with Equation 3.28 shows that the time constants can not be interpreted as a function of $(1/n^2)$, the inverse square of the summation index in Equation 3.27. Additional it is not possible to estimate the longest time constant τ_3 from Equation 5.16 with the help of Equation 3.29 where the geometry of a two–strand cable determines the value for the time constant. This situation indicates that the three terms of Equation 5.16 may have different origin and are not directly linked to each other. A possible explanation can be the three sources of induced currents inside a Rutherford–type cable:

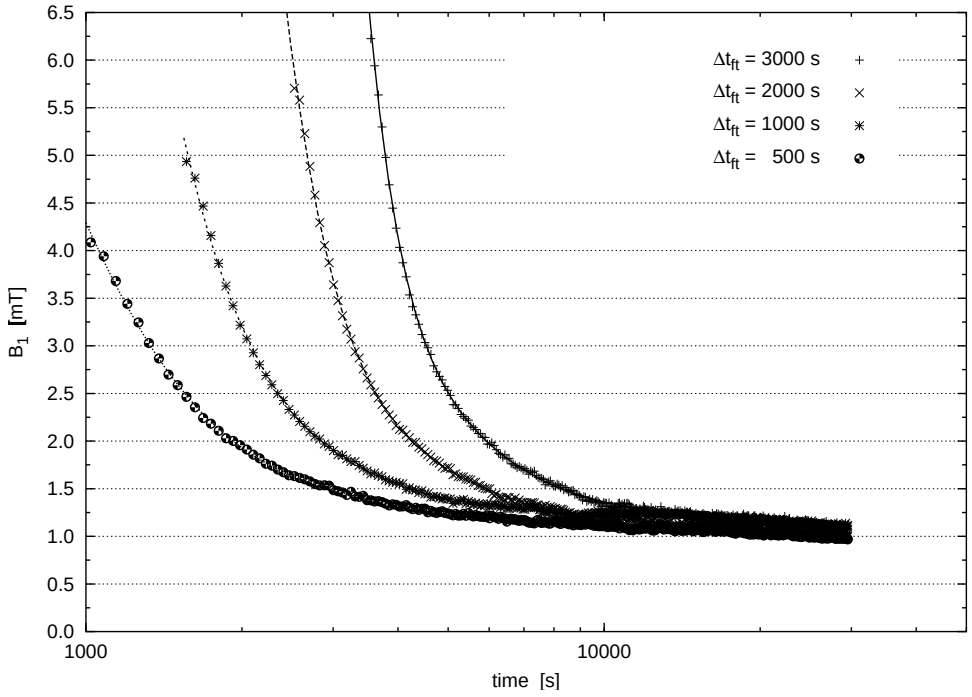

Figure 5.10: The decay of the PFP amplitudes approximated by Equation 5.16 for data measured in the short model MBSMS17.V3 during a decay duration of about eight hours. The time axis is plotted in logarithmic scale.

Parameters	500 s	1000 s	2000 s	3000 s	Mean
D_1 $[mT]$	19.1	97	452	5297	
τ_1 $[s]$	475	406	504	471	464 ± 41
D_2 $[mT]$	1.32	5.78	5.81	12.3	
τ_2 $[s]$	2023	1263	2005	2039	1833 ± 380
D_3 $[mT]$	1.17	1.33	1.24	1.37	
τ_3 $[s]$	165341	156923	132805	129811	146220 ± 17601

Table 5.7: Fitting parameters of the decay of the PFP amplitudes shown in Figure 5.10 for current cycles with different flat–top duration

- the local change of the field sweep rate,
- the local distribution of the cross–contact resistances,
- an external field variation or distribution of the cross–contact resistances in the joints.

5.2.3 Influence of the magnets characteristic on the PFP

All investigated superconducting dipoles were submitted to the so–called current reference cycle. Because of a limited measurement time during the tests of the long prototype and pre–series magnets the reference–cycle for the long magnets differ in a shorter flat–top time comparing to that one used in Block 4 for the short dipole models.

Starting with the short dipoles measured in Block 4 a current cycle was chosen after which all short magnets showed a clear PFP. This current reference cycle is described with a ramp–up to $9\,kA$ at $40\,A/s$ followed by a ramp–down at $-40\,A/s$ after a flat–top time of $3000\,s$. For comparison of the measurements performance on the six short dipole models the following results are given for the same reference time of roughly one hour after the beginning of the cycle. The measurement data and their corresponding fit functions are shown in Figure 5.11 and 5.12, respectively. The upper figure summarizes the three single aperture models while the second one shows the results for the twin aperture dipoles. The scale of the axes was set to be equal for both charts.

Magnet	$B_0\ [mT]$	$B_1\ [mT]$	$\varphi\ [rad]$	$\lambda\ [mm]$
MBSMS17.V3	−1.27	4.98	−2.34	114
MBSMS23.V3	−1.49	2.01	−2.92	115
MBSMS23.V4	−1.25	1.30	−2.72	115
MBSMT4.V2	−2.00	2.76	−1.03	113
MBSMT4.V5	−1.80	2.34	−1.02	113
MBSMT5.V3	−1.28	0.67	−2.93	113

Table 5.8: Fitting parameters for all six measured short dipole models at the same reference time after applying a specified reference–cycle

All the fitting parameters deduced from Equation 5.5 for the PFPs of both Figures 5.11 and 5.12 at the same reference time are given in Table 5.8.

The comparison of the amplitudes in Table 5.8 with the specific magnet properties shows that no correlation between the B_1 values and the cable manufacturers can be found. For example, the cable used for MBSMS17 and MBSMT4 is produced by the same company. For the other two magnets the cable manufacturer is different. Also no influence of the number of apertures on the PFP amplitude can be observed. All measured short models have passed through the

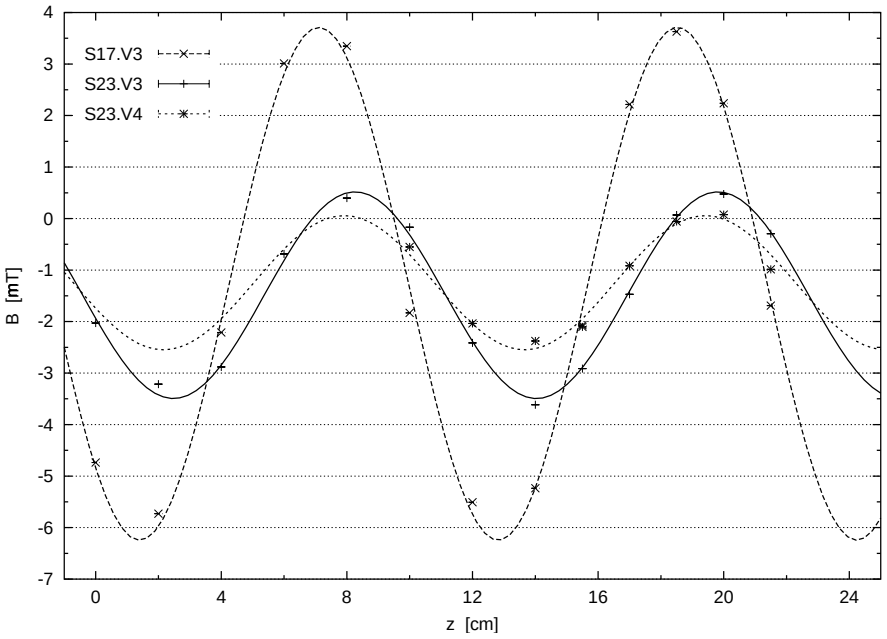

Figure 5.11: PFP measured after the reference–cycle for three short single aperture dipole models.

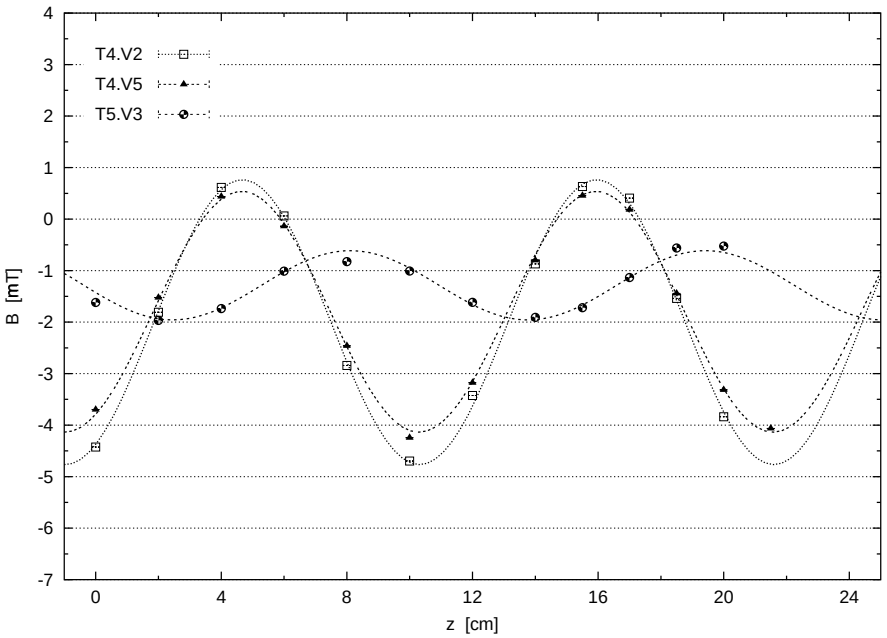

Figure 5.12: PFP measured after the reference–cycle for three short twin aperture dipole models.

Magnet	B_0 $[mT]$	B_1 $[mT]$	φ $[rad]$	B_2 $[\mu T/cm]$
MBP2 O1	-0.72	0.16	2.77	0.60
MBP2 A2	0.06	0.13	2.53	5.14
MBP2 O2	-0.74	0.18	3.70	-5.27
MBPS O01	-0.12	0.15	3.22	20.2
MBPS A01	0.61	0.25	0.24	13.5

Table 5.9: Fitting parameters deduced from Equation 5.17 for the five measured long prototype and pre–series dipoles at the same reference time after applying a specified reference–cycle

same thermal cycle for the so–called curing process. This indicates that the differences in B_1 cannot be determined by the curing parameters. Finally we can say that the amplitude variations given in Table 5.8 for different magnets have its origin mainly in:

- a local variation of the field sweep rate,
- a different value of the average cross–contact resistance R_c for different magnets,
- a local distribution of R_c for each magnet.

In the case of the long dipoles the flat–top duration of the current reference cycle was reduced to $\Delta t_{ft} = 1000\,s$ while the ramp rates for up and down and the maximum current stayed unchanged in comparison to the short dipoles. The PFPs for the long magnets showed an additional field gradient and therefore Equation 5.5 has been modified considering this behavior. Especially for the two pre–series dipoles the relation

$$B\left(z,t\right) = B_0\left(t\right) + B_1\left(t\right) \cdot \sin\left(\frac{2\pi z}{\lambda} + \varphi\right) + B_2 \cdot z \tag{5.17}$$

fits much better to the measured data. Anyway the coefficient B_2 representing the field gradient is rather small and does not influence the PFP effective.

All the fitting parameters are given in Table 5.9. The amplitude values show a much smaller spread than the B_1 values observed inside the apertures of the short dipole models. This result can be explained by better control of the cross–contact resistance R_c for the latest dipoles tested. Indeed a special program was launched at CERN to control the oxidation process of the strand coating ($SnAg_{5\%wt}$) for the superconducting cables of the 3rd generation of the long prototypes, pre–series and series magnets [62].

5.3 Measurements and analysis of the Field Advance

The value for the cross–contact resistance R_c between the strand of the two layers of the superconducting Rutherford–type cable can be derived from measurements of the magnetic field by using the Hall probe devices already described in Chapter 4. During the ramp of a magnet, the time derivative of the external magnetic field $\dot{B} = \frac{dB}{dt}$ appears and additional currents are induced. In the case of an uniform main field sweep rate along the cable axis, $\frac{d\dot{B}}{dx} = const.$, the so–called interstrand coupling currents are established, i.e. an uniform current distribution inside the cable. These currents provoke a distortion of the main magnetic field which produces the so–called main Field Advance (FA).

Figure 5.13 shows a sketch of a magnet based on the six–block design with the different components of the magnetic field. The main field is represented by the large arrows pointing all in the same direction. The small arrows, which change their direction from the inner to the other part of the magnet, illustrate the FA originating from an uniform field sweep rate which produces the uniform induced current distribution.

In a first approach the total resulting field in the magnet during the whole current cycle can be expressed in a Taylor–series with the dependences of the magnetic field only on the main transport current I and the current sweep rate $\dot{I} = \frac{dI}{dt}$

$$B\left(I, \dot{I}\right) \approx B_c + \alpha I + \beta \dot{I} + \dots \ . \tag{5.18}$$

Thus the FA can be measured by comparing the field values on the ramp–up and the ramp–down of the current cycle (see Figure 5.14). In principle this difference can be calculated simply by using Equation 5.18 for a constant current value I_B and neglecting higher orders of the Taylor–series. This leads to the expression for the FA

$$\Delta B = \beta \dot{I} = \frac{1}{2}\left[B_{up}\left(I_B, \dot{I} > 0\right) - B_{dn}\left(I_B, \dot{I} < 0\right)\right] \tag{5.19}$$

where the stronger influence of the total field $B\left(I, \dot{I}\right)$ on the current I is eliminated and only the dependence on the ramp rate $\dot{I}$ can be investigated.

5.3.1 Measurements protocol

After the cool down ($T \leq 1.9\,K$) the magnet was submitted to a current cycle which can be described in the same way as it was discussed in the previous section (see Figure 5.3 and also Figure 5.14). For the FA experiments the main parameters of the current cycle remained unchanged for all measured magnets.

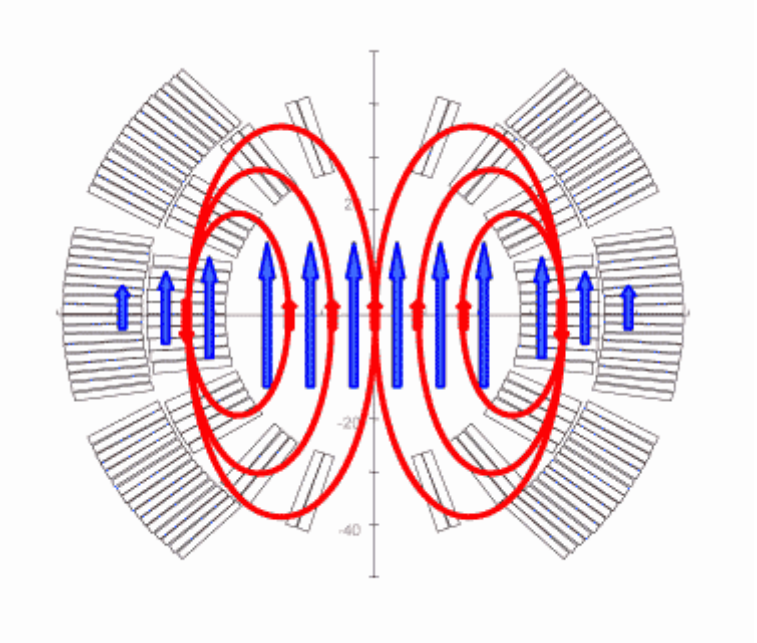

Figure 5.13: The main field and the FA in the magnet due to an unfirom current distribution inside the cables.

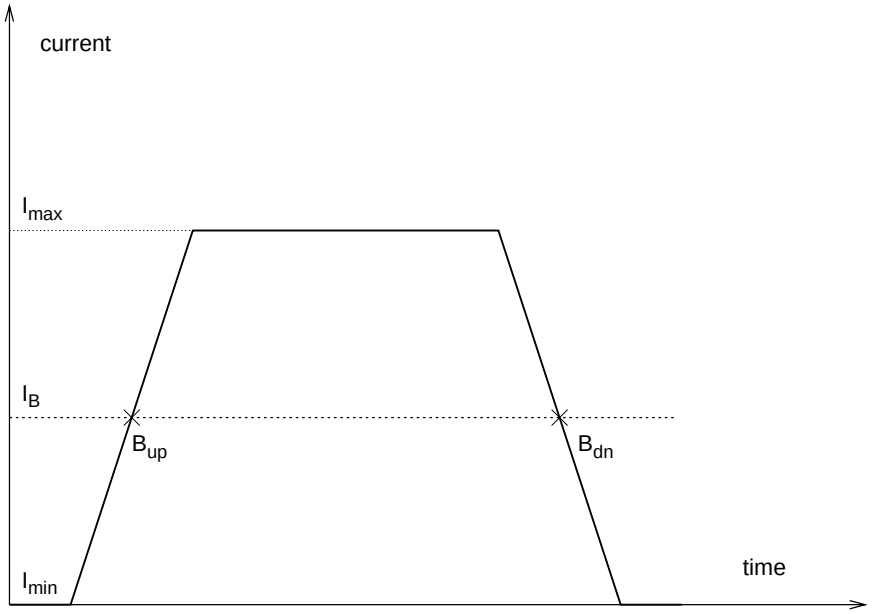

Figure 5.14: A typical current cycle with a specified ramp rate for the FA measurements. It is also intimated that the corresponding field values for a fixed current I_B are different for the ramp up and the ramp down.

The two current extrema were set to $I_{\min} = 1000\,A$ and $I_{\max} = 3000\,A$ respectively and the flat–top duration was about $50\,s$. As already mentioned the effect of the FA depends on the time derivative of the external magnetic field and thus one measurement series consists of several single measurements with the same cycle properties except the applied ramp rate. For example a typical measurement series covers five single measurements with ramp rates from $30\,A/s$ up to $70\,A/s$ in steps of $10\,A/s$. All current cycles used here are symmetrical, i.e. the same ramp rate for up and down (trapezoidal shape) is applied.

The raw data obtained from every measurement are recorded on a SUN workstation in an ASCII file consisting of the current values and five channels for the Hall voltages during the whole current cycle. The further data treatment is mainly based on a computer program written in the Python language [63]. The whole source and a short description of the Python code is given in Appendix A.

5.3.2 Transitory regime

The results for the field differences calculated from Equation 5.19 can be divided into two parts. The first part referred to as stationary regime where the ΔB values are constant will be discussed later on. The second part close to the current extrema of the cyle at $I_{\min}$ and $I_{\max}$, i.e. the transition from $\dot{I} = 0$ to $\dot{I} = const.$ and also from $\dot{I} = const.$ to $\dot{I} = 0$ during the current cycle, the field differences decrease and increase respectively which is referred here to as the transitory regime. Figure 5.15 illustrates this behavior for a measurement with a ramp rate of $30\,A/s$ performed on the prototype dipole MBP2 A2. The x-axis can be expressed in two ways, directly by using the current values of the current cycle during the ramp–up, or by a transformation of the recorded data into time values. The origin of time is again set to be equal to the beginning of the ramp–up of the current cycle and the time grid is determined by the integration time used for the dedicated measurement which is typically $0.1\,s$.

The measurements have shown that the two parts of the transitory regime are symmetrical with respect to the stationary part. Thus the field differences can be approximated by an exponential function

$$b\,(t) = A_0 + A_1 \cdot e^{-\frac{t-t_1}{\tau}} + A_2 \cdot e^{\frac{t-t_2}{\tau}} \tag{5.20}$$

where only one time constant τ is used to describe the decrease on the left side and the increase on the right side of the curve shown in Figure 5.15. The two time values t_1 and t_2 of Equation 5.20 are fixed and take into account the time shift to the respective beginning of the decay. The constant A_0 indicates the stationary regime and it is comparable to the mean value of the field differences between the two branches of the transitory regime. All fitting parameters of the example shown in Figure 5.15 are summarized in Table 5.10.

As the real shape of the transport current during the cycle differs slightly from the ideal case shown in Figure 5.14 a probable influence of this effect on the FA

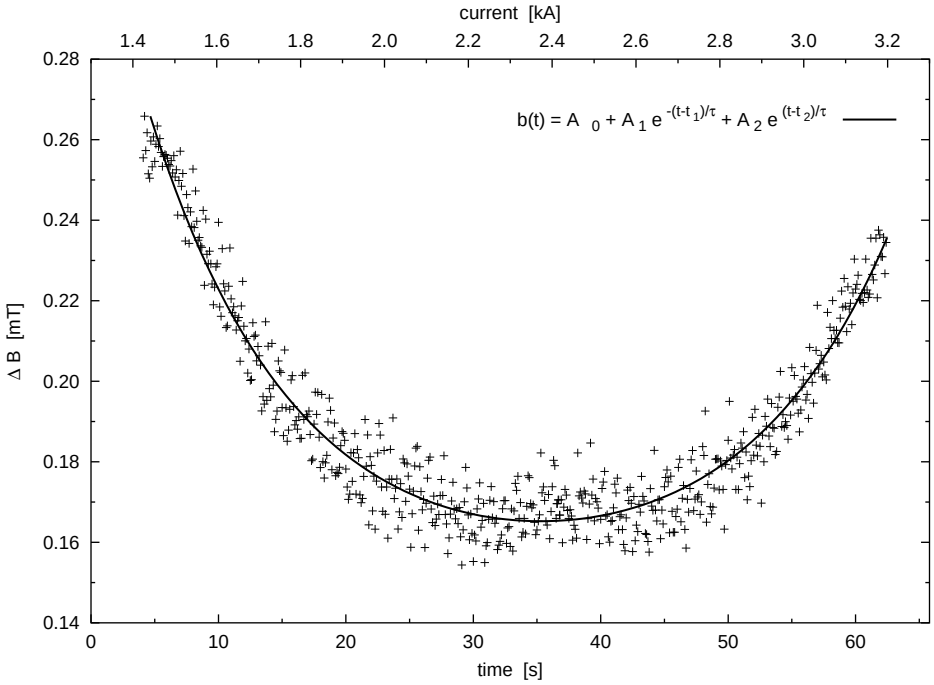

Figure 5.15: An example (MBP2 A2, HP3, $\dot{I} = 30\,A/s$) for the ΔB-values versus the current at the ramp up. Using a time axis determined form the integration time of the measurement a fit function describing the transitory part can be applied to the data points.

A_0 $[mT]$	A_1 $[mT]$	A_2 $[mT]$	τ $[s]$
0.15	0.12	0.02	11.4

Table 5.10: Fitting parameters extracted from Equation 5.20 for the ΔB-values shown in Figure 5.15

was investigated. Especially the beginning of the current ramp–up is performed in a specific way by using first an exponential and then polynomial continuous increase of the current in function of time. The same method is applied for reaching the flat–top current. These two time periods during the ramp–up where the current shape differs from the linear excitation are rather short with time constants in the millisecond range. This is one order of magnitude smaller in comparison to the observed time constants for the transitory regime of the field differences. Therefore a direct influence of the non–linear current shape can be neglected and is not responsible for the transitory behavior of the FA. It can be said that the time dependence of the FA represents the transient process of the establishing of coupling currents inside the superconducting Rutherford–type cables [64].

It was found that the time constants τ extracted from Equation 5.20 did not

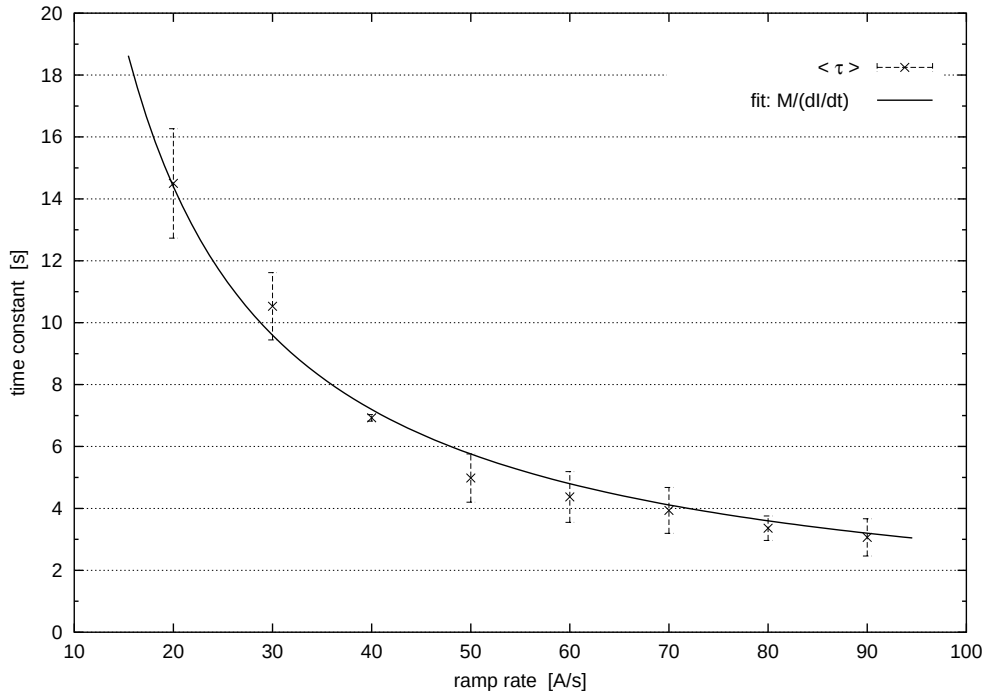

Figure 5.16: The dependence of the time constants deduced from Equation 5.20 on the ramp rate for the prototype magnet MBP2 A2.

depend strongly on the measurement position along the magnet axis however similar values of τ for both used Hall probes were found and an influence of the ramp rate on the time constants was observed. The increase of τ for decreasing ramp rates can be desribed by the relation

$$\tau\left(\dot{I}\right) = \frac{M}{\dot{I}} \ . \tag{5.21}$$

This dependence is shown in Figure 5.16 for the prototype diploe MBP2 A2. The error–bars for each point in the figure represents the standard deviation deduced from the averaging process of the two Hall probes measuring the field in a distance of 5.5 cm along the magnet axis.

The fit parameter M for all measured magnets is shown in Table 5.11.

MBP2 O1	MBP2 A2	MBP2 O2	MBPS O01 a1	MBPS O01 a2
238	288	250	324	377

Table 5.11: The fit parameter M in Ampere for all measured long prototype and pre–series dipoles deduced from Equation 5.21

5.3.3 Stationary regime

For the calculation of the contact–resistance R_c only the ΔB values which are independent of time are considered. This stationary regime has been found to be around the mean value of the two current extrema $\frac{I_{\min}+I_{\max}}{2}$ with a range of $\pm 250\,A$. Considering, for example, a current cycle from $I_{\min} = 1000\,A$ up to $I_{\max} = 3000\,A$ the stationary regime is limited into a current interval of $1750\,A$ and $2250\,A$. Applying this current range in the Python computer program (see Appendix A) the mean value and the corresponding standard deviation of all field differences within the stationary regime is calculated.

This procedure was performed for all single measurements with different ramp rates for one measurement series. Thus the dependence of the averaged field differences on the ramp rate $dI/dt = \dot{I}$ can be evaluated. This behavior is described by a straight line

$$f\left(\dot{I}\right) = \beta_0 + \beta\dot{I}\ . \tag{5.22}$$

Figure 5.17 illustrates this linear function where an example for the full–scale prototype diploe MBP2 O2. The fit parameters deduced from Equation 5.22 for the two different positions of the used Hall probes (HP3 and HP9) along the magnet axis are given in Table 5.12.

The extrapolation of Equation 5.22 to zero ramp rate, $f\left(\dot{I} \to 0\right) = \beta_0$, corresponds to the contribution in the main magnetic field due to the difference in the magnetization of the superconducting filaments on the way up and down. The slope β of the linear fit function 5.22 is used to determine the cross–contact resistance of the magnet. This is achieved by using Equation 5.23

$$R_c = \frac{C}{\beta} \tag{5.23}$$

where C is the so–called field factor. This factor is computed from a numerical simulation program and represents the theoretical values of field error for a specific magnet, e.g. number of apertures and blocks, magnet length, number of strand and the twist pitch length, etc. [65]. For the full–scale prototype and pre–series diploes a field factor $C = 440\,\Omega T s A^{-1}$ was used to calculate the cross–contact resistance R_c.

The FA measurements inside the apertures of the two pre–series dipoles MBPS O01 and MBPS A01 were performed on several positions along the magnet axis. After each measurement series the Hall probes set–up was axially moved at fixed orientation. This scan of the magnetic field provides a certain spread of the fit parameters of Equation 5.22 and the corresponding values for R_c. Especially the results for the cross–contact resistances can then be compared with results obtained by the rotating coil technique providing integral values along the magnet axis which are affected by a substantial dispersion [66].

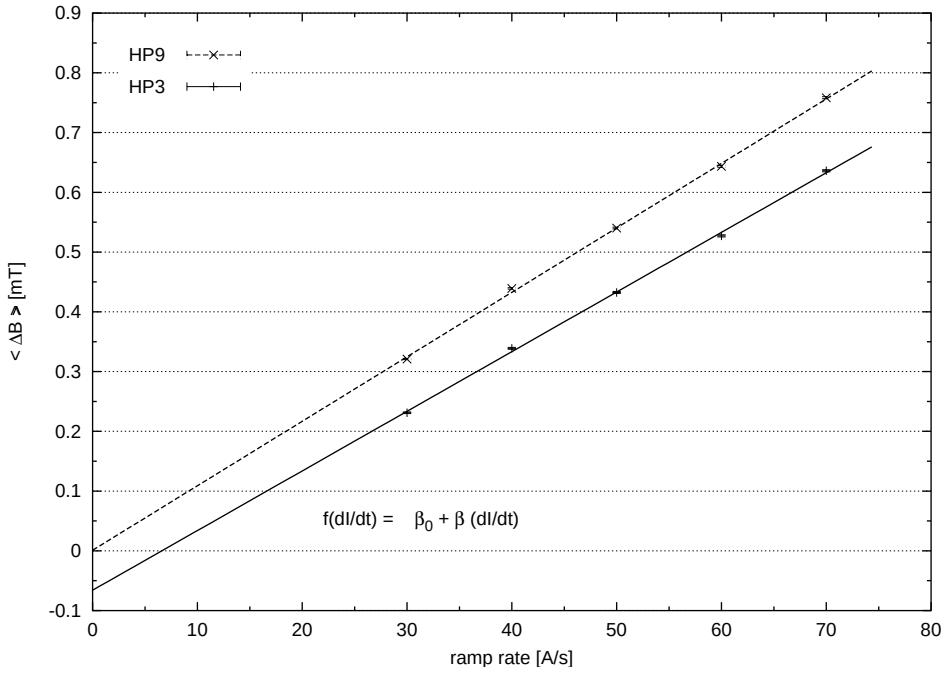

Figure 5.17: The linear dependence of the averaged ΔB-values on the ramp rate for magnet MBP2 O2. The corresponding standard deviation for each point is also plotted, but it is too small to be visible.

	Offset β_0 $[\mu T]$	Slope β $\left[\frac{\mu T}{(A/s)}\right]$
HP3	-97	10.03
HP9	-18	10.72

Table 5.12: The fit parameters deduced from Equation 5.22 for the example shown in Figure 5.17

Position	Offset β_0 $[\mu T]$	Slope β $\left[\frac{\mu T}{(A/s)}\right]$	R_c $[\mu\Omega]$
$0\,cm$	52	7.36	60
$3\,cm$	-37.8	6.64	66
$5.5\,cm$	-62.2	7.74	57
$8.5\,cm$	50.9	8.24	53
$11.5\,cm$	13.4	6.67	66
$14.5\,cm$	-49.6	6.66	66
$17\,cm$	-87.3	6.78	65
$20\,cm$	-18.2	7.33	60
$23\,cm$	14.7	8.13	54
$28.5\,cm$	-69.4	6.89	64
Average	-23.9 ± 44.6	7.24 ± 0.62	61 ± 5

Table 5.13: The fit parameters deduced from Equation 5.22 and the corresponding values for the cross–contact resistance on different positions along the magnet axis in the second aperture of the first pre–series LHC main diploe MBPS O01

As an example Table 5.13 gives the values for the offset β_0 and the slope β deduced from Equation 5.22 measured in the second aperture of the pre–series magnet MBPS O01 along the axis. The distances are referred to the first position which is set to be $0\,cm$. The corresponding values for the cross–contact resistance obtained from Equation 5.23 are listed in the last column of Table 5.13. The mean values with their standard deviations of the three parameters over all positions can be found in the last row.

The spread of the slope values β and also of R_c in dependence on the relative position along the magnet axis for the values given in Table 5.13 is shown in Figure 5.18. No clear periodicity can be observed. In contrary Figure 5.19 shows a similar periodicity as discussed in the previous section for the PFP. In this case the extrapolated values for $f\left(\dot{I} \to 0\right) = \beta_0$ are plotted again as a function of the distance for the above mentioned magnet. By using a sinusoidal fit function of the same type like Equation 5.5 an amplitude of $52.2\,\mu T$, an average value of $-32\,\mu T$ and a phase of $1.93\,rad$ can be obtained.

5.4 PFP amplitudes expected in series LHC dipoles

The summarized of the PFP and FA measurements first time performed together using the same technique are shown in Table 5.14. The amplitudes B_1 of the PFP deduced from Equation 5.5 and 5.17 respectively are given at time $t = 2500\,s$ after the beginning of the measurement. The investigated magnets were submitted to

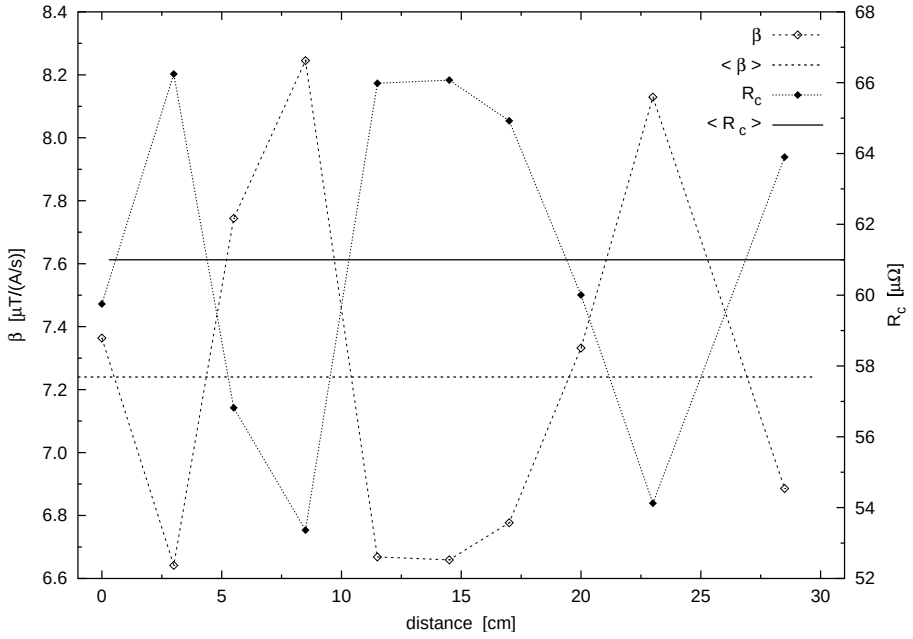

Figure 5.18: The spread of the slope β and the corresponding cross–contact resistances as a function of the distance. Additional the mean values are shown for both parameters.

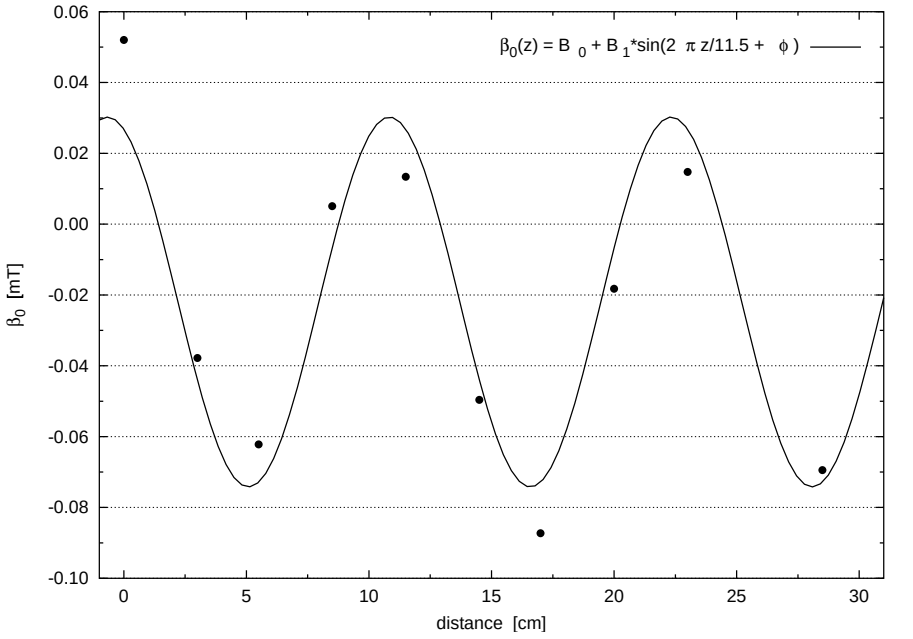

Figure 5.19: The values for β_0 shows a periodic dependence on the z-coordinate in the same way as already shown for the PFP.

a current reference cycle with a ramp–up to $9\,kA$ at $40\,A/s$ followed by a ramp–down at $-40\,A/s$ after a flat–top time of $1000\,s$.

The values of the cross–contact resistance R_c deduced from the FA measurements are listed in the last row of Table 5.14. These results allow to plot the dependence of the PFP amplitude as a function of $\frac{1}{R_c}$ (see Figure 5.20). As expected, the data can be fitted with a linear variation crossing the origin [67] resulting in

$$B_1\left(R_c^{-1}\right) = 8 \cdot R_c^{-1}\ . \tag{5.24}$$

The slope of this straight line allows to estimate the amplitude of the non–uniform current distribution in function of R_c.

For the series LHC dipoles the cross–contact resistances will to be controlled via the oxidation process. Thus a guaranty for the minimum value of R_c is provided to $20\,\mu\Omega$. Considering Equation 5.24 a PFP amplitude of about $0.41\,mT$ is calculated. From the other hand a maximum for the cross–contact resistances of about $100\,\mu\Omega$ is presently evaluated. For such a R_c value the PFP amplitude is calculated to $0.08\,mT$.

Magnet Name	PFP Amplitude $B_1\,(t = 2500\,s)$ $[mT]$	Cross–contact resistance R_c $[\mu\Omega]$
MBSMS17 . V3	2.27	[a]
MBSMT4 . V2	1.17	[a]
MBSMT4 . V5	1.15	[a]
MBSMT5 . V3	0.19	[a]
MBP 2O1	0.16	40 ± 2
MBP 2A2	0.13	70 ± 7
MBP 2O2	0.18	42 ± 2
MBPS O01	0.15	63 ± 2
MBPS A01	0.25	37 ± 2

[a] not measured

Table 5.14: Summary of the results obtained on LHC short diploes, full–scale prototypes and first pre–series dipoles

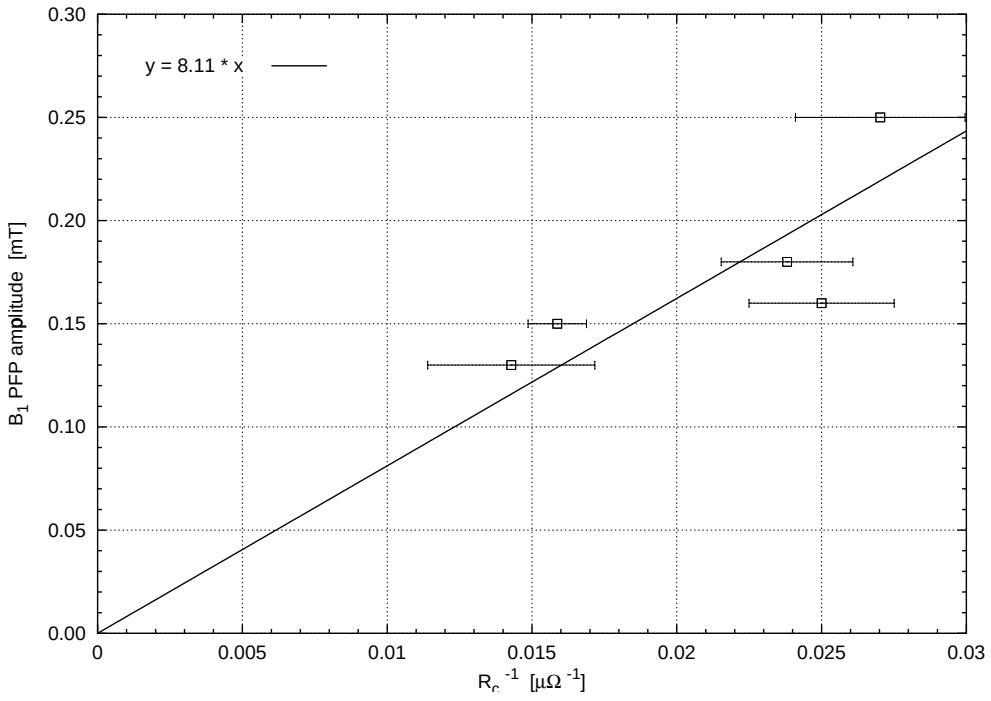

Figure 5.20: PFP amplitude obtained after a reference current cycle versus $\frac{1}{R_c}$ deduced from FA measurements.

Chapter 6

Impact on quench performance of LHC dipoles

6.1 Magnet quench

A quench is the transition of superconductor from the superconducting to the normal state. Such a transition will invariably occur if any of the three parameters temperature, magnetic field or current density of the superconductor exceeds a critical value. In fact the large scale superconducting magnets rarely can be excited up to the critical current of the conductor but quench at significantly lower values. This phenomenon is called premature quenching and the reason may be insufficient clamping of the windings or insufficient cooling. Because of the Lorentz forces a certain part of a winding can move slightly causing a temperature increase initiating a quench. If this part is, after the motion, in a stable position the magnet can be excited to a higher current in the next attempt. The second quench will than be caused by the motion of another part of the windings. Going on with this procedure the magnet can reach the critical current. Therefore the magnets can be "trained" for their use in the accelerator.

Like most large–scale magnets, the LHC main ring magnets exhibit training quenches. This type of premature quenches is mainly due to conductor motions or epoxy resin cracking. Both of these effects can lead to a local temperature rise exceeding the critical temperature of the superconducting state. The temperature margin for the LHC main dipoles in case of transient heat deposition (see Figure 6.1) is about $7\,K$ at injection field and about $1.4\,K$ at nominal field. The temperature margin for the continuous heat deposition is however reduced to about $0.26\,K$ at nominal field of $8.33\,T$ and nominal temperature of $1.9\,K$ [68].

Besides these training quenches the quenching field of the magnets depends also on other parameters as for example the applied ramp rate for exciting the magnet. Particularly during acceleration process, magnets are subject to a magnetic ramp cycle, wherein the magnetic field changes from zero to a maximum

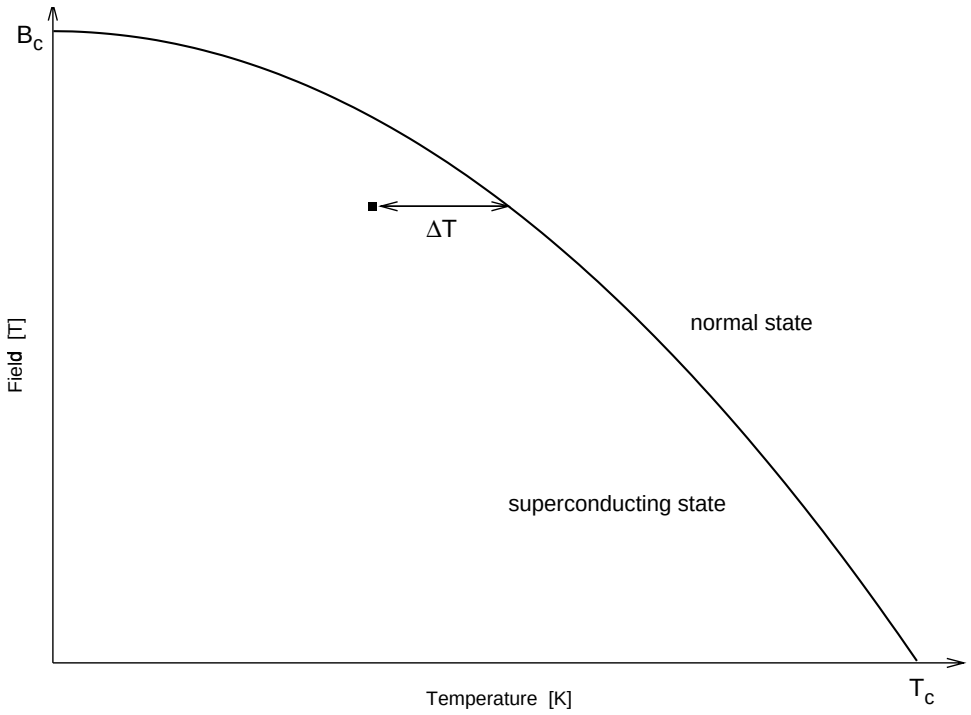

Figure 6.1: The critical field of a superconducting material as a function of the temperature. The temperature margin ΔT for the LHC magnets in case of transient heat deposition is about $1.4\,K$ at nominal field of $8.33\,T$.

value. In some cycles, the field may also be ramped down to zero field over a period of time. In both cases, the changing magnetic field produces voltages internal to the magnet in accordance to classical electromagnetic theory of induction. If low resistance paths exist in regions where changing magnetic fields occur, eddy currents will flow. These currents may degrade magnet performance in several ways. Since they result in response to a magnetic field ramp, magnet performance may be sensitive to the ramp rate.

6.2 Quench performance versus ramp rate

The LHC dipoles of full length and model magnets of reduced length have been systematically tested concerning the ramp rate limitation. Not only the quench current as a function of ramp rate, but also the quench location were measured. For this purpose pick up coils, also called Quench–Antenna (QA), were used [69] and [70]. Using the same technique signals occurring well before quenches can also be studied. The rapid variations recorded in voltages coming from QA called spikes can in general be interpreted as due to conductor motions or epoxy resin cracking. The localization and the time distribution of such precursors to the quench can give precious information concerning the mechanical stability of the

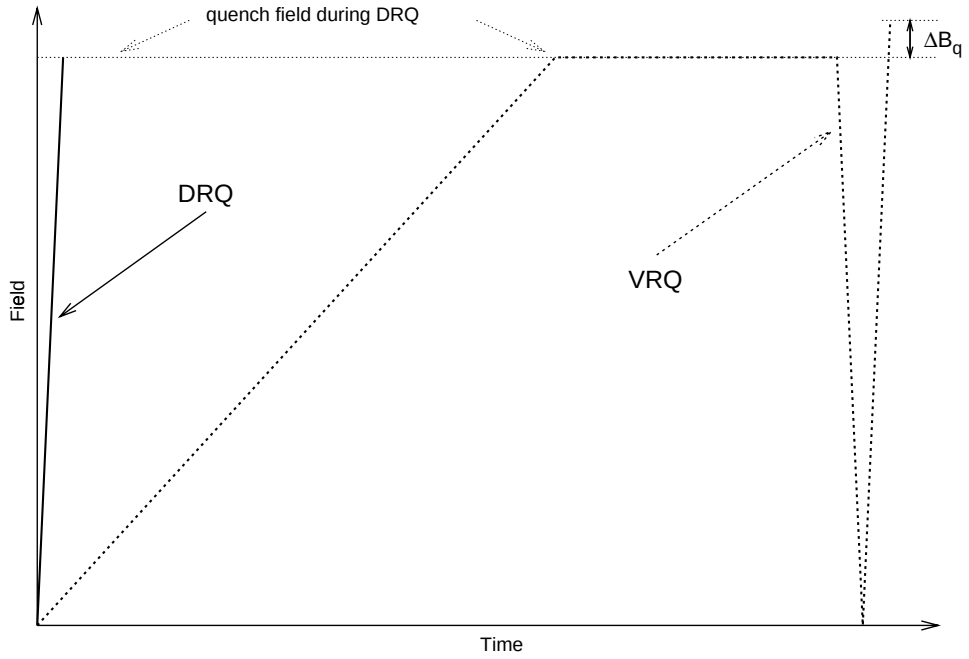

Figure 6.2: The two different ramps to quench, Direct Ramp to Quench (DRQ) and V-Ramp to Quench (VRQ), used for investigation of the quench behavior. The VRQ–cycle shows a magnetic field at quench, which is ΔB_q larger in comparison to the quench field during a DRQ at the same ramp rate.

coils [71].

For investigation of a ramp rate dependence on the quench behavior two special ramps to quench have been performed to distinguish between the magnet excitation histories. For the so–called Direct Ramp to Quench (DRQ) the field value is increased with a certain ramp rate from zero up to the magnetic field at quench (see continuous line in Figure 6.2).

In the second case the magnet is first ramped to a high field value corresponding to quench field during DRQ at a low ramp rate that does not cause the magnet to quench. The field is then held constant for about ten minutes. After the pause, the magnet is ramped–down to almost zero and is ramped–up again to quench at a defined ramp rate (see dashed line in Figure 6.2). As the last ramp–down and ramp–up cycle is symmetrical, i.e. at the same ramp rate, these cycles are referred to as V-Ramp to Quench (VRQ).

6.2.1 DRQ

During the testing period of each magnet several quenches are provoked by a direct ramp to quench. Figure 6.3 displays a summary plot of quench field versus

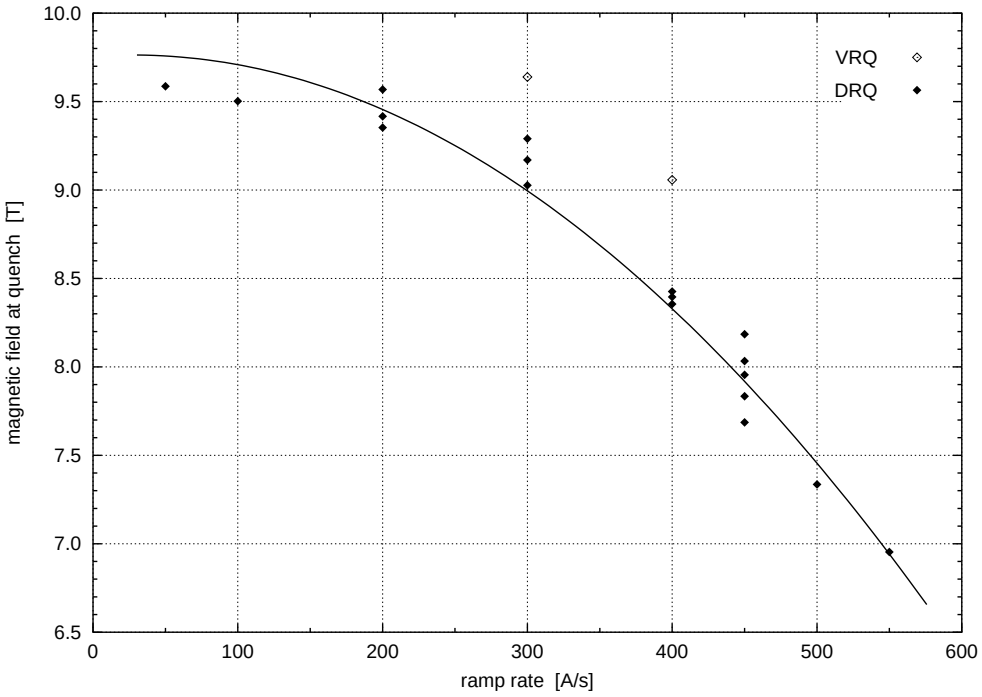

Figure 6.3: Quench characteristic as a function of the ramp rate. After a special ramp to quench the magnetic field at quench is increased, mainly because of the reduced eddy currents contribution.

ramp rate for the short model dipole MBSMT5.V3. The continuous line shows qualitatively the behavior of the quenching field by an increase of the ramp rate for DRQ measurements. The constant part at relatively low ramp rate can be explained by training quenches, i.e. the quenches originating in mechanical motions of a new magnet. The spread of the field values at the same ramp rate shows that the creation of a quench is a function of several parameters. Locally deficient cooling by definition reduces temperature margin, according to the temperature profile in the pressurized helium bath around the magnet.

The reduced quench field with increasing ramp rate can mainly be described by two phenomena, the heat dissipation which increases with ramp rates, and the effect of induced eddy currents discussed in the previous chapter. Since the effect of the heat dissipation is proportional to the square of the current sweep rate and additionally the reduction of the quenching field depends linearly on the ramp rate induced non–uniform current the resulting function shown as a continuous line in Figure 6.3 is the superposition of a parabolic and a linear term.

$$\begin{aligned} I_q &= I_c\left(T+\Delta T\right)-\Delta I \\ &\approx I_c\left(T\right)+\frac{\partial I_c}{\partial T}\Delta T-\Delta I \end{aligned} \tag{6.1}$$

The influence of the heat is nearly independent on the history how the magnet is

excited to its quench field. Whereas the PFP measurements dealing with different current cycle parameters have shown that the amplitude of induced eddy currents depend strongly on the magnet history. Thus, in principle, an estimation of the current sharing on the total field decrease for higher ramp rates can be performed by using special ramps to quench.

6.2.2 VRQ

The V-ramp to quench measurements are intended in order to determine if the dominant mechanism for the field reduction at higher ramp rates has its origin in the induced eddy currents. The V-ramp is comparable to the PFP measurements with symmetrical current cycles without any flat–top duration. From the measurements dealing with the current cycle parameters influencing the PFP characteristics, it was investigated that in the case of ramp rates differing only in the sign the induced current waves can partially cancel each other. Because of this reason it is expected that the influence of eddy currents after a VRQ is smaller compared to that one after a DRQ. Assuming that the contribution from the heat dissipation is the same for both types of ramp to quench (this is true for ramp rates up to about $500\,A/s$, the general case is $Q_{DRQ} \leq Q_{VRQ}$) this leads to higher values of the magnetic field at quench for VRQ measurements. Such measurements were only performed at two different ramp rates for the magnet MBSMT5.V3. Nevertheless an increase of the quench field can be clearly investigated in comparison to the DRQ measurements (see Figure 6.3).

6.2.3 Interpretation and comparison of the ΔB_q values

The difference between the quench field reached after a VRQ and that one reached after a DRQ is referred here to as ΔB_q. These values, for example, can be seen in Figure 6.3 as the distance between the black and the white icons at constant ramp rate. A summary of these ΔB_q values performed on the two short model magnets MBSMT4 and MBSMT5 for several ramp rates is given in Table 6.1. In Figure 6.4 this behavior is illustrated. The data points are approximated by a parabolic function

$$\Delta B_q\left(\dot{I}\right) = q \cdot \dot{I}^2 \tag{6.2}$$

within the assumption that the effect should vanish for zero ramp rate. The coefficients for q of both magnets are given in Table 6.2.

As the ΔB_q values are an indication for the size of the induced eddy currents a similar behavior of these values in respect of different magnets is expected such as already observed on PFP measurements. A qualitative comparison of these two estimations on the eddy currents shows consistent results. The PFP measurements have pointed out that for example the PFP amplitude B_1 measured

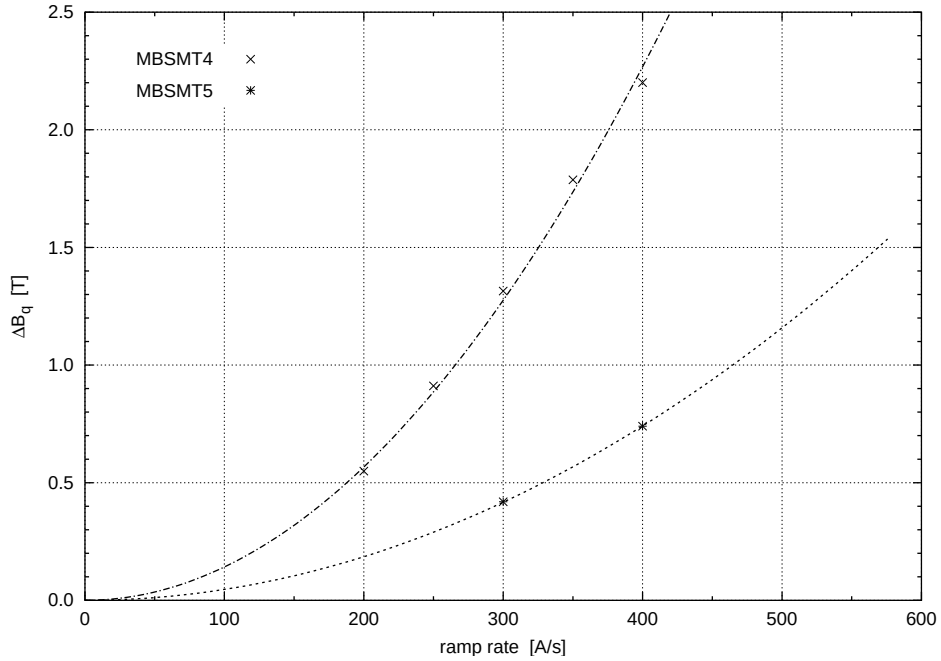

Figure 6.4: Graphical illustration of the values given in Table 6.1 approximated by Equation 6.2.

Ramp rate	MBSMT4	MBSMT5
$200\,A/s$	0.549	[a]
$250\,A/s$	0.911	[a]
$300\,A/s$	1.314	0.419
$350\,A/s$	1.787	[a]
$400\,A/s$	2.2	0.74

[a] not measured

Table 6.1: The ΔB_q values representing the difference between the VRQ and the DRQ measurements at the same ramp rate for the two short model magnets MBSMT4 and MBSMT5

	MBSMT4	MBSMT5	ratio
$q\ \left[mT\,(A/s)^{-2}\right]$	$1.42 \cdot 10^{-5}$	$4.63 \cdot 10^{-6}$	3.06
$B_1\ [mT]$ from PFP	2.55	0.67	3.81

Table 6.2: Relative influence of the eddy current estimated by two kinds of measurement for the same magnets

on the short model magnet MBSMT5 is roughly a factor 3.8 smaller compared to the similar magnet labelled MBSMT4. The ratio of the ΔB_q values for these two magnets leads to a factor of 3 which is close to that one estimated above. Table 6.2 shows this result in a more detailed way for the two mentioned magnets.

Equation 6.2 and the evaluated values for q presented in Table 6.2 allows to perform an extrapolation for the eddy current impact on the quench performance for ramp rates, which will be used for the LHC accelerator running. Considering a ramp rate of $40\,A/s$ used for the PFP measurements the contribution of the induced eddy currents is calculated to $22\,mT$ in the case of magnet MBSMT4 where a larger value for q was obtained. With the transfer function which is equal to $0.7\,T/kA$ for this twin aperture short model magnet the corresponding current value is $32\,A$.

6.3 Effect of the PFP on the quench performance

In the case of low ramp rates, i.e. up to $10\,A/s$, the non–uniform currents represent the main part of the whole eddy currents. These non–uniform interstrand current distribution inside the superconducting cable of the coil is responsible for the effect of the PFP. In order to understand the origin of such non–uniformity, previous studies have identified two main mechanisms. The first one concerns the spatial variation of the time derivative of the magnetic field along the cable. The second one is related to the variation of the cross–contact resistance between the strands of the cable.

An estimate of the current imbalance between the strands required to produce the maximum PFP amplitude $B_1\,(t_1) = 32\,mT$ measured during this study is around $\pm 350\,A$ for the case of short dipole models investigated (i.e. with 6-block coil structure). This value is not negligible and should be compared to the current margin at the nominal field of half of the cable which is around $1000\,A$. Moreover for the real operation of the LHC machine such a margin will be drastically reduced due to the beam loss. As a consequence, non–uniform superimposed induced currents can certainly provoke premature quenches of the dipoles.

The full–scale prototypes and pre–series dipoles measured have shown a much smaller value for the PFP amplitude. Additionally a linear correlation between the PFP amplitude and the inverse cross–contact resistance was found. The oxidation process of the strand coating developed at CERN for the superconducting cables for the LHC is expected to guaranty a minimum value for R_c equal to $20\,\mu\Omega$ [72]. This is actually the case as it can be noticed in Table 5.14 for the R_c values deduced from measurements performed on prototypes and first pre–series dipoles. According to the linear fit of Figure 5.20, a R_c value of $20\,\mu\Omega$ corresponds

to an amplitude for the PFP equal to $0.41\,mT$.

The study of the PFP performed on short models gives typically a factor around 5 between the amplitudes of the PFP taken at the time t_1 (on the flat–top of the cycle) and t_3 (right after the cycle is finished) of the current cycle up to the nominal value. As a consequence, for LHC dipole magnets with the lowest cross–contact resistance expected, the PFP amplitude can reach $2\,mT$ at the nominal field. An estimate of the current imbalance between strands required to produce such a PFP amplitude is around $\pm 22\,A$. This estimation resulting from the PFP studies is comparable with the value obtained for all induced eddy currents using the ramp to quench measurements described above which is equal to $32\,A$.

Because these values are small in comparison to the current margin of $1000\,A$, it can be said that non–uniform superimposed induced currents however contribute to the origin of the premature quenches of the dipoles with the lowest R_c values but their impact on quench performance is much less critical than anticipated from the worst case obtained with short dipole models.

Chapter 7

Conclusion

Current distribution in superconducting cables is known to have effects on several aspects of quench performance, and mainly on the quench characteristics and field quality. Non–uniform current distribution has already been observed in earlier measurements experimentally both in dedicated small–scale experiments, as well as in full–scale magnets. Within the Large Hadron Collider (LHC) project, we are concerned mainly with the performances of the superconducting magnets that will form the main ring. The non–uniform superimposed induced currents reduce locally the difference between the total strand current and the critical current of the superconductor. This may provoke premature quenches of the dipoles and can affect the stability with respect to quench performance.

The thesis was planed to measure the current distribution inside the Rutherford–type superconducting cables, and to establish the nature of the current distribution changes and a correlation to cable properties. In addition the effect of the current distribution and its evolution should be examined in relation with the long term stability of the field and quench properties with the aim to provide a predictive tool for the operation of the LHC.

For this purpose a detailed study on the Periodic Field Pattern (PFP), which occurs along the magnet axis resulting from the induced current distribution, was launched and accomplished in the present thesis. The experimental approach to the investigation of the PFP has been carried out with six short magnet models and has also been extended on full–scale LHC prototypes and pre–series magnets. In general the behavior of the PFP parameters, especially the amplitude of the sinusoidal like oscillations, was investigated as a function of the current precycle parameters and the influence of the magnets characteristic on the PFP was also studied.

It was found that during the ramp–up of the current cycle the Rutherford–type superconducting cable charges itself with a non–uniformly distributed current wave. On the plateau of the cycle this current wave diffuses slowly, in other words the current tends to be shared more uniformly between the strands. During the ramp–down, the superconducting cable charges itself with a non–uniformly

distributed current wave of an opposite sign as compared to the current ramp–up (antiwave). As a consequence, the PFP measured after the current cycle is the composition of two waves which can partially cancel. For the influence of the current cycle parameters it can be concluded that the PFP amplitude increase

- for an asymmetrical cycle, i.e. two different ramp rates for up and down,
- with the duration of the flat–top time (smallest PFP amplitude after a triangle–like form of the current cycle)
- with the top–current of the cycle including a longer charging and discharging period at constant ramp rate.

In other words the induced unbalanced currents can be kept small if the magnet is excited after a precycle which is symmetrical in the ramp rates, has no flat–top duration at all and has a relative small top–current.

The data treatment in respect of the dynamic behavior of the PFP amplitude has pointed out a weakness of the used two–strand theoretical model which is for the static point of view in quite good agreement with the experimental results. This indicates that the origin of the induced current distributions depends on local characteristics, e.g. the field sweep rate and the cross–contact resistance R_c. One of the major results in this section is the first known observation of a PFP during a time period of up to 81 hours at zero transport current after the magnet was excited with a defined current cycle. This leads to a quasi–static current distribution inside a resistive network.

The study of the PFP inside different short and long magnets was performed with the so–called current reference cycle with a ramp–up to $9\,kA$ at $40\,A/s$ followed by a ramp–down at $-40\,A/s$ after a flat–top duration of $1000\,s$. The first conclusion which can be drawn is that no clear distinction can be observed between the PFP amplitudes measured in long and short dipoles. In addition the largest spread in the PFP amplitudes is observed inside the short dipole models whereas all results obtained in long dipoles are very close. Since one of the main parameters of a Rutherford–type superconducting cable is the cross–contact resistance, the so–called Field Advance (FA) produced by eddy current was measured for long dipoles during current cycles optimized for this study, which allows to determine the cross–contact resistance. In this thesis the PFP and the FA were measured for the first time together using the same technique. This allowed to correlate both these parameters in reliable way. The results for the PFPs considering measurements on different magnets have shown that the spread is rather small if the cross–contact resistance is reproducible. This implies that all the strands and cables have to be produced, stored and processed by identical and well–controlled methods. Furthermore, also the prestress and the curing cycle have to be the same for all magnets. For the recent magnets

this has been achieved by the oxidation process of the strand coating developed at CERN.

From the experimentally observed linear correlation between the PFP amplitude and the inverse cross–contact resistance an amplitude for the PFP equal to $0.41\,mT$ is calculated for a guaranteed minimum value for R_c equal to $20\,\mu\Omega$ for the superconducting cables for the LHC. Considering all results obtained in this study a PFP amplitude of $2\,mT$ at nominal field for LHC magnets with the lowest cross–contact resistance is assessed. A worst case estimate of the current imbalance between the strands required to produce such a PFP amplitude is around $\pm 22\,A$ for the case of the LHC dipole final design. This value should be compared to the current margin at the nominal field of half the cable which is around $1000\,A$. Moreover for the real operation of the LHC machine such a margin will be drastically reduced due to beam losses. As a consequence, non–uniform superimposed induced currents may provoke premature quenches of the dipoles with the lowest R_c values but the instability with respect to quench performance provoked by PFP is much less critical than anticipated from the worst case obtained with short models.

This study performed on LHC superconducting dipoles of two different scales has verified and confirmed appropriate results of the oxidation process developed for the LHC main lattice magnets in order to control effects like non–uniform current distribution and resulting PFP. The worst case estimate of the PFP is such that it can still affect to certain extent the stability of LHC main dipoles with respect to quench performance. This problem would have been more serious if the cross–contact resistance between strands had not been controlled.

Appendix A

Field advance, Python source

The aim of the field advance measurements series is to investigate the magnetic field difference of the ramp–up and the ramp–down in a specified current cycle in dependence of the ramp–rate. For this case current cycles with the same flat–top current and flat–top time but with different ramp–rates were performed. For each measurement the ramp rate for up and down was equal, i.e. a symmetrical cycle.

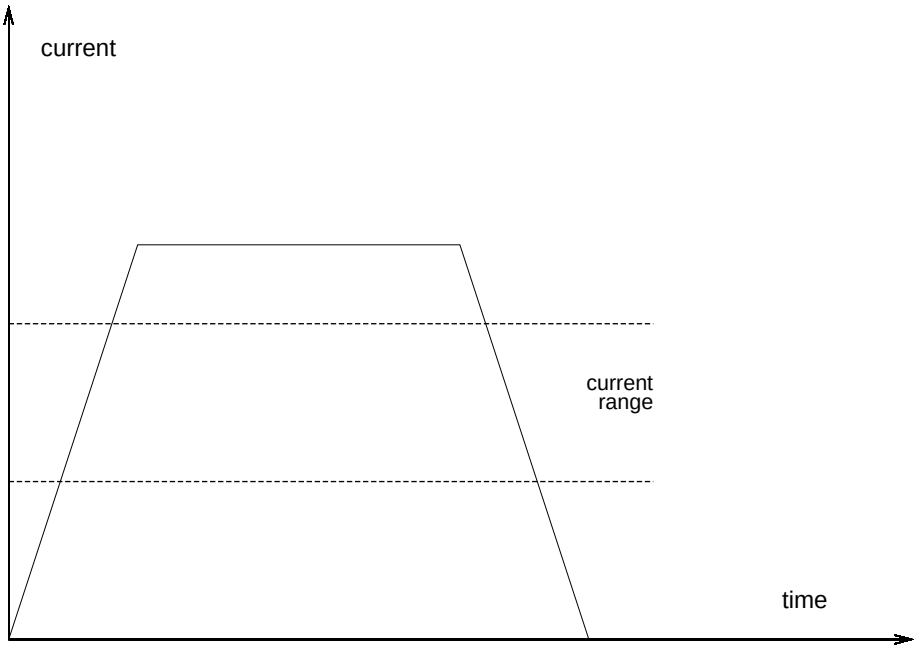

Figure A.1: Example for the used current cycles with fixed ramp–rate.

A certain number of Hall–probes in a special equipped device was used to measure the magnetic field during the cycle. The date were recorded with the help of six KEITHLEY 2001 digital multimeters. Therefore it was possible to get all the interesting values at the same time. Finally a raw data file with a specified

header including the measurement environment informations and six channels of recorded data was produced. In the first channel the magnet current of the whole cycle was stored. The corresponding voltage values of the Hall–probes can be found in the other ones.

The goal of the below described Python–source is to calculate for each measurement and each Hall–probe an average value of the field difference in the up and down ramp of the current cycle and the corresponding standard deviation in a certain current range. In other words the magnetic field values for the up and down ramp are compared for the same current values.

After the read–in of the raw date file the current cycle is splitted between the up and the down current range. This is achieved by searching for the maximum and minimum current value. With this information the user can choose a current range between these two values. Of course there is a check if the range is sensible, i.e. the two current input values must fit inside the real maximum and minimum and also the current must be monotonous for the ramp up and the ramp down respectively. Because we want to compare the voltage values for exactly the same current of the two ramps an interpolation between every two points of the ramp down is performed. With the help of this interpolation the voltage values of the ramp down can be estimated for the measured current values of the ramp up. Afterwards the difference in voltage is calculated for the selected current range. Finally the average of all this differences and the corresponding standard deviations are computed. The results for the substraction in dependency of the current, as well as the mean values and some other measurement and calculation parameters are written into two new files with the file–extensions *.adv* and monotonous *.result*, respectively.

Basis.py

```
#!/usr/bin/env Python

NotImplemented='NotImplemented'
UnknownChannel = 'UnknownChannel'
#--------------------------------------------------------------------
class Data:
   """
   Generic class encapulating channel data.

   In the derived classes the __init__ function must set self.channel_max.
   channelnames must be set!
   Further the private method _getData must be Implemented!
   """
    def getCurrent(self):
        "Returns the Current in the Magnet"
```

```
        return self._getData(0)

    def getChannel(self, channel):
        "Returns the Data of the Channel"
        if channel < 1 or channel > self.channel_max:
            errm = "The Channel you specified does not exist!" +\
                   " Max Channels : " + str(self.channel_max) +\
                   " You specified : " + str(channel)
            raise UnknownChannel, errm
        return self._getData(channel)

    def getChannelNames(self):
        return self.channelnames

    def setChannelNames(self, names):
        self.channelnames = names

    def getNumberOfChannels(self):
        return self.channel_max

    def _getData(self, channel):
        "Virutal 'private' method to be used by the derived classes"
        raise NotImplemented, "This function is a virtual function" +\
              "and must be implemented in the derived class!"
#-----------------------------------------------------------------------
```

RawData.py

```
#!/usr/bin/env python

import Numeric
import string
import copy

import Basis
FileReadError = 'FileReadError'

class RawFile(Basis.Data):
    def _getData(self, index):
        return self.array[:,index]

    def getGains(self):
        return self.gains

    def getTime(self):
```

```
        return self.datetime

    def getMagnetName(self):
        return self.magnetname

    def getRampRate(self):
        return self.ramprate

    def getIntegrationTime(self):
        return self.integrationtime

class ReadRawFile(RawFile):
    def __init__(self, filename):
        self.file = open(filename, 'r')
        self.datetime        = self._readHeaderInfoLine('Date&Time')
        self.magnetname      = self._readHeaderInfoLine('MagnetName')
        self.integrationtime = self._readHeaderInfoLine('IntegrationTime')
        self.ramprate        = self._readHeaderInfoLine('RampRate')

        self.channelnames    = self._readHeaderInfo('ChannelNames')
        self.gains           = self._readHeaderInfoFloat('Gains')

        while 1:
            line = self.file.readline()
            if line[:4] == 'Data':
                break
            elif line == '':
                raise FileReadError, "I didn't find a data statetment!"

        hlplist = []
        for line in self.file.readlines():
            hlp = string.split(line)
            if hlp != []:
                hlp = Numeric.array(map(float, hlp))
                hlplist.append(hlp)

        if len(hlplist) == 0:
            raise FileReadError, "I could not find any Data after" +\
                                 "the Data statement!"

        self.array = Numeric.array(hlplist)
        self.channel_max = self.array.shape[1] - 1

        #Look if there were enough channelnames and gains!
        hlp = len(self.channelnames) - 1
```

```
        if  hlp != self.channel_max:
            raise FileReadError, "I could not find as many channelnames" +\
                  "as channels! I found " + str(hlp) + " channelnames," +\
                  "but I found " str(self.channel_max) + " Channels!"

        hlp = len(self.gains) - 1
        if  hlp != self.channel_max:
            raise FileReadError, "I could not find as many channelnames" +\
                  "as gains!" I found " + str(hlp) + " gains," +\
                  "but I found " str(self.channel_max) + " Channels!"

    def _readHeaderInfoFloat(self, info):
        hlp = self._readHeaderInfo(info)
        return map(float, hlp)

    def _readHeaderInfoLine(self, info):
        while 1:
            line = self.file.readline()
            hlp = info
            l = len(hlp)
            if line[:l] == hlp:
                break
            elif line == '':
                raise FileReadError, "I didn't find a " + info + " statetment!"
        return line

    def _readHeaderInfo(self, info):
        while 1:
            line = self.file.readline()
            hlp = info
            l = len(hlp)
            if line[:l] == hlp:
                break
            elif line == '':
                raise FileReadError, "I didn't find a  " + info + " statetment!"
        line = self.file.readline()
        return string.split(line)


def test():
    t = ReadRawFile('SM18-A2-30-11-2000-14-56-34.tsf')
    print t.getChannelNames()
    print t.getGains()
    return t
```

```
if __name__ == '__main__':
    test()
```

UserInput.py

```
#!/usr/bin/env python
import sys

OutofRange = 'OutofRange'

class UserInput:
    """
    Virtual Class encapsulating Range Input of the User!
    """
    def __init__(self, what, dim):
        self.what = what
        self.dim  = dim

    def getUserMin(self):
        return self.usermin

    def getUserMax(self):
        return self.usermax

    def getRealMin(self):
        return self.realmin

    def getRealMax(self):
        return self.realmax

    def getRange(self, min, max):
        self.realmin = min
        self.realmax = max
        usermin, usermax =  self._getRange(min, max)
        if usermin < min:
            raise OutofRange, "Minimum is smaller than the allowed range!"
        if usermax > max:
            errm = "Maximum is bigger  than the allowed range!\n" +\
                   "Realmax = " + str(max) + "\nYou specified = " +\
                   str(usermax)
            raise OutofRange, errm
        return usermin, usermax

class InitInput(UserInput):
```

```
        def __init__(self, mymin, mymax):
            self.usermin = float(mymin)
            self.usermax = float(mymax)

        def _getRange(self, *notused):
            return self.usermin, self.usermax



class Keyboard(UserInput):
    def _readInRange(self):
        while 1:
            myinput = raw_input()
            try:
                hlp = float(myinput)
            except ValueError, des:
                print "you gave me an illegal string: -->", myinput, "<--!"
                print "Which I can't convert to float!"
                print "err :", des
                sys.stdout.write("Please give a new string! > ")
                continue

            if hlp < self.min:
                print "The Value  ", hlp, ", you specified is smaller",
                print "than the minimum", self.min, " !"
                sys.stdout.write("Please give the value again! > ")
                continue

            elif hlp > self.max:
                print "The Value  ", hlp, ", you specified is bigger than",
                print "the maximum", self.max, " !"
                sys.stdout.write("Please give the value again! > ")
                continue
            else:
                break
        return hlp

    def _getRange(self, min, max):
        self.min = min
        self.max = max
        hlp = " [" +  self.dim + "]"
        print "\n"
        print "Specify ",
        print self.what, hlp,
        print " : "
```

```
        while 1:
            print "Minimum is:", "%6.3f" % self.min, " ", hlp
            print "Maximum is:", "%6.3f" % self.max, " ", hlp
            sys.stdout.write("Specifiy Minimum: " + hlp +  "> ")
            min = self._readInRange()
            sys.stdout.write("Specifiy Maximum: " + hlp +  "> ")
            max = self._readInRange()

            if min > max:
                print "Min must be smaller than max!!"
                continue
            else:
                break

        self.usermin = min
        self.usermax = max
        return min, max

def keyboardtest():
    k = Keyboard(0, 1, "Current", "kA")
    k.askUser()
    return k

def test():
    k =  keyboardtest()
    print "Min = ", k.getUserMin()
    print "Max = ", k.getUserMax()


if __name__ == '__main__':
    test()
```

Calc.py

```
#!/usr/bin/env python

import Numeric
from   Scientific.Functions.Interpolation import InterpolatingFunction
from   Scientific.Statistics import mean, standardDeviation


from   RawData   import ReadRawFile
from   UserInput import Keyboard, UserInput, InitInput
```

```
#from   watch     import watch
from   Utils     import ClearNaN
import Basis
UnknownChannel= Basis.UnknownChannel


SplitNotFound = 'SplitNotFound'
NonMonotonRamp= 'NonMonotonRamp'
InterpolBug   = 'InterpolBug'
__eps = '1e-14'

#--------------------------------------------------------------------------
class CalcData(Basis.Data):
    def __init__(self, channellist):
        self.channellist  = channellist
        self.channelnames = None
        self.channel_max   = len(channellist) - 1

    def _getData(self, index):
        return self.channellist[index]

    def getChannelInterpol(self, channel):
        """Creates a Interpolationobject, with the current as the
           independent and the data as the dependent variable.
        """
        current = self.getCurrent()
        data    = self.getChannel(channel)
        index = Numeric.argsort(current)
        hlpc  = Numeric.take(current, index)
        hlpd  = Numeric.take(data, index)
        return InterpolatingFunction((hlpc,), hlpd)

    def write(self, file):
        array = Numeric.transpose(Numeric.array(self.channellist))
        file.write('# ')
        if self.channelnames != None:
            for name in self.channelnames:
                file.write(name + '\t ')
            file.write('\n')
        if len(array.shape) == 1:
            array = array[:, Numeric.NewAxis]
        for line in array:
            for element in line:
                #file.write(`element` + '\t ')
                file.write('%e' % element + '\t ')
```

```
            file.write('\n')

#-------------------------------------------------------------------------
def fieldadvance(up, down):

    current = up.getCurrent()

    advancelist = [current]
    for index in range(1, up.getNumberOfChannels()+1):
        myf = down.getChannelInterpol(index)
        l = []
        for value in current:
            try:
                hlp = myf(value)
            except ValueError, des:
                #The current value was outside the interpolation!
                hlp = float('NaN')
            l.append(hlp)
        downdata = Numeric.array(l)
        data     = up.getChannel(index)
        advance  = data - downdata
        index    = index + 1
        advancelist.append(advance)
    advancedata = CalcData(advancelist)
    advancedata.setChannelNames(up.getChannelNames())
    return advancedata

def fieldadvancemean(advancedata):
    m = [None]
    s = [None]
    channelnames = advancedata.getChannelNames()
    for counter in range(1, advancedata.getNumberOfChannels()+1):
        data = advancedata.getChannel(counter)
        data = ClearNaN(data)
        if data == None:
            print "While trying to calculate the Statistic for the",
            print " FieldAdvance: "
            print " There was no fieldadvancedata for Channel Number ",
            print " ", counter, "named ", channelnames[counter]
            m.append(mean(float('NaN')))
            s.append(standardDeviation(float('NaN')))
        else:
            m.append(mean(data))
            s.append(standardDeviation(data))
```

```
    md = CalcData(m)
    md.setChannelNames(advancedata.getChannelNames())

    sd = CalcData(s)
    sd.setChannelNames(advancedata.getChannelNames())
    return md, sd

#-----------------------------------------------------------------------
def checkrampup(data):
    check = data[0]
    for item in data[1:]:
        if check > item:
            errm = "At item: " + str(item)
            raise NonMonotonRamp, errm
        else:
            check = item

def checkrampdown(data):
    check = data[0]
    for item in data[1:]:
        if check < item:
            errm = "At item: " + str(item)
            raise NonMonotonRamp, errm
        else:
            check = item


def validatedata(updata, downdata):
    hlp = updata.getCurrent()
    checkrampup(hlp)
    hlp = downdata.getCurrent()
    checkrampdown(hlp)

#-----------------------------------------------------------------------
def split(indexdata, data, max):
    # search for the beginning of the ones again
    l = len(indexdata)
    for index in range(l):
        item = indexdata[index]
        if item == 0:
            hlp = data[index]
            if hlp > max:
                break

    if index >= l:
```

```
        errm = "I could not find an index to split in the " + \
               "whole cycle!"
        raise SplitNotFound, errm
    return index

def checksplitlength(splitdata):
    if splitdata.shape == (0,):
        errm = "After splitting data, I had no data to calculate on!" +\
               " I can't continue without data!"
        raise SplitNotFound, errm

def splitdata(data, index, splitup, splitdown):
    hlpup    = Numeric.logical_and(index, splitup)
    hlpdown  = Numeric.logical_and(index, splitdown)
    datadown = Numeric.compress(hlpdown, data)
    dataup   = Numeric.compress(hlpup, data)
    checksplitlength(datadown)
    checksplitlength(dataup)
    return dataup, datadown

#--------------------------------------------------------------------
def get_min_max_current(rawdata):
    gain    = rawdata.getGains()[0] * 1000.0
    current = rawdata.getCurrent() / gain

    min     = current[Numeric.argmin(current)]
    max     = current[Numeric.argmax(current)]
    return min, max

#--------------------------------------------------------------------

def scale_and_split_cycle(rawdata, userinput):

    #Calculate Current in kA
    gain    = rawdata.getGains()[0] * 1000.0
    current = rawdata.getCurrent() / gain

    min     = current[Numeric.argmin(current)]
    max     = current[Numeric.argmax(current)]
    usermin, usermax = userinput.getRange(min, max)

    index = Numeric.logical_and(Numeric.less(usermin, current),
                                Numeric.greater(usermax, current))
    splitindex = split(index, current, usermax)
```

```
    indexrange = Numeric.arange(current.shape[0])
    splitup   = Numeric.less(indexrange, splitindex)
    splitdown = Numeric.greater(indexrange, splitindex)

    data = splitdata(current, index, splitup, splitdown)
    uplist = [data[0]]
    downlist = [data[1]]
    counter = 1

    for counter in range(1, rawdata.getNumberOfChannels()+1):
        hlp   = rawdata.getChannel(counter)
        counter = counter + 1
        data  = splitdata(hlp, index, splitup, splitdown)
        uplist.append(data[0])
        downlist.append(data[1])

    updata   = CalcData(uplist)
    downdata = CalcData(downlist)

    channelnames = rawdata.getChannelNames()
    updata.setChannelNames(channelnames)
    downdata.setChannelNames(channelnames)
    return updata, downdata

#---------------------------------------------------------------------
def readin():
    t  = ReadRawFile('SM18-A2-30-11-2000-14-56-34.tsf')

    return t, ui

def test():
    data, ui = readin()
    updata, downdata = scale_and_split_cycle(data, ui)
    validatedata(updata, downdata)
    updata.write(open('up.txt', 'w'))
    updata.write(open('up.txt', 'w'))
    downdata.write(open('down.txt', 'w'))
    hlp = fieldadvance(updata, downdata)
    fieldadvancemean(hlp)
    hlp.write(open('advance.txt', 'w'))

    return hlp

if __name__ == '__main__' :
    test()
```

FieldAdvance.py

```
#!/usr/bin/env python
"""
Author : Thomas Schreiner <Thomas.Schreiner@cern.ch>
Date   : 18.12.02000
Purpose: Caluclates the Fieldadvance
License: If non from CERN applies, GPL
"""

import sys
import getopt
import os
import string

import UserInput
import RawData
import Calc

#---------------------------------------------------------------------
class FieldAdvance:

    def __init__(self):
        pass


    def WriteResultFile(self, filename, mean, stdev, ui, rawdata):
        file = open(filename, "w")
        file.write("Measurement Information\n")
        for i in (rawdata.getTime,
                  rawdata.getMagnetName,
                  rawdata.getIntegrationTime,
                  rawdata.getRampRate,):
            file.write(" " + i())
        file.write("\n-------------------------------------------------\n")

        file.write("\nCurrent [kA]\n")
        file.write(" Real Values\n")
        file.write("    min :\t ")
        file.write(str(ui.getRealMin()))
        file.write("\n")
        file.write("    max :\t ")
        file.write(str(ui.getRealMax()))
```

```
    file.write("\n")

    file.write("Input Values\n")
    file.write("    min :\t ")
    file.write(str(ui.getUserMin()))
    file.write("\n")
    file.write("    max :\t ")
    file.write(str(ui.getUserMax()))
    file.write("\n")
    file.write("\n-------------------------------------------------\n")
    file.write("\nField Advance [V]\n")
    channelnames = mean.getChannelNames()
    for i in range(1, mean.getNumberOfChannels() + 1):
        file.write(" " + channelnames[i] + "\n")
        file.write("    Mean  :\t " + "%e" % mean.getChannel(i) + "\n")
        file.write("    Stdev :\t " + "%e" % stdev.getChannel(i) + "\n")

    print "\nField advance summary in"
    print "file ", filename," \nIn directory: ",  os.getcwd()
    print ""


def _WriteChannel(self, file, des, strlist):
    file.write(des + "\t ")
    hlp  = string.join(strlist, "\t ") + "\n"
    file.write(hlp)


def handlefile(self, ui, filename):
    try:
        data = RawData.ReadRawFile(filename)
    except RawData.FileReadError, des:
        print  "While trying to read in file " +\
              filename + " the following error occured: " + des
        return

    updata, downdata = Calc.scale_and_split_cycle(data, ui)
    Calc.validatedata(updata, downdata)
    advancedata       = Calc.fieldadvance(updata, downdata)
    mean, stdev = Calc.fieldadvancemean(advancedata)
    hlp = filename + ".adv"
    file = open(hlp, "w")
    advancedata.write(file)
    del file
```

```
        print "\nField advance in dependence of current in"
        print "file ", hlp," \nIn directory: ",  os.getcwd()
        print ""
        self.WriteResultFile(filename + ".result", mean, stdev, ui, data)
        return 1

    #--------------------------------------------------------------------
    def usage(self):
        print "Usage: ", sys.argv[0], " options measurementfiles"
        print "          --min: Minimum"
        print "          --max: Maximum"
        print "          -h : Print this Message"
        sys.exit(1)
    #--------------------------------------------------------------------
    def run(self):
        "If run as a CommandLineProgramm!"
        min = None
        max = None

        try:
            opts = getopt.getopt(sys.argv[1:], "-h", ("min=", "max="))

        except getopt.error:
            self.usage()

        measurementfiles = opts[1]
        for i in opts[0]:
            opt = i[0]

            if opt == '-h':
                self.usage()

            elif opt == '--min':
                min = float(i[1])

            elif opt == '--max':
                max = float(i[1])

        if len(measurementfiles) == 0:
            print "You didn't specify any measurementfile I should work on!!"
            self.usage()

        if min != None:
            if max == None:
                print " You only specified a minimum and no maximum!"
```

```
                print " I don't know what to do!!\n"
                return None
        if max != None:
            if min == None:
                print " You only specified a maximum and no minimum!"
                print " I don't know what to do!!\n"
                return None

        if min != None and max != None:
            ui = UserInput.InitInput(min,max)
        else:
            ui = UserInput.Keyboard("current", "kA")

        for file in measurementfiles:
            if self.handlefile(ui, file) != None:
                file = open(file + '.result' ,'r')
                for line in file.readlines():
                    sys.stdout.write(line)

def run():
    f = FieldAdvance()
    f.run()

if __name__ == '__main__':
    run()
```

Utils.py

```
import Numeric
#---------------------------------------------------------------------
def _aNumber(x):
    """
    A hack to find NaN in imput stream!
    For some reason a simple test of == float('NaN')
    does not work!!
    """
    if x > float('-Inf') and x < float('Inf'):
        return 1
    else:
        return 0

#---------------------------------------------------------------------
def ClearNaN(data):
    indexlist = []
```

```
    index = Numeric.array(map(_aNumber, data))
    index = Numeric.array(index)
    data = Numeric.compress(index, data)
    return data
```

Bibliography

[1] LHC–homepage, http://lhc.web.cern.ch/lhc/general/gen_info.htm

[2] CERN–homepage of the PS (Proton Synchrotron) Division, R. Ley, 1996, http://cern.web.cern.ch/CERN/Divisions/PS/PSComplex/CERNAcc.html

[3] E.J.N. Wilson, "Introduction to particle accelerators", CERN lecture series 1999/2000

[4] R.P. Walker, "Synchrotron Radiation", CERN Accelerator School in Finnland 1992, CERN 94-01 Vol. 1 pp. 437-459, 26 January 1994

[5] F. Gianotti, "Physics at LHC", CERN summer student lecture series 2000

[6] P. Lefèvre, T. Pettersson, et al., "The Large Hadron Collider", CERN/AC/95-05 (LHC), 20 October 1995

[7] Ph. Lebrun, "The Large Hadron Collider, a Megascience Project", CERN LHC Project Report 374, 5 April 2000

[8] Ph. Lebrun, "Advanced Superconducting Technology for Global Science: The Large Hadron Collider at CERN", CERN LHC Project Report 499, 27 AAugust 2001

[9] R. Perin, "Superconducting Magnets for the Large Hadron Collider", CERN LHC Project Report 52, 1996

[10] A. Ballarino, "High–temperature superconducting current leads for the Large Hadron Collider", Proc. IEEE 9 pp. 523-526, 1999

[11] Ph. Lebrun "Superfluid helium as a technical coolant", Atti XV Congresso Nazionale sulla Trasmissione del Calore, Edizioni ETS, Politecnico di Torino, Italy, 1997

[12] Ph. Lebrun, "Cryogenics for the Large Hadron Collider", invited paper at MT16, Ponte Vedra Beach, Florida, USA, 1999

[13] V. Benda, et al., "Conceptual design of the cryogenic system for the Large Hadron Collider (LHC)", CERN LHC Project Report 12, 1996

[14] L. Bottura, L. Walckiers and R. Wolf, "Field Errors Decay and Snap–Back in LHC Model Dipoles", Presented at the Applied Superconducting Conference 1996 in Pittsburgh, 2000 (LHC Project Report 55)

[15] A. P. Verweij, "Electrodynamics of Superconducting Cables in Accelerator Magnets", PhD thesis, Twente University, 1995

[16] R.Meinke, "Superconducting magnet system for HERA", IEEE Transactions of Magnetics, Vol. 27, NO. 2, pp. 1728–1734, 1991

[17] H. Brück, D. Gall et all., "Observation of a Periodic Pattern in the Persistent–Current Fields of the Superconducting HERA Magnets", Proc. IEEE Particle Accelerator Conference, San Francisco, pp. 2149, 1991

[18] Homepage: "The SSC Scientific and Technical Electronic Repository", http://www.hep.net/ftp/ssc/new/repository.html

[19] A. K. Ghosh, K. E. Robins and W. B. Sampson, "Axial Variations in the Magnetic Field of Superconducting Dipoles", Supercollider 4, edited by J. Nonte, pp. 765–772, 1992

[20] A. K. Ghosh, K. E. Robins and W. B. Sampson, "Time Dependent Magnetization Effects in Superconducting Accelerator Magnets", 15^{th} International Conference on High Energy Accelerators, Vol. 2, pp. 665–667, 1992

[21] A. K. Ghosh, K. E. Robins and W. B. Sampson, "The Ramp Rate Dependence of the Sextupole Field in superconducting Dipoles", IEEE Transactions of Magnetics, Vol. 30, NO. 4, pp. 1718–1721, 1994

[22] A. den Ouden et all., "Quench characteristics of the $11\,T$ Nb_3Sn model dipole magnet MSUT", 15^{th} International Conference on Magnet Technology, pp. 339–342, 1992

[23] J. Buckley, L. Bottura, D. Richter, L. Walckiers, R. Wolf and A. Verweij, "Dynamic Magnetic Measurements of Superconducting Magnets for the LHC", IEEE Transactions of Applied Superconductivity, Vol. 5, NO. 2, pp. 1024–1027, 1995

[24] L. Bottura, L. Walckiers and Z. Ang, "Experimental Evidence of Boundary Induced Coupling Currents in LHC Prototypes", IEEE Transactions of Applied Superconductivity, Vol. 7, NO. 2, pp. 801–804, 1997

[25] L. Bottura, M. Breschi and M. Schneider, "Measurements of Magnetic Field Pattern in a Short LHC Dipole Model", Presented at the Applied Superconducting Conference 2000, 2000

[26] G. H. Morgan, "Eddy currents in flat metal–superconducting braids", J. Appl. Phys. 44 (7), pp. 3319–3322, 1973

[27] A. Devred and T. Ogitsu, "Ramp–rate sensitivity of SSC dipole magnets prototypes", KEK preprint 94–156, 1994, submitted to Particle Accelerators

[28] K.-H. Mess, P. Schmüser and S. Wolff, "Superconducting Accelerator Magnets", World Scientific, Hamburg, 1996

[29] A. A. Akhmetov, A. Devred, and T. Ogitsu, "Periodicity of crossover currents in a Rutherford–type cable subjected to a time–dependent magnetic field", J. Appl. Phys. 75 (6), pp. 3176–3183, 1994

[30] A. A. Akhmetov, A. Devred, R. G. Mints and R. I. Schermer, "Current Loop Decay in Rutherford–Type Cables", Supercollider 5, edited by J. Nonte, pp. 443–446, 1994

[31] L. Krempasky and C. Schmidt, "Theory of 'supercurrents' and their influence on field quality and stability of superconducting magnets", J. Appl. Phys. 78 (9), pp. 5800–5810, 1995

[32] L. Krempasky and C. Schmidt, "Ramp–rate limitation in large superconducting magnets due to 'supercurrents'", Cryogenics 36 (6), pp. 471–483, 1996

[33] L. Krempasky and C. Schmidt, "Influence of supercurrents on the stability of superconducting magnets", Physica C 310, pp. 327–334, 1998

[34] L. Krempasky and C. Schmidt, "Experimental verification of 'supercurrents' in superconducting cables exposed to AC–fields", Cryogenics 39 (1), pp. 23–33, 1999

[35] L. Krempasky and C. Schmidt, "Time constant measurement in technical superconductors: A theoretical solution of the problem", J. Appl. Phys. 75 (8), pp. 4264–4266, 1994

[36] L. Krempasky and C. Schmidt, "Time constant measurement in technical superconductors", Cryogenics 37, Vol. 38, NO. 10, pp. 1017–1029, 1998

[37] E. H. Hall, "On a new action of magnetic and electric currents", American Journal of Mathematics, 2, pp. 287–292, 1879

[38] B. Berkes, "Hall Generators", Proceedings of CERN Accelerator School-Magnetic Measurement and Alignment, pp. 167–191, March 1992, CERN 92-05, 1992

[39] H.H. Wieder, "Hall Generators and Magnetoresistors", Pion Ltd., London, 1971

[40] F. M. Ašner, "High Field Superconducting Magnets", Clarendon Press, Oxford, 1999

[41] Z. Ang, I. Bejar, L. Bottura, L. Bottura, D. Richter, M. Sheehan, L. Walckiers and R. Wolf, "Measurement of AC Loss and Megnetic Field during Ramps in the LHC Model Dipoles", CERN LHC Project Report 241, April 1999, Presented at the ASC 1998

[42] W. Venturini Delsolaro, A. Arn, L. Bottura, C. Giloux, R. Mompo, A. Siemko and L. Walckiers, "The Test Facility for the Short Prototypes of the LHC Superconducting Magnets", submitted for publication to the CEC/ICMC 2001 hold in Madison, Wisconsin, USA, July 16-20, 2001

[43] N. Andreev, et al., "The $1\,m$ long single aperture dipole coil test program for LHC", CERN LHC Project Report 25, August 1996, Presented at the EPAC 1996

[44] D. Tommasini, F. Arteche, S. Sanfilippo, A. Siemko, I. Vanenkov and C. Wyss, "Status of the LHC Short Dipole Model Programme", CERN LHC Project Report 427, September 2000, Presented at the EPAC 2000

[45] AREPOC catalog, "High linearity Hall probes for room and cryogenic Temperature".

[46] P. Pugnat and A. Siemko, "Calibration and dynamic response of Hall probes at low temperature for current sharing experiment", CERN LHC MTA Internal Note 98-034, 1998

[47] N. W. Ashcroft and N. D. Mermin, "Solid state physics", International Edition, pp. 263–281, 1976

[48] L. Bottura, "Standard Analysis Procedures for Field Quality Measurements of the LHC Magnets – Part II: Transfer Functions and Parameterization", CERN LHC MTA Internal Note 98-27, 1998

[49] J. Billan et al., "Manufacturing features and performances of long models and first prototype for the LHC project", Proceedings of 6^{th} European Particle Accelerator Conference, Stockholm, pp. 2041–2043, 1998

[50] J. Billan et al., "Test Results on the Long Models and Full Scale Prototype of the Second Generation LHC Arc Diploes", IEEE Transactions of Applied Superconductivity, Vol. 9, NO. 2, pp. 1039–1044, 1999

[51] L. Bottura, P. Pugnat, A. Siemko, J. Vlogaert and C. Wyss "Performance of the LHC Final Design Full Scale Superconducting Diploe Prototypes", CERN LHC Project Report 452, December 2000, Presented at the ASC

2000, IEEE Transactions of Applied Superconductivity, Vol. 11, NO. 1, pp. 1554–1557, 2001

[52] L. Bottura, L. Larsson, S. Schloss, M. Schneider, N. Smirnov and M. Haverkamp "A Fast Sextupole Probe for Snapback Measurement in the LHC Dipoles", CERN LHC Project Report 362, December 1999, Presented at the 16th International Conference on Magnet Technology 1999

[53] C. Wyss et al., "LHC arc dipole status report", Proceedings of 1999 Particle Accelerator Conference, New York, pp. 149–153, 1999

[54] K. Artoos et al., "Design, manufacturing status, first results of the LHC main dipole final prototypes and steps towards series manufacture", IEEE Transactions of Applied Superconductivity, Vol. 10, NO. 1, pp. 98–102, 2000

[55] M. Buzio, Z. Ang, and L. Bottura, "MBP2O1 Magnetic Measurement Summary", CERN Internalnote, LHC-MTA-IN-2001-151, 2001

[56] S. Sanfilippo, S. Amet, Z. Ang, L. Bottura, M. Buzio and N. Smirnov, "MBP2A2 Magnetic Measurement Summary", CERN Internalnote, LHC-MTA-IN-2001-154, 2001

[57] S. Sanfilippo, S. Amet, Z. Ang, L. Bottura, M. Buzio and N. Smirnov, "MBP2O2 Magnetic Measurement Summary", CERN Internalnote, LHC-MTA-IN-2001-155, 2001

[58] S. Sanfilippo, A. Akhmetov, S. Amet, L. Bottura, M. Buzio and N. Smirnov, "HCMMBB_A1-01000001 Magnetic Measurement Summary", CERN Internalnote, LHC-MTA-IN-2001-165, 2001

[59] P. Schmüser, "Superconducting Accelerator Magnets", CAS - CERN Accelerator School: 5th Advanced Accelerator Physics Course, CERN 95-06 Vol. 2 pp. 993-1026, 1995

[60] Gnuplot–homepage, http://www.gnuplot.org

[61] P. Pugnat, Th. Schreiner and A. Siemko, "Investigation of the Periodic Field Modulation inside Apertures of LHC Superconducting Dipole Models", Proceedings of EPAC'00, Vienna, June 2000

[62] J. D. Adam, T. Boutboul, G. Cavallari, Z. Charifoulline, C. H. Denarie, S. Naour, D. F. Leroy, L. R. Oberli, D. Richter, A. P. Verweij and R. Wolf, "Status of the LHC Superconducting Cable Mass Production", submitted for publication to the MT 17 conference hold in Geneva, Sept. 24-28, 2001

[63] Python–homepage, http://www.python.org

[64] A. Akhmetov, Z. Ang, I. Balaazi, L. Bottura, M. Gateau, P. Pugnat and L. Walckiers, Energy loss and field advance in MBP2O1 prototype magnet at different ramp rates", CERN Internalnote, LHC-MTA-IN-2000-131, 2000

[65] H. Fayard and R. Wolf, "Principle of R_c measurement and application to the last magnet models", CERN Internalnote, LHC-MTA-IN-99-065, 1999

[66] A. Akhmetov, S. Amet, I. Balaazi, L. Bottura, M. Gateau, P. Pugnat and L. Walckiers, "Loss and Dynamic Magnetic Field Measurements in LHC Dipoles", submitted for publication to the MT 17 conference hold in Geneva, Sept. 24-28, 2001

[67] Th. Schreiner, P. Pugnat and A. Siemko, "Investigation of the Periodic Magnetic Field Modulation in LHC Superconducting Dipoles", submitted for publication to the MT 17 conference hold in Geneva, Sept. 24-28, 2001

[68] A. Siemko, "Magnet Quench Process", Proceedings of the LHC Workshop Chamonix XI, CERN-SL-2001-003 DI, pp. 245–249, January 2001

[69] D. Leroy, J. Krzywinski, V. Remondino, L. Walckiers and R. Wolf "Quench observation in LHC superconducting one meter long dipole models by field perturbation measurements", IEEE Transactions of Applied Superconductivity, Vol. 3, pp. 781–784, 1993

[70] J. Billan, L. Bottura, M. Buzio, G. D'Angelo, G. Deferne, O. Dunkel, P. Legrand, A. Rijllart, A. Siemko, P. Sievers, S. Schloss and L. Walckiers "Twin rotating coils for cold magnetic measurements of $15\,m$ long LHC dipoles", IEEE Transactions of Applied Superconductivity, Vol. 10, NO. 1, pp. 1422–1426, 2000

[71] P. Pugnat, B. Khomenko, A. Rijllart, S. Sanfilippo and A. Siemko "Statistical Diagnosis Method of Conductor Motions in Superconducting Magnets to Predict their Quench Performance", CERN LHC Project Report 455, December 2000, Presented at the ASC 2000, IEEE Transactions of Applied Superconductivity, Vol. 11, NO. 1.2, pp. 1705, 2001

[72] J. Adam et al., "Status of the LHC superconducting cables mass production", submitted for publication to the MT 17 conference hold in Geneva, Sept. 24-28, 2001